DUPLICATE ALSO

Advanced Lectures 1988

The physics and dynamics of the climate system

Part 2

LONDON, METEOROLOGICAL OFFICE.
Advanced Lectures 1988

The physics and dynamics of the climate system.
Part 2.

00221088 551.583 551.588 551.513.1 F62

ORGS UKMO A

National Meteorological Library
FitzRoy Road, Exeter, Devon. EX1 3PB

quarters, Bracknell

DUPLICATE ALSO

METEOROLOGICAL OFFICE
152899
27 SEP 1988
C
LIBRARY

Advanced Lectures 1988

The physics and dynamics of the climate system Part 2

P.R. Rowntree

S.J. Foreman

H. Cattle

J.F.B. Mitchell

Permission to quote from this document must be obtained from the Principal, Meteorological Office College, Shinfield Park, Reading RG2 9AU

The physics and dynamics of the climate system Part 2

6. **Forcing of the ocean circulation**
   H. Cattle
7. **The observed ocean circulation**
   H. Cattle
8. **Long time scale parts of the climate system**
   H. Cattle
9. **Simulation of climate**
   J.F.B. Mitchell
10. **Simulation of climate change**
    J.F.B. Mitchell

PHYSICS AND DYNAMICS OF THE CLIMATE SYSTEM

FORCING OF THE OCEAN CIRCULATION

H Cattle

Met O 20, Meteorological Office, Bracknell

6.1 INTRODUCTION

As emphasised in previous lectures, the atmosphere, oceans, land and sea ice are interacting, constituent parts of the climate system, with the surface characteristics of the ocean (its temperature and sea ice cover) forming a temporally and spatially variable bottom boundary condition to the atmosphere. The oceans are important for climate for a number of reasons:

- they determine and affect the atmospheric climate through the sea surface temperature and its variations and the extent and variability of the sea ice cover. These are themselves affected by the atmosphere via the air-sea exchanges.

- they carry a significant amount of the poleward transfer of heat within the ocean-atmosphere system

- they possess a large thermal inertia

In this lecture we shall consider aspects of the first two of these. The origin of the ocean forcing by the atmosphere (Figure 6.1) is primarily in the fluxes of momentum, heat and water substance across the air-sea interface. The ocean is therefore driven both by the wind, via the effects of the surface wind stress, and viathe so-called thermohaline forcing, which arises as the combined result of the net surface heating or cooling and the freshwater input. Note (Figure 6.1) that the determining equations for the ocean are similar in nature to

those for the atmosphere. For both systems, the equation of continuity and the appropriate equation of state complete the set.

6.2 SALINITY AND THE EQUATION OF STATE FOR SEA WATER

A particular characteristic of the ocean is, of course, its saltiness, the composition of which is shown in the table below. Amounts are in percentage of the total salt content:

Ion	Amount
Chloride	55.0%
Sodium	30.6%
Sulphate	7.6%
Magnesium	3.7%
Calcium	1.2%
Potassium	1.1%
Bicarbonate	0.41%
Bromide	0.19%
Boric Acid	0.075%
Strontium	0.038%
Fluoride	0.003%

The effect of the dissolved salts is to alter the physical properties of sea water from those of pure water. In particular the freezing point is lowered to about -1.8 C (see Figure 6.2). The salinity of sea water is expressed in units of grams of solid material per kilogram of sea water. Over the world ocean, surface salinities range from of order 29‰ (parts per thousand) in the Central Arctic to 37.5‰ in the subtropical North Atlantic (Figure 6.3), the average value being of order 35‰. The surface salinity field reflects the general pattern of sources and sinks of freshwater. These comprise the net freshwater flux across the air-sea interface as given by the difference between the precipitation less the evaporation, the influx of fresh water due to river inflow and the effects of ice formation and melt.

The density of sea water is a complex function of temperature, salinity and depth (or pressure), i.e.

$$\rho = \rho(T, S, P)$$

For a detailed description of the equation of state for sea water, the reader is referred to the standard textbooks on physical oceanography (as a starting point see e.g Pond and Picard, 1978) A useful rule of thumb is that density increases by approximately one part per thousand (i.e. by 1kg m^{-3}) for a change of temperature of -5 C, a change of salinity of 1‰ or a change of pressure of 2000 kPa (=200 db, equivalent to a depth change of 200m). Figure 6.2 shows the variation of density of sea water at atmospheric pressure (expressed in terms of $\sigma_t = \rho - 1000$ kg m^{-3}) as a function of temperature and salinity. Note that 90% of the ocean has temperature and salinity values over a relatively short range. This is mostly sub-surface water, the remainder of the range of properties in the figure represents limited volumes of surface waters.

Figure 6.2 also demonstrates that the density of sea water is more sensitive to changes in salinity at low temperatures than high, whereas the opposite is true for temperature itself. This effect goes to enhance the salinity stabilisation of the density profile in Arctic waters, itself important for the maintenance of the sea ice cover (see lecture 8).

6.3 THE OCEAN BOTTOM TOPOGRAPHY

Overall, approximately 71% of the earth's surface is covered by water and oceanic dynamics is dominated both by the relatively small size of the Rossby radius (which determines the characteristic eddy size - see Lectures 2/3) and by the fact that the oceans are split into a series of basins. The ocean bottom topography, itself an important influence on the oceanic circulation, is highly variable in nature. As illustrated in Figure 6.4, continental shelves extend outward into the ocean basins for a distance of anywhere from a few to several hundred kilometers and with a gradient of order 1 in 500. The edges of the shelves give way to a very steep continental slope which extends to, or near, the deep sea bottom, the topography of which is marked by underwater mountains, ridges, trenches and in some locations fairly smooth basins. The largest and most extensive feature is the mid-ocean ridge, extending north to south along the mid Atlantic Ocean and into both Pacific and Indian Oceans. The mean ocean depth is of order 4000m.

6.4 THE OCEAN TEMPERATURE STRUCTURE

An important factor in determining aspects of the air-sea exchange is the sea surface temperature. Figure 6.5 shows the global field of mean sea surface temperature (sst) for the northern hemisphere spring and autumn. Values range from freezing point in polar regions up to 30 C in the tropics. On a seasonally averaged basis, the isotherms are approximately zonal. However, noteable divergences from the zonal structure appear in the tropical Pacific, where temperatures tend to be warmer in the west than in the east, and in the North Atlantic and North Pacific, where the contours fan out across the basins from the regions of very intense gradient associated with the *western boundary currents - the Gulf Stream and Kuroshio* (see Lecture 7). Note also the wave-like nature of the sst pattern in the southern ocean and evidently associated, at least in part, with topographic steering of the circumpolar current. The impact of the variability of sea surface temperature on atmospheric climate is discussed at length in the companion series of lectures to these, **Climate of the World**, and so will not be pursued further here. However, note that whilst, like the atmosphere, the ocean possesses its own inherent variability, the origin of sst anomalies on a variety of timescales ultimately lies, to a large extent, in variations in the nature of the atmospheric forcing on the ocean.

Over much of the ocean, an upper well mixed layer can be discerned in which the temperature and salinity profiles are constant with depth. Below this lies an often well defined stable layer through which the temperature decreases with depth and salinity increases. Over the mid-latitude oceans in particular, the mixed layer depth varies markedly with season from values of perhaps 20 or 30m in summer, when solar heating at the surface is a maximum and mixing due to wind stirring (see below) is a minimum to 100m or more in winter as a result of surface cooling and stronger wind stirring (Figure 6.6). Because the significant temperature gradient evident in the upper hundred metres or so ceases to exist in winter, it is called the *seasonal thermocline*. Much deeper in the ocean, extending from below a hundred metres to 800-1000m, is the *permanent thermocline* which predominates in low and mid-latitudes. This can be seen in Figure 6.7 which shows the zonally and annually averaged ocean potential temperature as a function of latitude and depth. Variations in the depth of the seasonal thermocline

(especially in spring and autumn) can occur on timescales as short as a few hours (Figure 6.8) as result of advective effects (horizontal and vertical), changes in surface heating and cooling (the former tending to lead to stabilisation and shallowing of the layer and the latter to convective deepening), direct windmixing effects and effects of shear mixing associated with changes in the wind at the surface. For further details of the representation of mixed layer processes, see e.g. the Advanced Lecture Notes by Cattle (1986). By contrast to the changes in the depth of the seasonal thermocline, the permanent thermocline shows little seasonal variation overall, except at the boundaries between mid and high latitudes.

The averaged temperatures at the lower levels of the ocean are nearly uniform with values between 0.5 and 1.25 C. The coldest bottom temperatures of just below -0.25 C occur at 60°-70°S near the Antarctic continent. Such temperatures are consistent with the fact that much of the cold bottom water throughout the oceans derives from surface cooling and sinking of water in the polar regions of both hemispheres, particularly near the open ocean and shoreline edges of a divergent sea ice pack. This occurs because as freezing takes place, much of the salt content of the water is expelled as brine to mix with the water below. The increasing density of the upper waters as a result of the brine rejection tends to destabilise the water column and eventually lead to deep convection which may extend down to the ocean bottom (Figure 6.9). The overall effect of high latitude convective processes on the temperature structure of the oceans can be seen in Figure 6.7. Note the contrast with the atmosphere in which much of the deep convection occurs in low latitudes as a result of surface heating whereas in high latitudes, the net cooling tends to stabilise the polar atmosphere. By contrast, in the oceans, the convection to depth takes place in high latitudes in association with processes associated with surface cooling whereas the net heating in the tropics leads to strong stabilisation of the ocean structure overall.

6.5 THE WIND FORCING OF THE OCEAN

The importance of wind driving for the overall circulation of the ocean, and in particular for the oceanic mass transport (the Sverdrup transport, dependent on curl τ/β, where $\beta = \partial f/\partial y$, the variation of

Coriolis parameter with latitude) will be discussed in the next lecture. However, because of its particular importance to ocean transport theories (Sverdrup, 1947; Stommel, 1948; Munk, 1950), the geographical distribution of surface wind stress has been extensively analysed for the past few decades and many climatological features of the stress field are now well documented, though details of the temporal and spatial structure of the stress field are not well known. Early studies employed monthly mean compilations of wind rose data with assumptions about the distributions of wind speed (e.g. Hidaka, 1958) or more explicit information on the wind speed distribution (and improved wind rose data), when these became available (Hellerman, 1967). The Hellerman stress fields were derived in the form of four three-month averages defined on a 5° x 5° global grid. Eyre (1972) later computed monthly mean wind values for all calendar months. More recently, millions of surface observations collected by the national Climatic Center, Asheville, NC, designated TDF 11, have become available. These have been used by a number of authors (e.g Wyrtki and Meyers, 1976; Bunker, 1976, 1988; Hastenrath and Lamb, 1977) in basin scale derivations of the wind stress field, whilst a data set of monthly mean wind and its standard deviation derived from the TDF 11 data was used in a global determination of the surface stress field (again with assumptions about the wind distribution and supplemented by surface pressure data in data sparse regions) by Han and Lee (1981). More recently, Hellerman and Rosenstein (1983) have used the TDF 11 tapes to derive a new monthly mean dataset of global windstress, illustrated in Figure 6.10 for the months of January and July. In each case a relationship between the vector wind stress, $\boldsymbol{\tau}$, and wind, $\mathbf{V}$ was used of the form:

$$\boldsymbol{\tau} = \rho C_D \mathbf{V}V$$

with various assumptions about the drag coefficient, C_D. For details, the reader is referrred to the individual papers.

The effects of the wind stress and its temporal and spatial variability have important consequences, not only for the large-scale ocean dynamics, but also for mixing and structure of its upper layers, in respect of which, the effect of the wind on the surface is to:

(i) induce turbulent vertical mixing ('windmixing'), dependent on the three-halves power of the stress (or the cube of the wind) (Figure 6.11), the effect of which generally decays significantly with depth through the mixed layer.

(ii) generate shear mixing events at the base of the mixed layer as a result of inertial motions (which may decay on a timescale of a few days) initiated via *changes* in the wind (Figure 6.12). Such motions are sinusoidal in time, with period $2\pi/f$ (f is the Coriolis parameter), inversely proportional to the depth of the mixed layer, h, and proportional to the change in the components of the stress.

(iii) generate an 'Ekman' flow in the mixed layer with a vertically integrated transport given by:

$$\mathbf{V}_E = - (1/\rho_w fh)\mathbf{k} \times \boldsymbol{\tau}$$

and directed to the right of the wind stress in the northern hemisphere and to the left in the southern hemisphere. This effect is illustrated from a model simulation in Figure 6.13(a) and (b).

(iv) generate a vertical motion at the base of the mixed layer (Ekman pumping) given by:

$$w_h = (1/\rho_w)\mathrm{curl}(\boldsymbol{\tau}/f)$$

Figure 6.13(c) and (d) compares a model generated vertical motion field at the base of an assumed constant 50 m depth mixed layer with the field of curl $\boldsymbol{\tau}$. Note that, associated with the convergence of the trades there (Figure 6.13(a) and (b), there is a large upwelling generated at the equator. Over the subtropics there is downwelling as a result of the Ekman *divergence* generated in the mixed layer as a consequence of the *convergence* of the trade winds to the north and south of the equator. Note also the coastal upwelling regions and the upwelling in mid latitudes associated with *divergence* in the oceanic Ekman flow there, consequent upon the *convergence* of the westerly atmospheric flow regime

6.6 THE HEAT FLUX AT THE OCEAN SURFACE

Also important for the ocean circulation and mixed layer structure are the effects of variations in the density field These are brought about by the differential heating of the oceans, which we shall now consider, and the input of fresh water at the ocean surface.

The net heat flux at the ocean surface arises as a combined effect of

(i) the net solar radiation $(1 - \alpha)S$ which passes across the air-sea interface. Here α is the albedo of the surface (typically of order .05) and S, the total incoming shortwave radiation there.

(ii) the net longwave radiation at the surface, R_N, the difference between the downward longwave radiation from the atmosphere and the upward longwave (σT_*^4) from the ocean surface (σ is Stefan's constant and T_* the surface temperature.

(iii) the surface sensible heat exchange, H.

(iv) the surface latent heat exchange, LE, where E is the evaporation flux and L the latent heat of vaporisation.

The net heating across the ocean surface at any given location is therefore given by:

$$F_N = (1 - \alpha)S + R_N + H + LE$$

There have, in the past been a considerable number of studies to determine the components of the oceanic surface heat balance. Budyko (1963) was the first to conduct a study of the spatial and temporal structure of the heat balance on a global scale for which he employed available meteorological observations (of temperature, wind, humidity, sea level pressure and cloud) and bulk parametrisations of the fluxes. Since then, many regional studies have been carried out by investigators using similar methods. For example, Bunker and his coworkers (Bunker, 1976; Bunker and Worthington, 1976; Bunker and Goldsmith, 1979) carefully constructed a relatively high resolution study of the heat balance of the North and South Atlantic Oceans. Their study supported the gross features revealed by Budyko's study and offered better

estimates on the fine structure of the heat exchange patterns, principally over the Gulf Stream of the North Atlantic. Hastenrath and Lamb (1977, 1978 and 1979) used long term 1° x 1° latitude-longitude averages of surface marine observations to establish a monthly high resolution climatology of the heat budget over part of the tropical ocean. More recently, Weare et al. (1981) studied the heat budget climatology over the tropical Pacific Ocean and Esbensen and Kushnir (1981) using similar techniques to those of Budyko rederived the heat budget over the global ocean (excluding areas covered by sea ice) to provide a dataset readily available in machineable form.

Figure 6.14 shows the annual mean distribution of the components of F_N from the Esbensen and Kushnir atlas. As expected, the input of solar radiation is a maximum over the tropical oceans, with a marked gradient in middle latitudes. Note the relative maxima over the sub-tropical high pressure cells. The field of net longwave flux is relatively uniform everywhere with values typically of order 40-60W m^{-2} and contributes, on average, to a cooling of the surface. Both the evaporation flux and sensible heat transfer also cool the surface on average, though, in the annual average, the latter contributes a small warming effect in some high latitude locations. The sensible heat exchange is a maximum off the eastern seaboards of the northern hemisphere continents, which largely reflects the impact of advection of cold air off the land masses in winter. Otherwise, the field represents the weakest heat sink for the ocean surface layer and lacks spatial coherence.

The latent heat exchange, on the other hand shows large values over the tropical oceans (reflecting the non-linear dependence of the saturation vapour pressure of water on temperature) which are of order half the solar input. Note the relatively low values over the colder surface waters of the tropical Eastern Pacific. As for the sensible heat flux, maxima are also found off the eastern seaboards of the northern hemisphere continents. The evaporation falls to relatively low values, on average, in high latitudes.

Note that overall, the solar heat flux acts to heat the ocean, whereas the other components of the heat balance act to cool the ocean surface. In tropical regions the solar heat flux dominates, whilst the reverse is the case in higher latitudes. The pattern of annual average net

downward heat flux into the oceans is shown in Figure 6.15(a). The net heating of the tropical oceans has a maximum on the eastern sides of the tropical Pacific and Atlantic and in the northern Indian Ocean. There is, however, considerable uncertainty in current estimates of the magnitude of the heat flux - compare Figures 6.14 and 6.15 with Figure 6.16 which shows the corresponding fields from an analysis by Reed (1985). Differences by up to a factor of two can be seen between the net oceanic heating displayed in the two figures.

In mid and high latitudes, the ocean surface shows a net cooling, with maxima associated with the large wintertime evaporation and sensible heat exchanges on the western sides of the north Atlantic and Pacific Oceans. There is some suspicion that the values off the southern hemisphere ice edge may be too small, possible due to lack of a sufficiently representative data coverage there.

An indication of the seasonal variation of the net heat flux is shown in Figure 6.15(b) which demonstrates the annual cycle of zonal mean values of this quantity. On average, there is a net heating of the tropical oceans throughout the year, whilst higher latitudes warm during the summer (as a result of the predominance of solar heating over surface cooling then) and cool markedly in winter.

6.6 THE OCEANIC HEAT TRANSPORT

The solar flux differs from the other components in that it is absorbed with depth in the top 100m or less, whereas the others act essentially at the surface. The molecular absorption of the radiation varies strongly with wavelength, so that the infra-red component of the solar input is absorbed in the top centimetre, while the blue-green sunlight can penetrate to 100m or more. The vertical distribution of oceanic heating therefore depends on the spectrum of surface irradiance; it also depends significantly on the turbidity of the sea water (Jerlov, 1976) due mainly to the presence of plankton, the depth distribution of which exhibits dramatic seasonal variations. The rate of solar heating decreases quasi-exponentially with depth. If there were no mixing, the temperature profile would also be of exponential form.

On average, the ocean is losing energy at the same rate as it is received. However, because the energy is absorbed at depth it must be transported to the surface before it can be lost to the atmosphere. Both vertical and horizontal transport processes have a part to play in the eventual heat loss from the surface. Leaving aside molecular conduction, which contributes significantly only in the surface skin, dominent vertical transport processes are up- and downwelling, turbulence generated by wind and shear induced mixing and convection. Of these, upwelling, and convection act to bring heat upwards to the surface, whilst downwelling and wind and shear induced mixing act to carry heat down. Note (Figure 6.13(d)) that downwelling operates in a broad swath across the subtropical oceans, whilst upwelling is, in general restricted to equatorial regions, the higher latitudes and close to coastal regions. Both windmixing and shear induced mixing have greatest effect in the ocean close to the surface, whilst the depth of convective adjustment exhibits large regional and seasonal variation (Figure 6.17)

One of the most important aspects of the ocean circulation for climate studies is the poleward transport of heat in both hemispheres. As already discussed, there is a net surface heating in the tropics and subtropics, while, in general, the opposite is true poleward of the subtropics, where the surface is cooling. For equilibrium, the oceans as a whole must transport heat from the regions of net surface heating to the regions of surface cooling. Of the total heat transport by the climate system, the oceans contribute perhaps 40%. Oort and Vonder Haar (1976) computed the ocean heat transport as a residual by first determining from satellite data the radiation imbalance at the top of the atmosphere and then subtracting out the atmospheric heat transport and seasonal heat storages in the system. Figure 6.18(a) shows the resultant values of the seasonal variation of the ocean heat flux, which Oort and Vonder Haar derived for the northern hemisphere only. Note the large seasonal variation in the ocean heat flux at 20° N from 5 x 10^{15} W in April-May to zero in July-August. The seasonal changes are caused in part by changes in the winds, which in turn cause stronger or weaker Ekman transport. Since there is upwelling at the equator and poleward surface circulations on both sides of the equator, heat can be transported from the tropics to the subtropics in these mainly wind-driven direct cells. The annual mean heat transport for all three major oceans (Atlantic, Pacific and Indian) combined is illustrated in Figure

6.18(b) and for the individual ocean basins in Figure 6.18(c). The estimates by Hastenrath (1980) were computed by integration of the observed surface energy balance. That of Bryden and Hall for 25° N was obtained directly from oceanographic measurements via an equation of the form:

$$\int \int \rho C_p T v \cos\varphi \, d\lambda \, dz$$

where the first integral is taken over depth and the second along the line of latitude traversing the basin. v is the meridional component of the current, φ and λ are latitude and longitude. Note that the transport is northward in both the North and South Atlantic, and southward in the Indian Ocean, a point to which we shall return in Lecture 8.

6.7 FRESHWATER FLUXES AND TRANSPORTS

The sources of freshwater for the ocean lie in the difference between the precipitation and evaporation flux and in the continental runoff (including ice calving). The global mean evaporation from the ocean is 1.2m yr^{-1}, which equates to a volume of 440 km^3. This rate is equivalent to a residence time of about 3000 years, compared with about 1 year for soil moisture and 10 days for the atmosphere. The overall water cycle is illustrated in Figure 6.19(a). The variation of evaporation with latitude is reflected in the pattern of Figure 6.14(d). The distribution of precipitation over the ocean is one of the most uncertain features of the hydrological cycle, though the main features are well known (Figure 6.19(b)). Figure 6.19(c) illustrates the continental runoff, much of which (74%) flows into the Atlantic and Arctic basins. Of the remainder, the Pacific receives 18% and the Indian Ocean 8%. The groundwater contribution is unknown. Note (Figure 6.19(a)) that, as would be expected, the continental runoff goes to balence the total loss of freshwater from the ocean due to the excess of evaporation over precipitation. As noted earlier, the pattern of precipitation less evaporation is reflected, away from the sources of continental runoff in the field of surface salinity (compare Figures 6.20 and 6.3). The vertically integrated fresh water circulation can be inferred (though with considerable uncertainty) from the distribution of net surface water flux. An example taken from Baumgartner and Reichel

(1975) is shown in Figure 6.21(b). Note the different character of the transports of heat (Figure 6.21(a) and fresh water in the individual ocean basins, in particular the northward heat flow along the whole length of the Atlantic, already mentioned, and the southward water flow through the length of the Pacific.

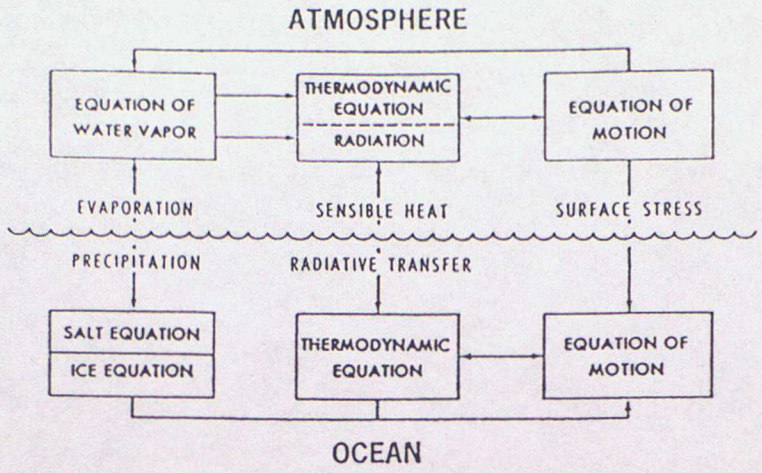

Figure 6.1 Ocean-atmosphere coupling.

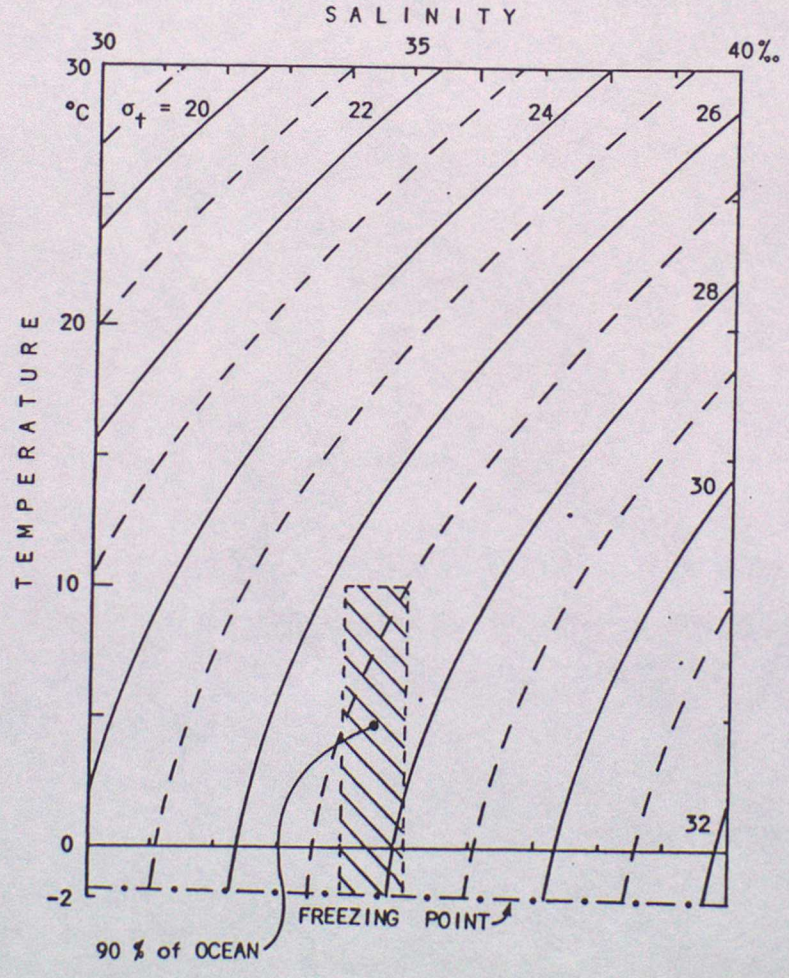

Figure 6.2 Values of density (as σ_t - see text) as a function of temperature and salinity over ranges appropriate to most of the ocean. (90% of the ocean volume has temperature and salinity values within the dashed rectangle.) From Pond and Pickard (1978).

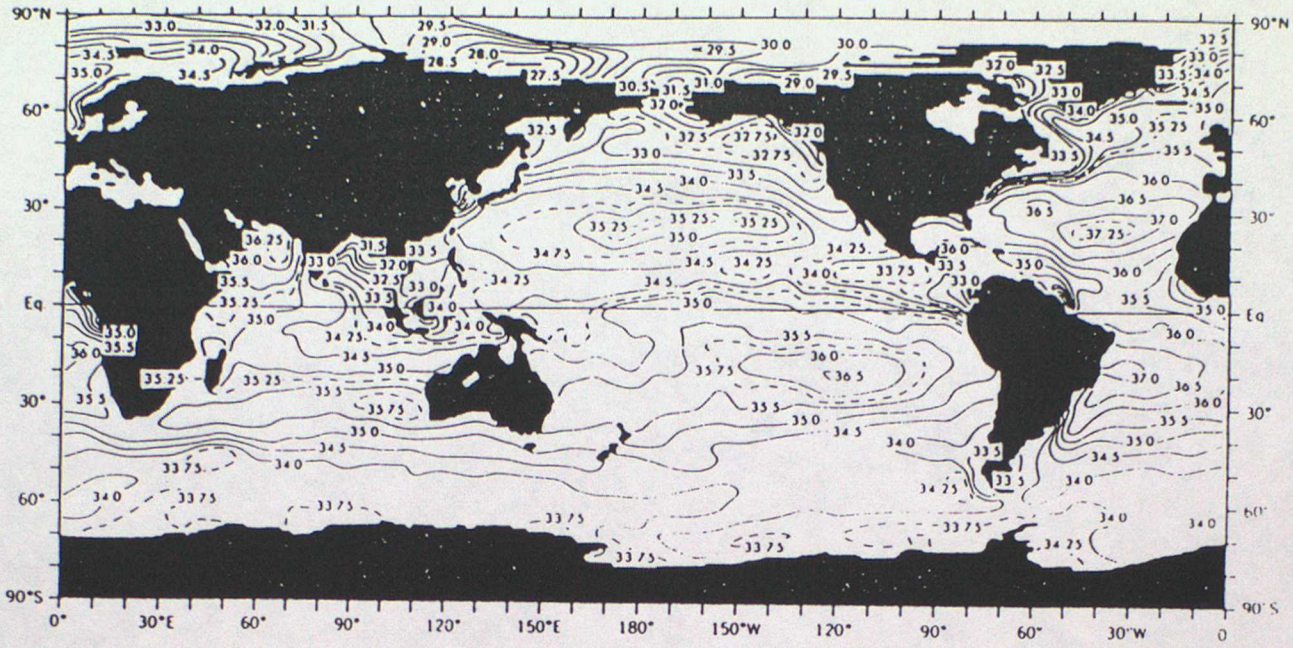

Figure 6.3 Annually averaged sea surface salinities (in ‰) (From Levitus, 1982)

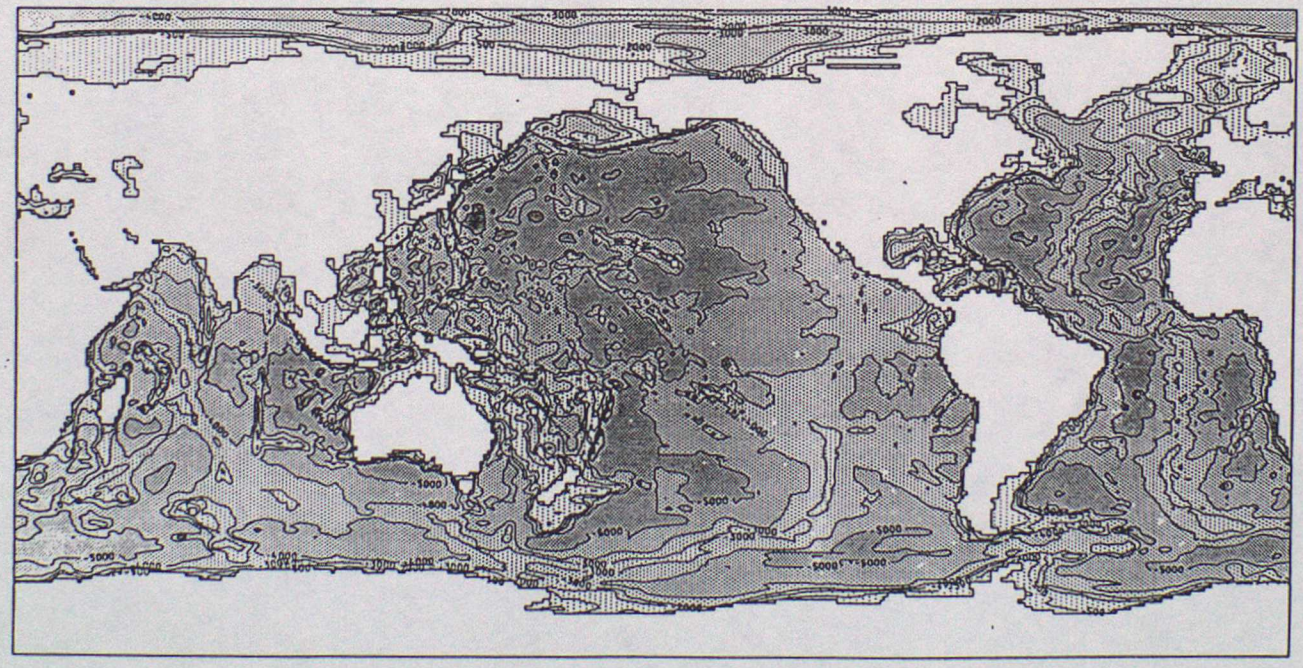

Figure 6.4 Ocean bottom topography. Contour intervals are 0, 500, 2000, 3000, 4000, 5000, 6000m, with each band shaded separately.

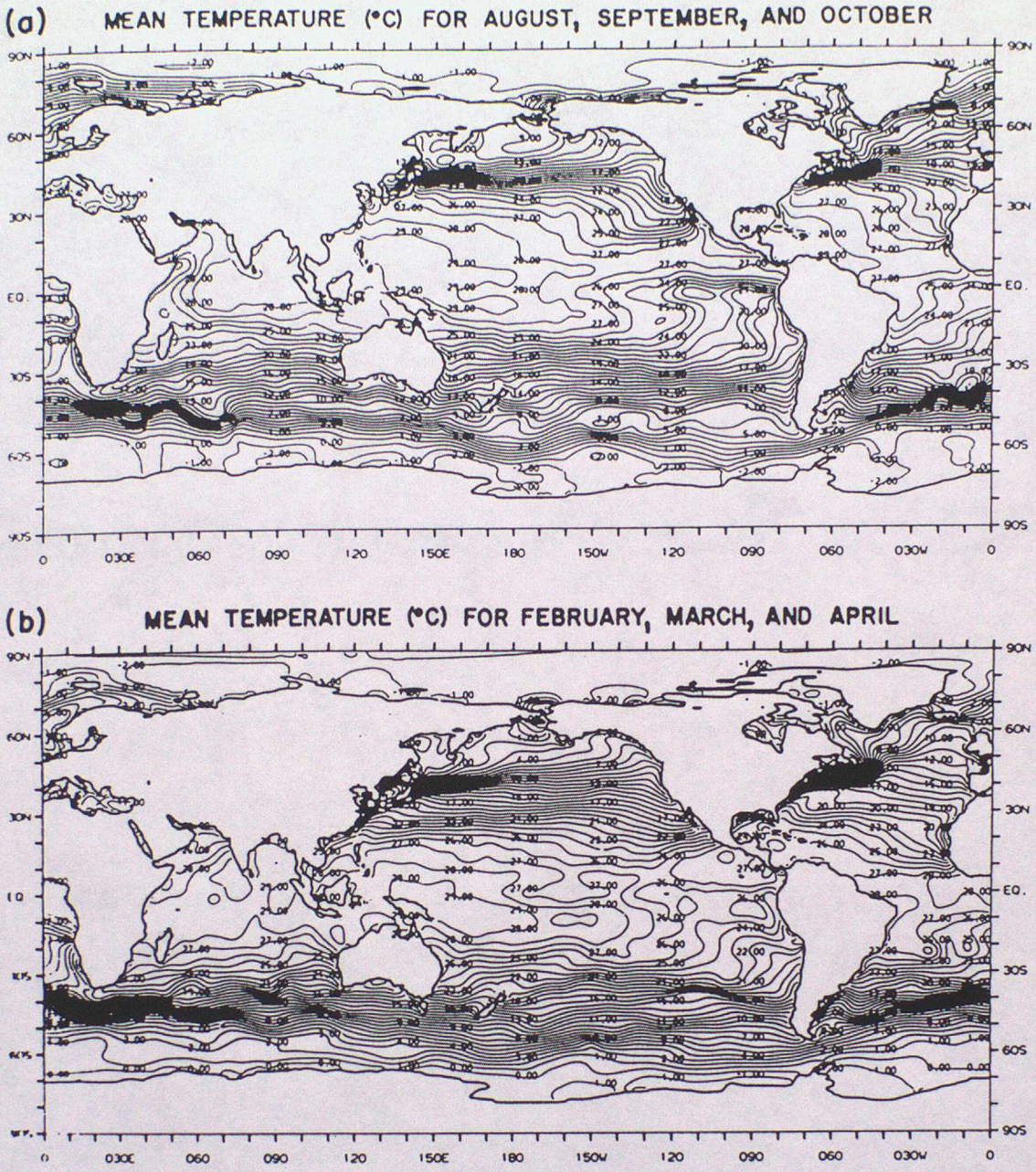

Figure 6.5 Seasonally averaged sea surface temperatures for (a) August, September and October and for (b) February, March and April. (From Levitus, 1982)

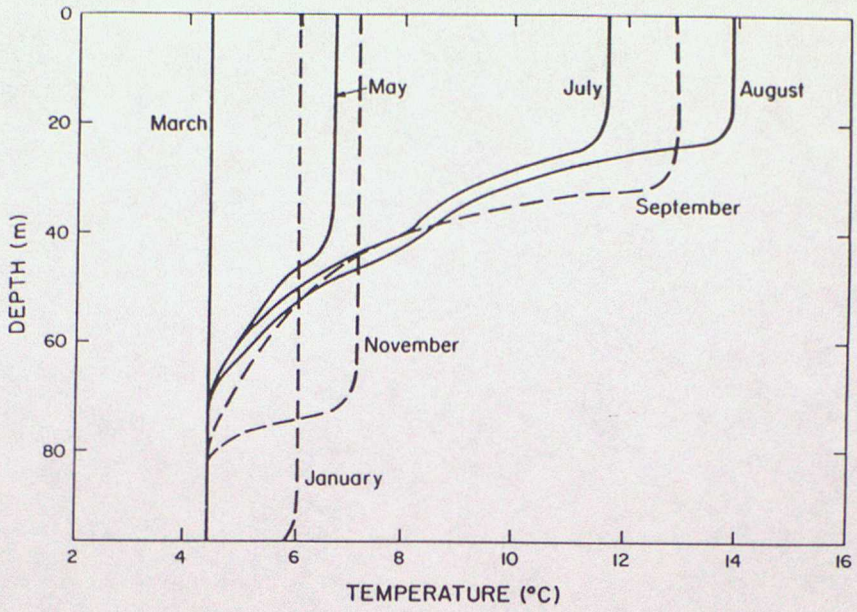

Figure 6.6 Standard ocean temperature profiles in the Northern hemisphere mid-latitudes in January, March, May, July, August, September and November. (After Knauss, 1978)

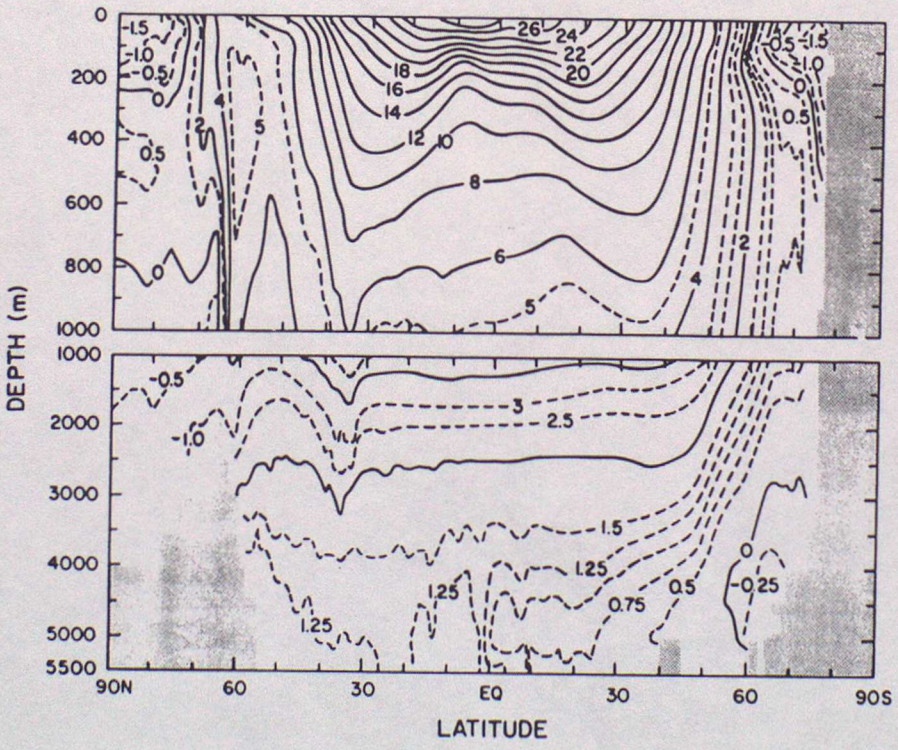

Figure 6.7 Annually averaged potential temperature (in degrees C) as a function of latitude and depth. (From Levitus, 1982).

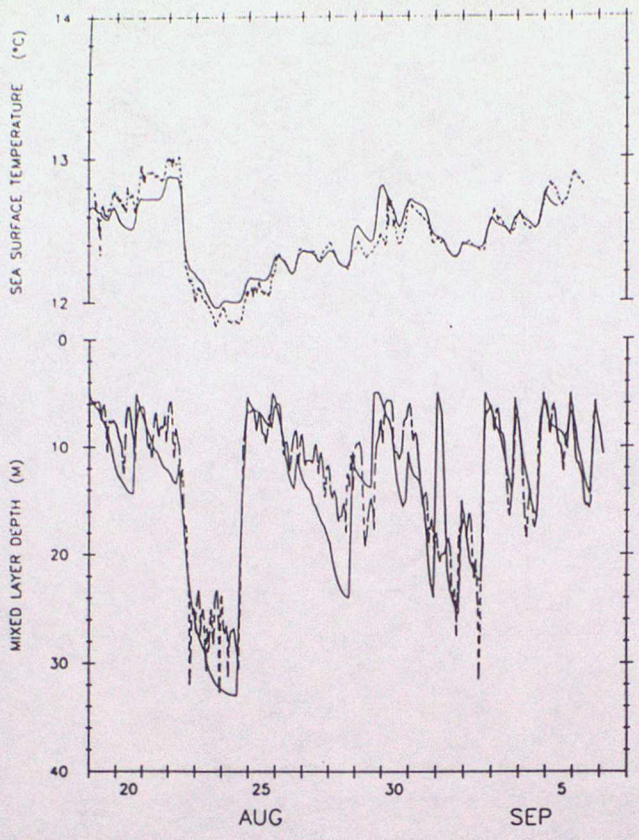

Figure 6.8 Variations in sea surface temperature and mixed layer depth at OWS P (50°N, 145°W) during autumn, 1977, as observed (dashed) and modelled using a mixed layer model. (From Davis, de Szoke and Niiler, 1981)

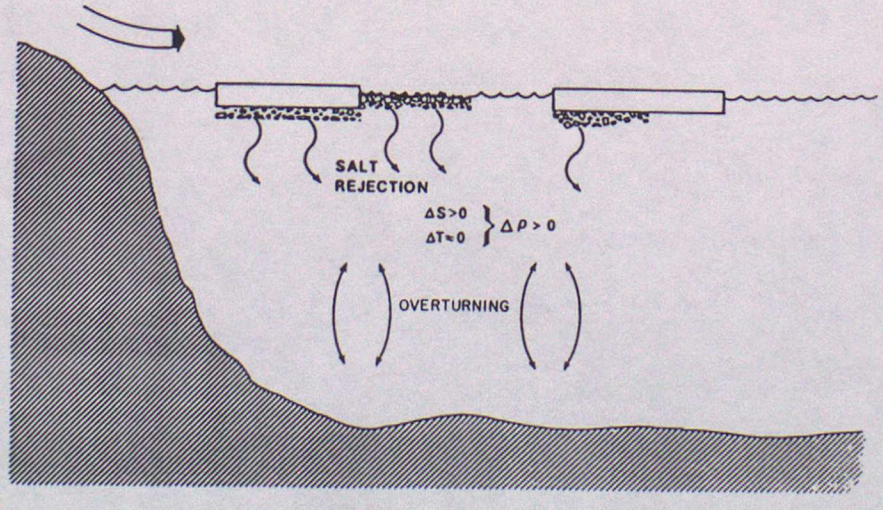

Figure 6.9 Schematic diagram of the possible inducement of deep oceanic convection by the rejection of salt during sea ice formation. (From Parkinson, 1985)

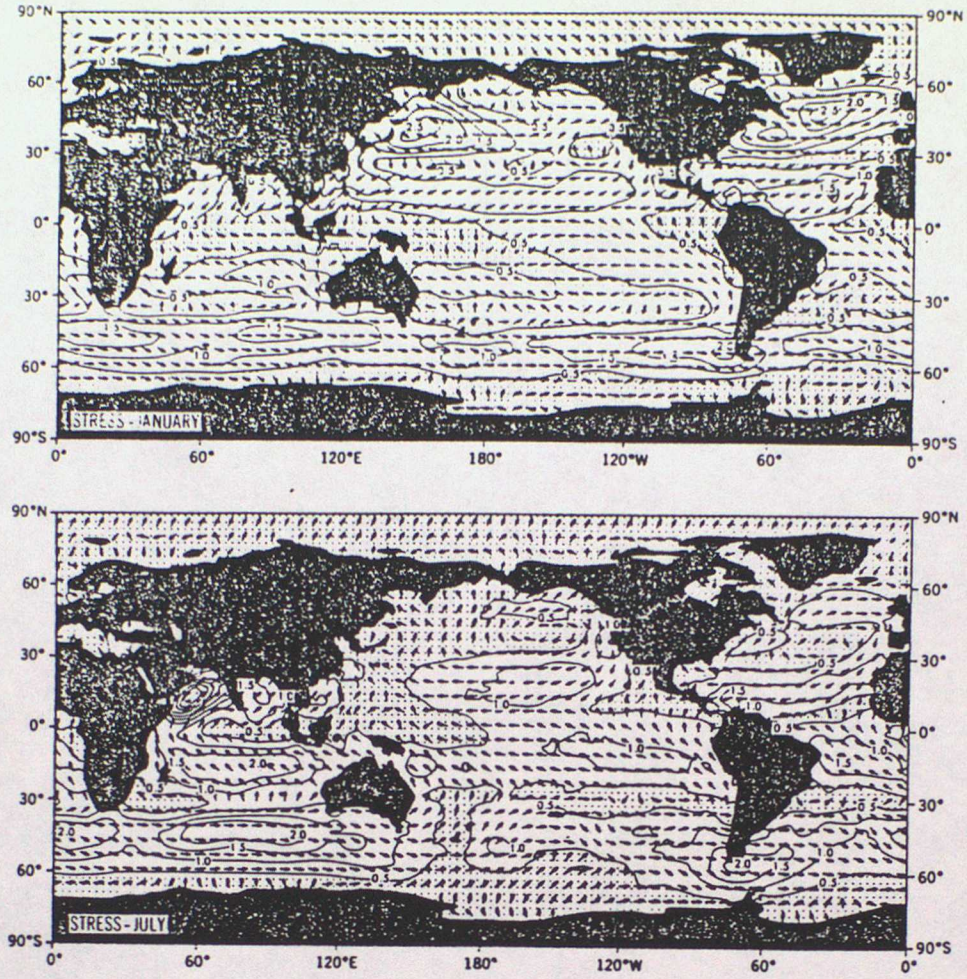

Figure 6.10 Wind stress fields. Arrows indicate direction and contours the magnitude (dyn cm^{-2}) Shading marks magnitudes < 0.5 dyn cm^{-2}. (From Hellerman and Rosenstein, 1983).

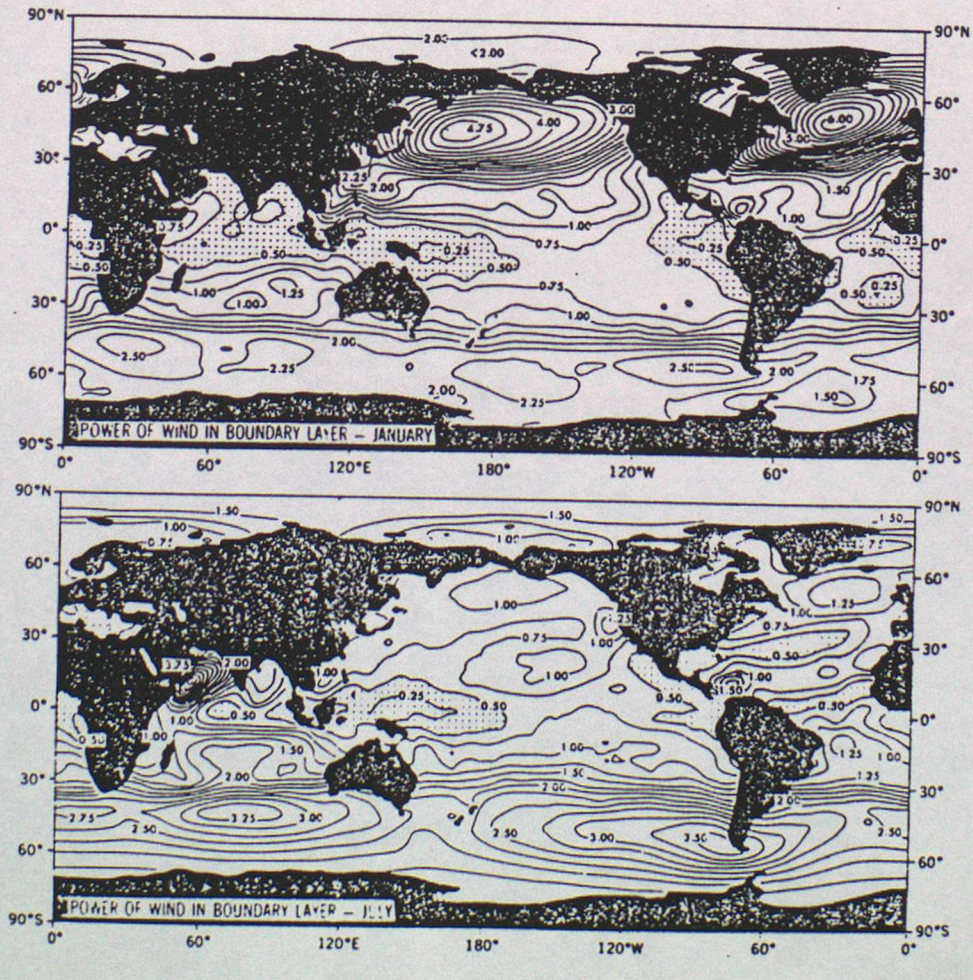

Figure 6.11 Estimate of the windmixing energy (in milliwatts) for January and July. (From Hellerman and Rosenstein, 1983).

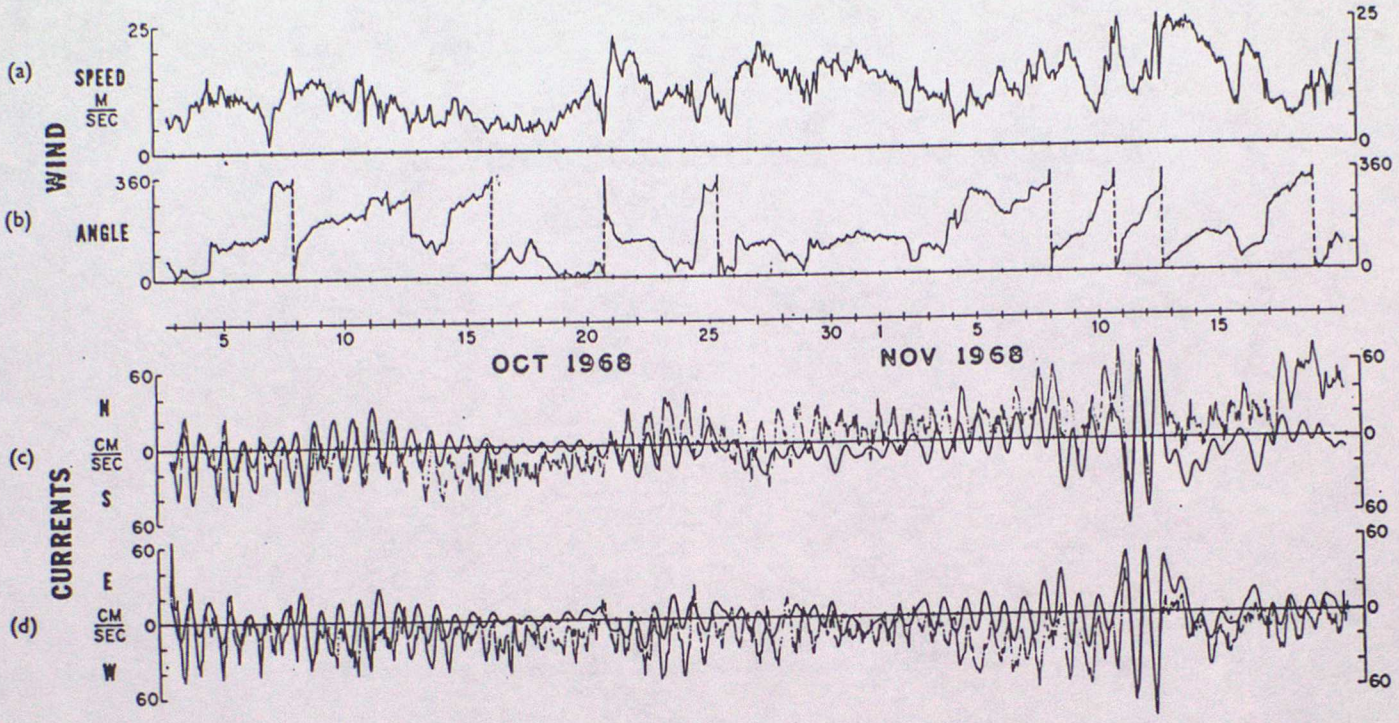

Mooring 280. One-hour averages of (a) wind speed; (b) direction towards which wind blows (measured clockwise from north); (c) North–south components of the model with a 4-day damping (smooth, thick curve) and the observed current 2803 at 12 m deep (jagged, thin curve); (d) East–west components.

Figure 6.12 From Pollard and Millard (1970)

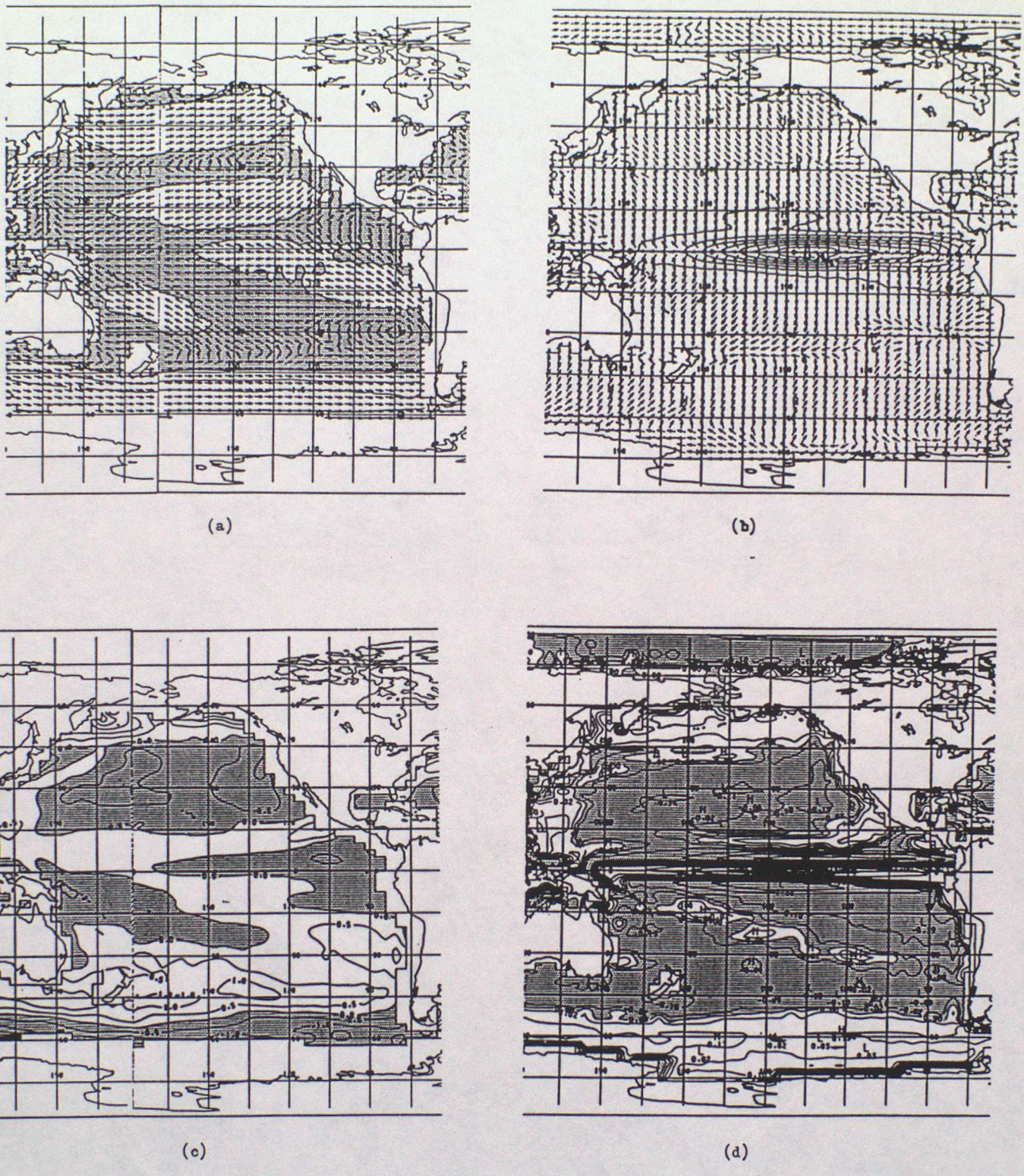

Figure 6.13 Results for the Pacific from a 30 day barotropic integration of the Bryan/Semtner model showing (a) the imposed annual mean wind stress (from Han and Lee, 1981); (b) the 50 m deep surface layer velocity field (isotachs and direction arrows); (c0 the curl of the wind stress and (d) the vertical motion at 50m depth: regions of downwelling are shown shaded.

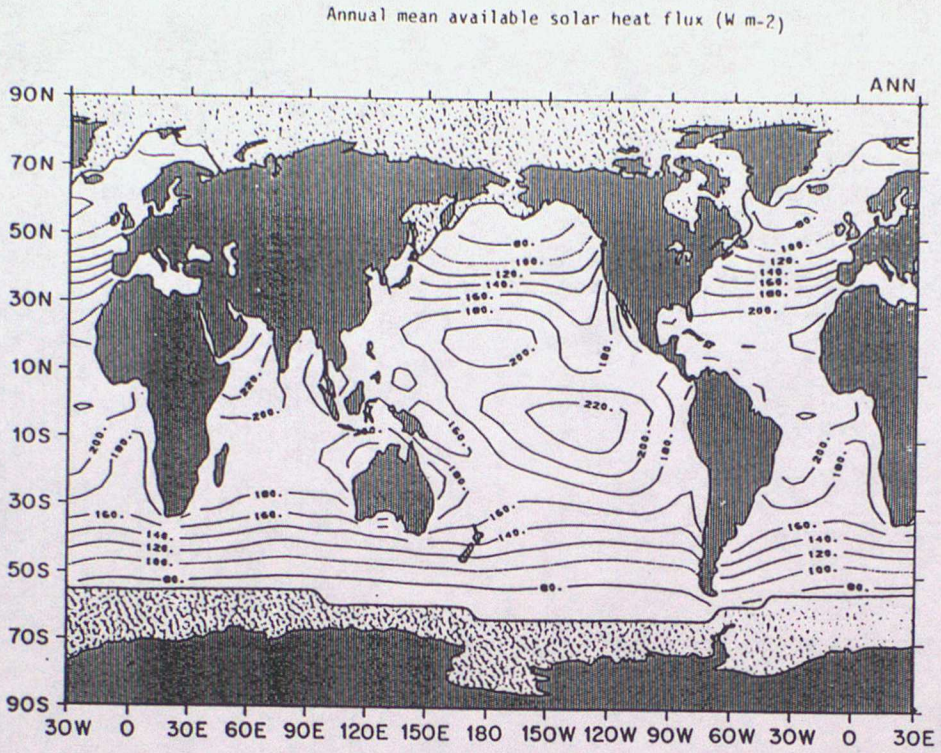

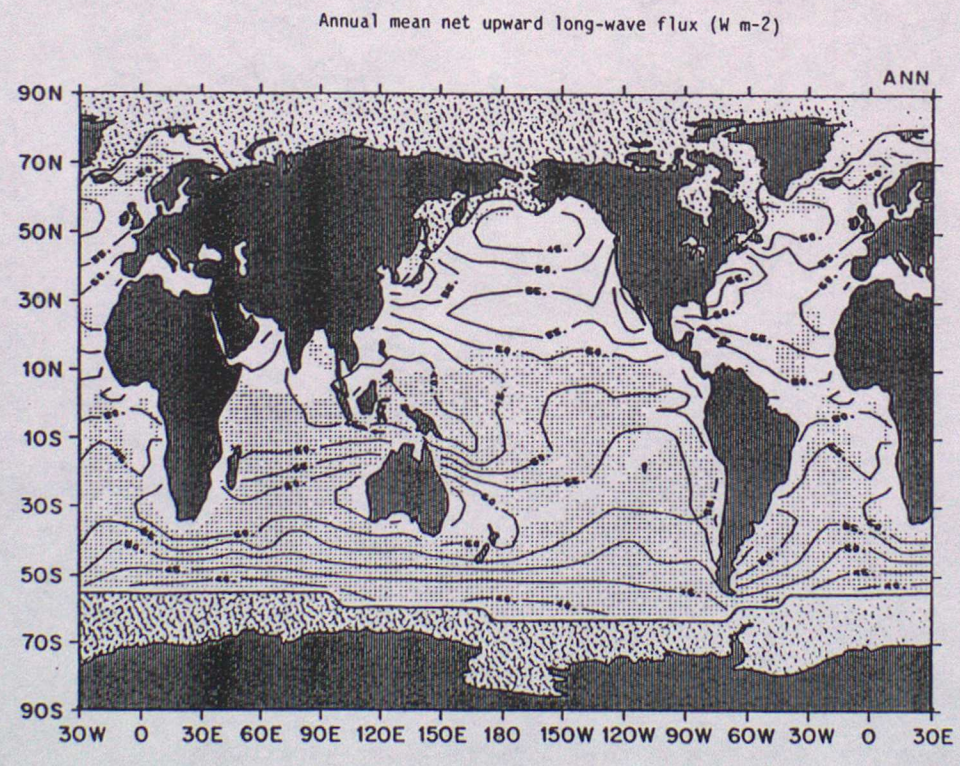

Figure 6.14 Components of the heat balance at the ocean surface. (From Esbensen and Kushnir, 1981)

Annual mean sensible heat flux (W m-?)

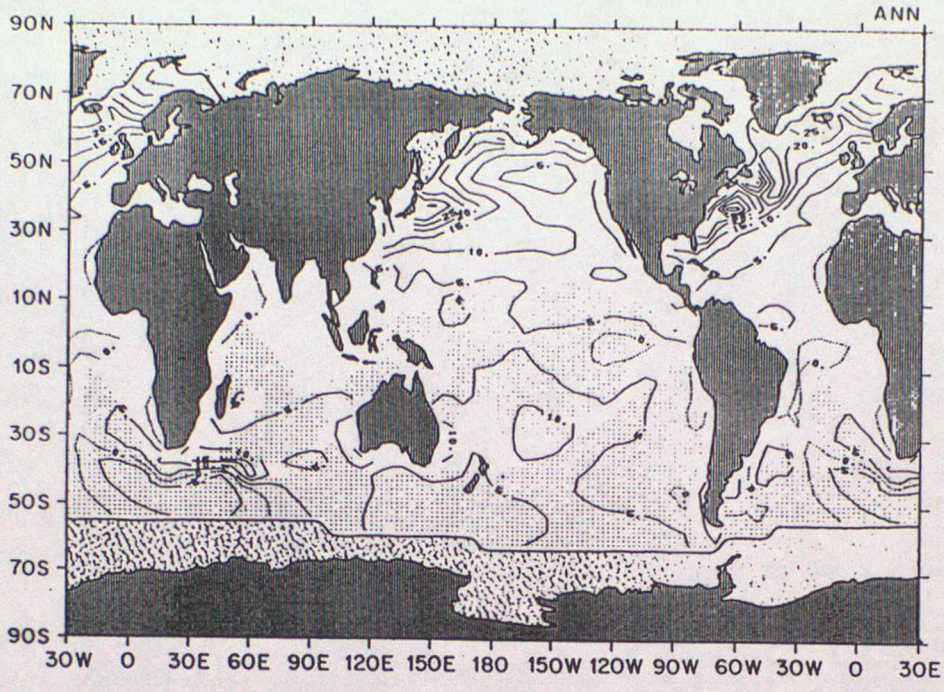

Annual mean latent heat flux (W m-?)

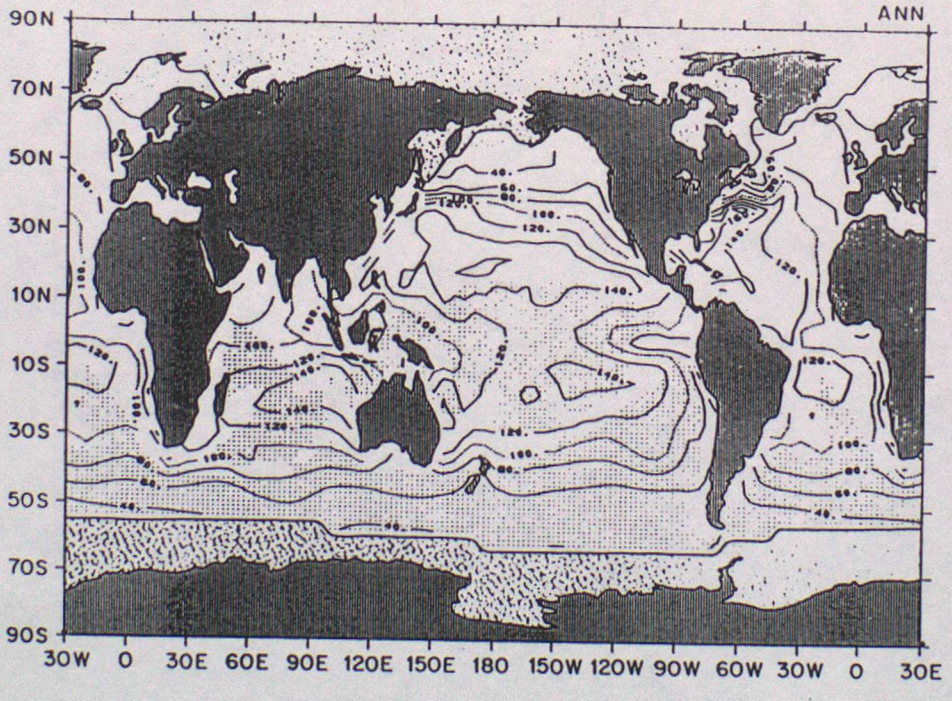

Figure 6.14 (continued)

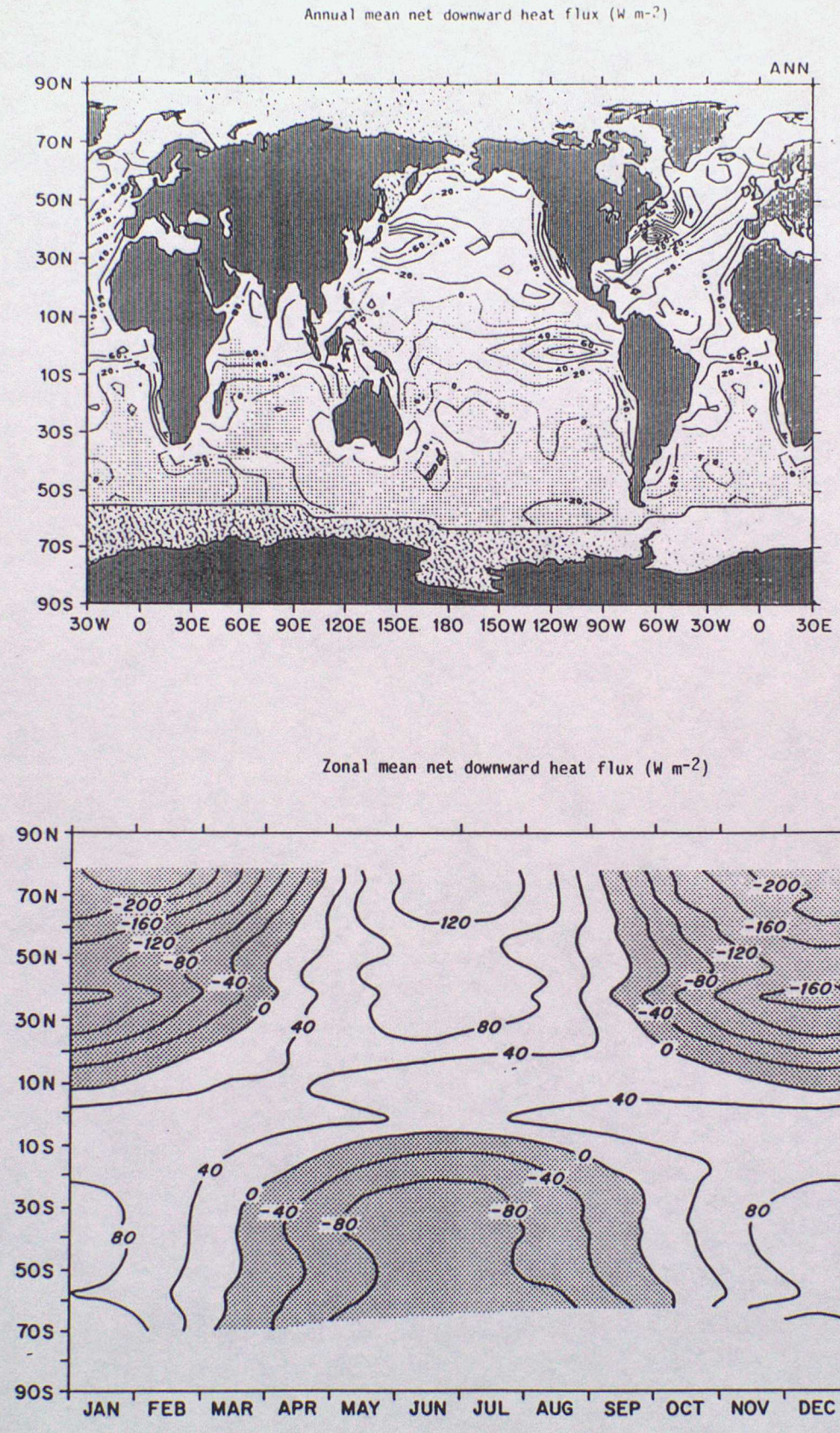

Figure 6.15 Annual mean (a) and seasonal variation of the zonal mean net downward heat flux (b) at the ocean surface. (From Esbensen and Kushnir, 1981)

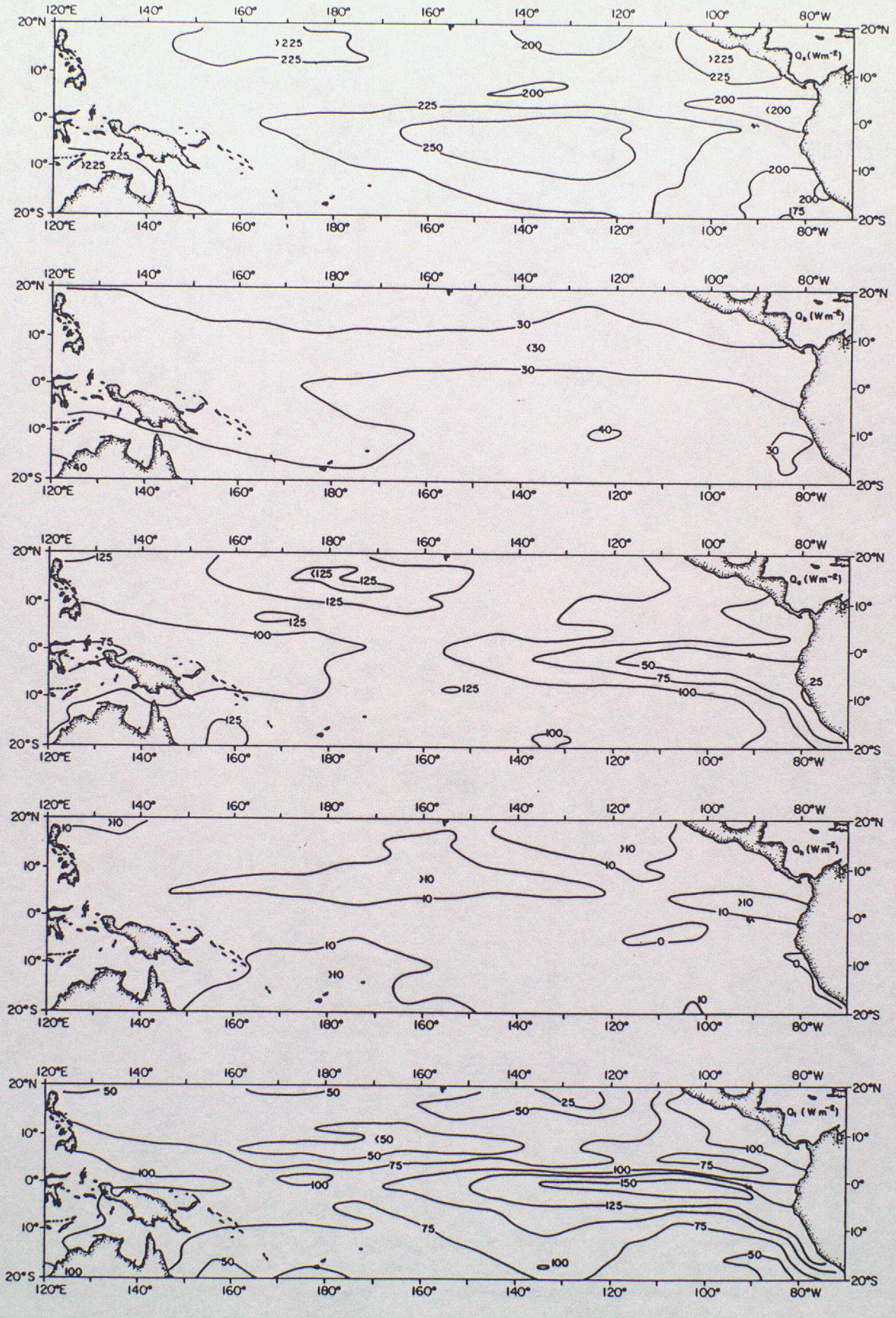

Figure 6.16 In order from the top, mean annual distribution for the tropical Pacific of absorbed solar radiation; net longwave radiation; latent heat flux; sensible heat flux; and net or total heat flux. Units are W m^{-2} and the data are for 1970-79. (From Reed, 1985).

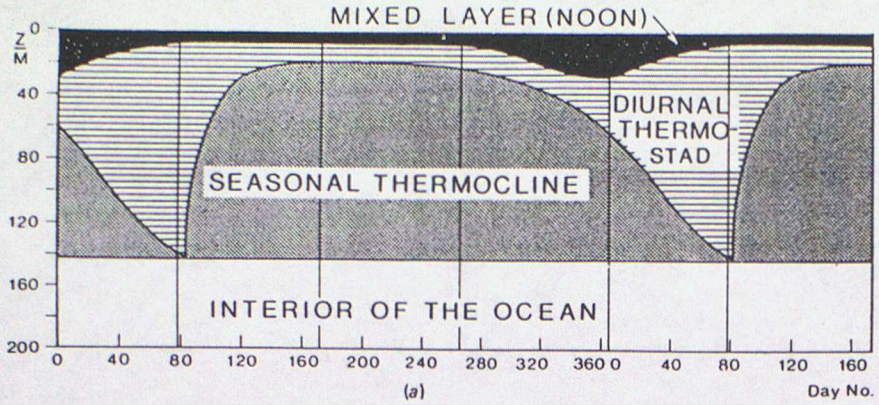

(a)

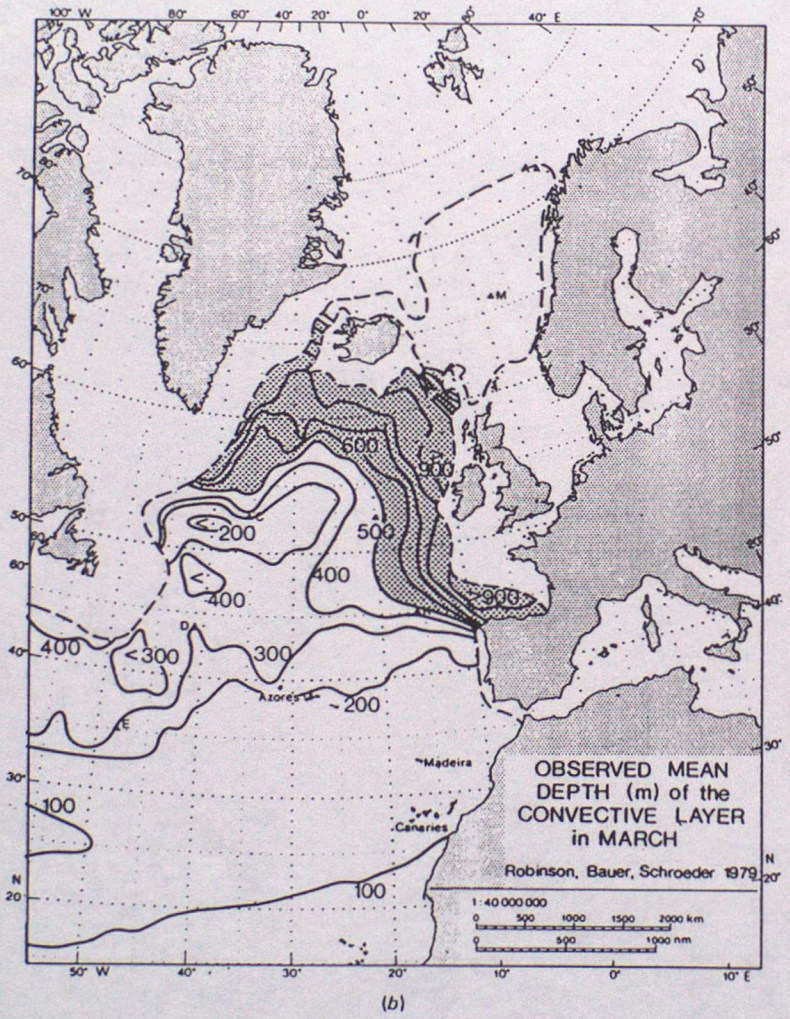

(b)

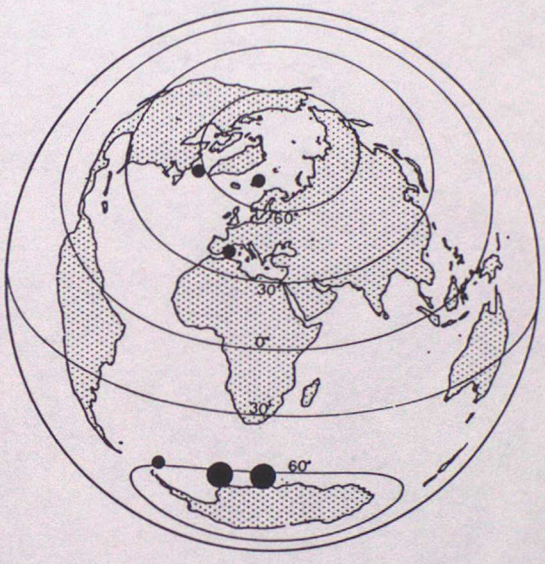

(c)

Figure 6.17 (a) The daily maximum and minimum depths of the mixed layer at 43° N according to Hofmann's (1982) model at a site where the annual surface heat flux is zero. (b) The regional variation of the annual maximum depth of the convection layer of the north-east Atlantic, deduced from bathythermograph data by Robinson, Bauer and Schroeder (1979). (c) The locations of the few sites at which it is known that convection can extend to the ocean bed, according to Killworth, 1983. Convection at these sites ventilates the deepest levels of the ocean at a rate that gives water mass residence times of many centuries. (From Woods, 1984)

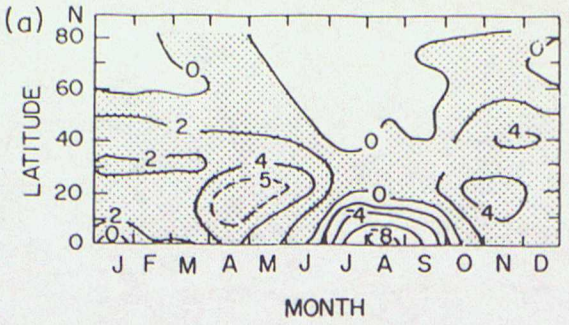

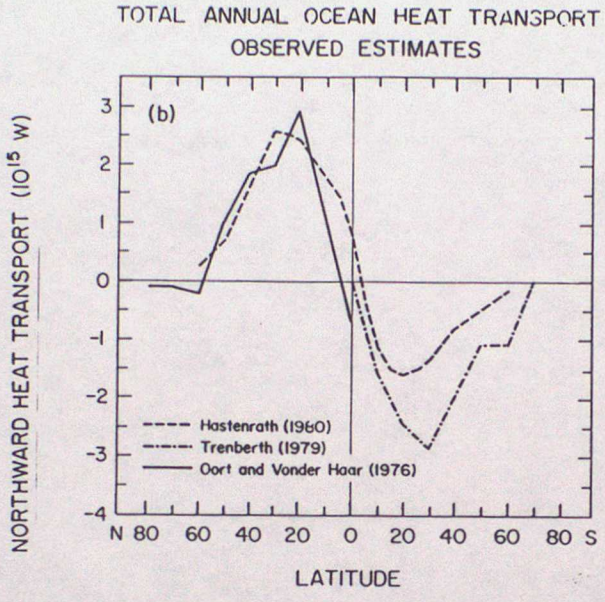

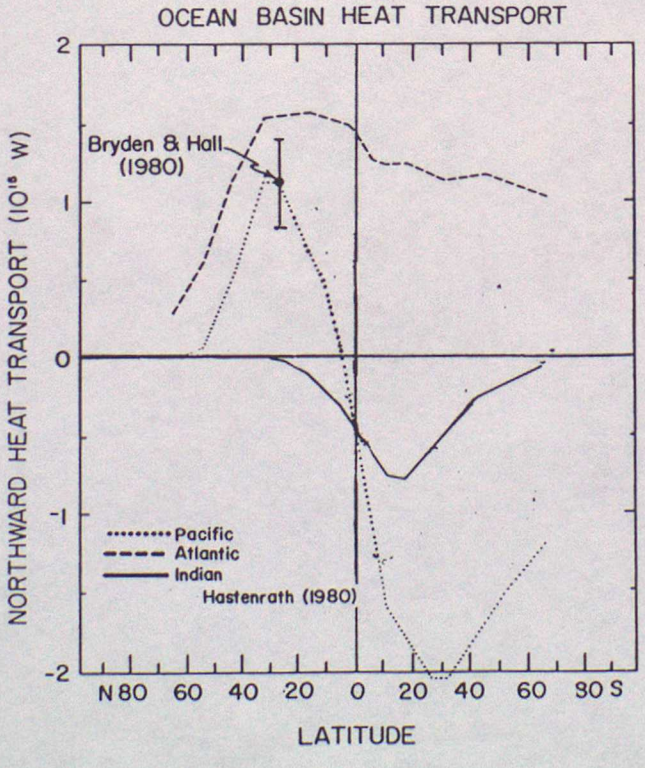

Figure 6.18 (a) Northward flux of heat in the oceans (10^{15} W) calculated from obsevations by Oort and Vonder haar (1976). (b) Observed estimates of the total annual transport of sensible heat. (c) Ocean basin heat transports as estimated from observations by hastenrath (1980). Also plotted is an estimate for the Atlantic from Bryden and Hall (1980).

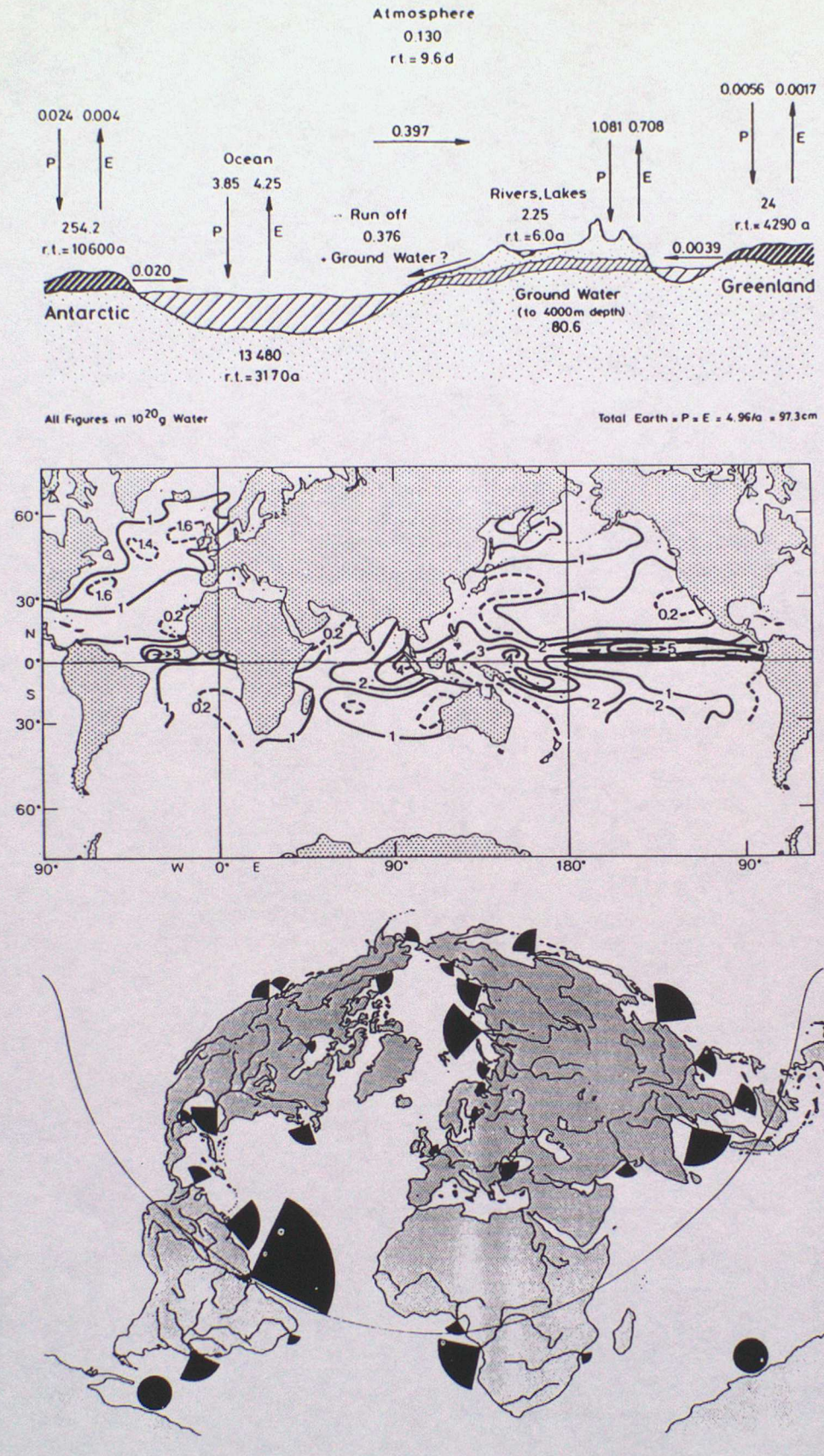

Figure 6.19 (a) The global water balance shown schematically on the basis of data in Baumgartner and Reichel (1975). (b) The global pattern of annual mean rainfall over the ocean based on ship observations (after Dorman, 1981). (c) The flow of freshwater from the continents into the oceans. The areas of the segments are proportional to the annual volume flow from each river assuming a depth of 1m. The iceberg flow from Antarctica is shown as two discs, scaled similarly. (From Woods, 1984)

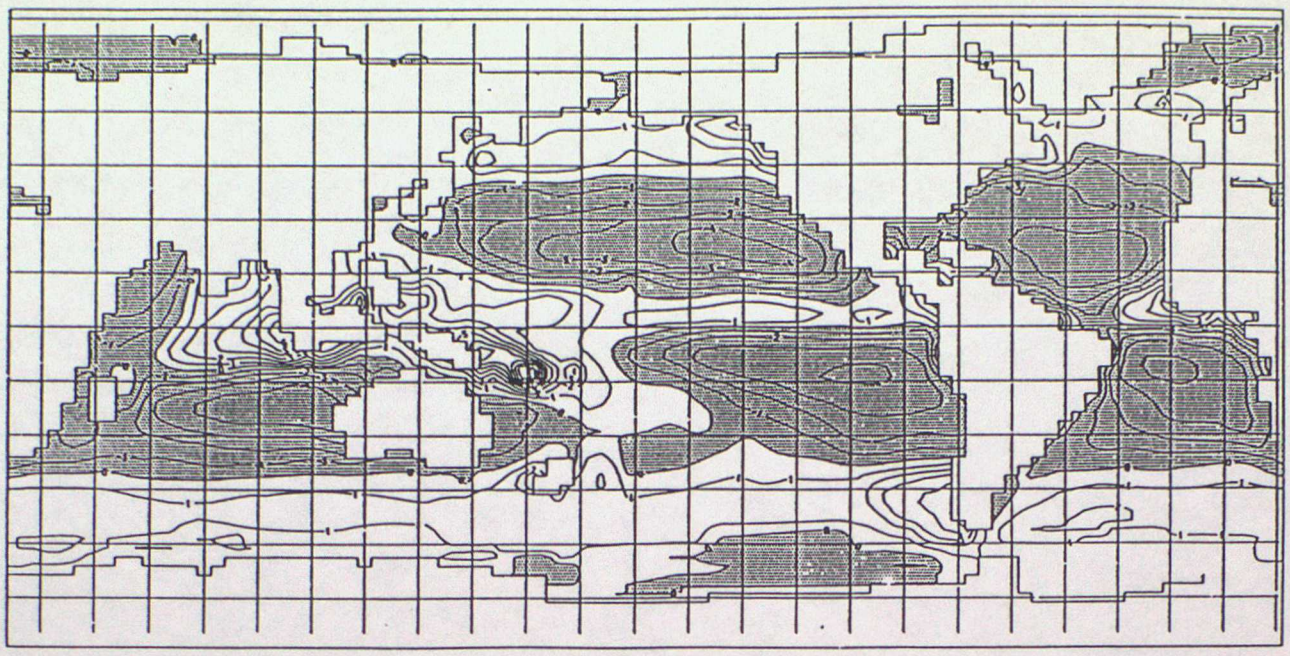

Figure 6.20 Annual mean precipitation less evaporation flux. (rainfall is taken from Schutz and Gates (1971-74), and evaporation data fromEsbensen and Kushnir (1981)). Contour interval is 1 mm day^{-1}; negative areas correspond to an excess of evaporation over precipitation.

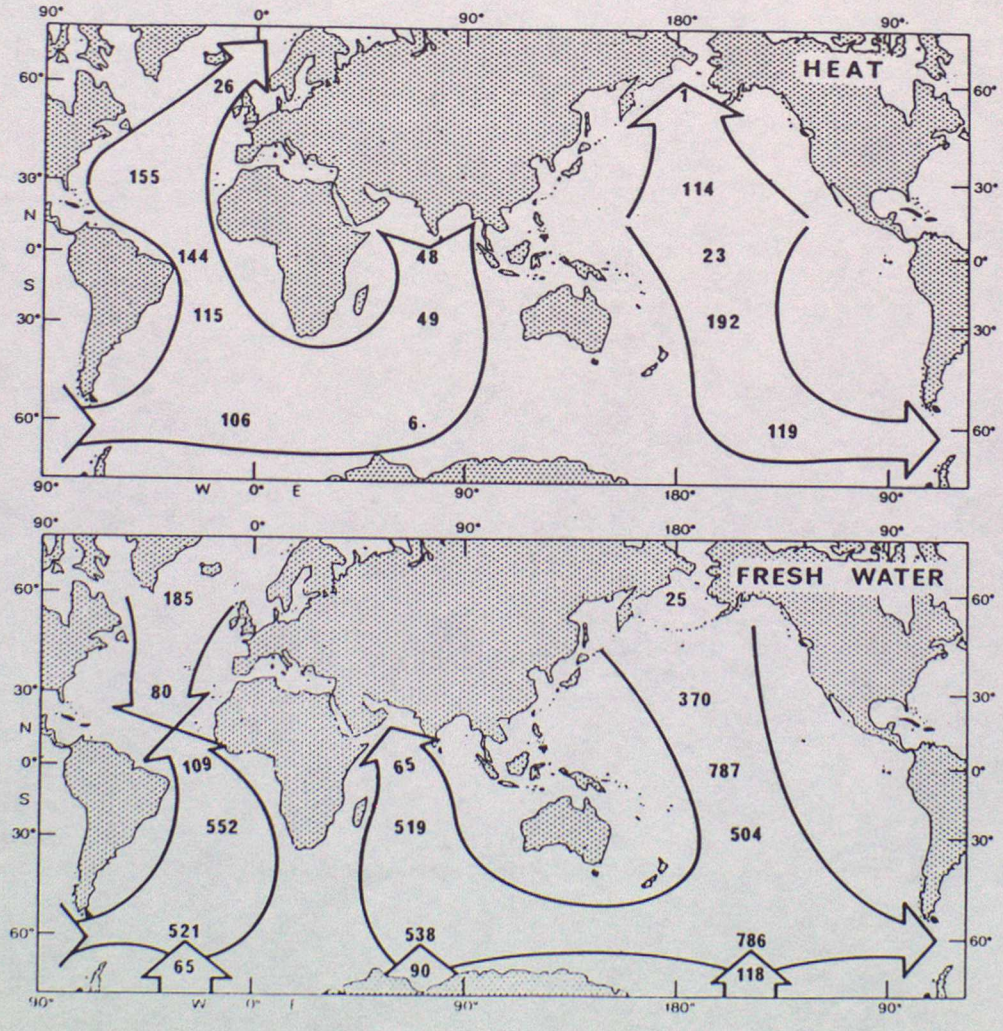

Figure 6.21 The circulation of heat (10^{15} W) and freshwater (Kt s^{-1} around the ocean as (tentatively) deduced by Stommel (1979) and Baumgartener and Reichel (1975) from the global pattern of energy and water fluxes from the ocean to atmosphere (plus continental run off).

PHYSICS AND DYNAMICS OF THE CLIMATE SYSTEM

THE OBSERVED OCEAN CIRCULATION

H Cattle

Met O 20, Meteorological Office Bracknell

7.1 INTRODUCTION

In this lecture, we shall discuss some of the observed features of the ocean circulation. As for the atmosphere, motion systems occur on a variety of scales, some indication of which is given in the kinetic energy diagram of Figure 7.1. We shall in this lecture discuss some aspects of most of these systems, but shall begin by briefly considering the observed large scale ocean surface current field.

7.2 THE OCEAN SURFACE CURRENT FIELD

Figure 7.2 shows the primary currents of the world's oceans. On the very large scale, are found clockwise circulations (gyres) in the northern basins of the Atlantic and Pacific, with counterclockwise circulations in the southern basins of these and the Indian ocean. A marked feature of these gyres is the presence of an intense boundary current on the western sides of the oceans of which the Gulf Stream and Kuroshio are prime examples. Equatorial countercurrents flow from west to east near the equator, with north and south equatorial currents to the north and south flowing from east to west in association with the trade winds. To the south of the major ocean basins lies the Antarctic Circumpolar Current, which itself is important for inter-basinwater mass exchange. The North Atlantic also exchanges water mass with the Arctic Ocean to the north, as the North Atlantic Current, an extension of the Gulf Stream, transports North Atlantic surface water into the Arctic both to the west and east of Spitzbergen, whilst the East Greenland current transports surface water (and sea ice) from the Arctic to the North Atlantic through the Fram Strait. Similarly, the West Greenland current brings relatively North Atlantic warm water into the Davis

Strait and Baffin Bay, while the Labrador Current brings colder water and ice back to the North Atlantic.

The basic current pattern in the Indian Ocean is notable for a seasonal reversal of currents off the east coast of Africa near Somalia (Figure 7.3). During winter, the northeast trades from India drive the waters towards the south, whereas when the summer Indian monsoon sets in the southwest trades in the Arabian Sea drive the water towards the north. This total reversal dramatically illustrates the response of current systems, including the north and south equatorial currents and the large scale gyres, to the major wind patterns, aspects of which we shall now consider, following the treatment in Pond and Picard (1978).

7.3 SVERDRUP'S SOLUTION FOR THE WIND-DRIVEN CIRCULATION

7.3.1 Sverdrup theory

Assuming negligible accelerations and friction from horizontal gradients of velocity (which as we shall see are important for the boundary current flows), the equations of motion are:

$$\alpha\, \partial p/\partial x = fv + \alpha\, \partial \tau_x/\partial z$$

$$\alpha\, \partial p/\partial y = -fu + \alpha\, \partial \tau_y/\partial z \qquad (7.1)$$

where $\alpha = 1/\rho_w$, u and v are the components of the current and τ_x and τ_y the components of the turbulent stress. If we denote the total wind driven transport by the ocean current systems in the x (W → E) and y (S → N) directions by M_x and M_y respectively, then these are given by:

$$M_x = \int u\, dz$$

$$M_y = \int v\, dz \qquad (7.2)$$

where the integrals are taken from the surface, 0, down to a depth, -h, where the wind driven flow is zero (assumed above the ocean bottom). By continuity,

$$\partial M_x/\partial x + \partial M_y/\partial y = 0 \qquad (7.3)$$

Subtraction of the equations of motion (7.1) differentiated wrt y and x respectively and integrated wrt z between 0 and -h, use of expressions (7.2) and (7.3) and remembering that $\partial f/\partial x = 0$, yields:

$$M_y \, \partial f/\partial y = \partial \tau_y/\partial x - \partial \tau_x/\partial y \qquad (7.4)$$

or:

$$\beta \, M_y = \mathrm{curl}_z \, \boldsymbol{\tau} \qquad (7.5)$$

Here $\beta = \partial f/\partial y$ and $\boldsymbol{\tau}$ is the surface stress. Equation (7.5) or, equivalently, (7.4) is called the *Sverdrup equation.*

7.3.2 Orders of magnitude of the terms

To get a feel for the magnitude of the terms involved, consider a position in the North Atlantic at about 35° N. If the wind, assumed to be of 7-8 m s^{-1} from the west, falls to zero in the north-south direction on a scale of 1000km, then, since $\tau_x \simeq 10^{-1}$ N m^{-2} and $\beta \simeq 2 \times 10^{-11}$ m^{-1} s^{-1}:

$$M_y = (1/\beta) \, \mathrm{curl}_z \, \boldsymbol{\tau} \simeq -5 \times 10^{3} \text{ kg } m^{-1} \, s^{-1}$$

This value for M_y is for a strip of ocean only 1 m wide, so that for a 5000 km wide ocean across which there is a constant wind, the southward flow would be of order 25×10^{9} kg s^{-1} in mass, 25×10^{6} m^3 s^{-1} in volume or, equivalently, 25 Sverdrups (c.f. Figure 7.3(b) below)

Note that, in places where $\mathrm{curl}_z \, \boldsymbol{\tau}$ is zero, there will be no northward or southward mass transport. Although there may be flows which when vertically integrated cancel, nevertheless, lines along which $\mathrm{curl}_z \, \boldsymbol{\tau}$ is zero form natural boundaries which separate the flow into gyres. This is demonstrated by Figure 7.4 which shows the mass transport streamfunction (for which $M_x = \partial\psi/\partial y$, $M_y = -\partial\psi/\partial x$) in Sverdrups from a barotropic model integration forced only by the observed wind stress. Note the approximate correspondence to gyres shown in the surface current field in Figure 7.2.

7.4 THE EQUATORIAL CURRENT SYSTEMS

Sverdrup applied his equations, (7.3) and (7.5), to the trade wind zones on the eastern sides of the oceans in lower latitudes where τ_y and $\partial\tau_y/\partial x$ can be considered small compared to their x-component counterparts. He related large scale characterisics of the mass transport of these systems to the sign of $\partial^2\bar{\tau}_x/\partial y^2$ where the 'bar indicates a horizontal average (see Figure 7.5, taken from Pond and Picard, 1978). In particular it turns out that:

(a) north of about 15° N and south of about 2° N where the value of $\partial^2\bar{\tau}_x/\partial y^2$ is positive, the transport M_x is negative and so to the *west* (North Equatorial current and the South Equatorial current)

(b) between 15° N and 2° N (doldrums), where the value of $\partial^2\tau_x/\partial y^2$ is negative M_x is positive and so is to the *east* (North Equatorial Counter Current).

The Figure shows qualitatively how Sverdrup's solution accounts for the existence of the gross features of the equatorial current system, though note that the detailed structure of this current system is, in fact more complex than this as we shall indicate below. Note also that the system is not symmetrical about the equator, but is displaced to the north of it, consistent with the general displacement of the trades. Remember also that the Sverdrup equations give the integrated mass transport, but no details of the velocity distribution with depth.

The equatorial current systems can also be related in a rather different way to the general pattern of vertical motion and pressure gradients induced by the effects of the wind driving on the ocean surface (Wells, 1986). We have already noted, in Lecture 6, the effects of the wind stress in inducing strong upwelling in equatorial regions, with downwelling to the north and south. The equatorial upwelling is of the order 1 m day^{-1} and causes a lifting of the thermocline. Locally, where upwelling is strong, the equatorial thermocline may be less than 50 m below the surface, whilst the downwelling to the north and south keeps it depressed further below the surface. The meridional tilt of the thermocline caused by these upwelling and downwelling patterns (Figure 7.6) has the effect of inducing a meridional pressure gradient, with high dynamic height polewards of the equator. A few degrees of latitude

from the equator, the flow will be close to geostrophic and therefore the flow within the thermocline will be westward. It is this meridional pressure gradient which is responsible for the north and south equatorial currents which are found in all ocean basins, except in the Indian ocean during the southwest monsoon. In the latter case, downwelling is induced on the equator, the meridional pressure gradient is reversed and eastward currents occur. Note that a downwelling region in the eastern Atlantic and eastern Pacific at about 10° N (but reflected in Figure 7.6 at about 5° N) and again associated with the wind pattern there (see the discussion of Sverdrup balance above) results in a similar reversal of the pressure gradient and induces a narrow countercurrent towards the east at that latitude.

Along the equator the primary balance of forces in the upper ocean is between the pressure gradient force and the surface wind stress. As a result of the wind on the surface the highest dynamic heights are found in the west and here the thermocline is depressed relative to the east (Figure 7.7). The upward slope of the thermocline towards the east accounts for the frequent appearence of cold upwelling water in the eastern equatorial Atlantic and Pacific Oceans (c.f Figure 6.13(d)). In the Indian Ocean, during the southwest monsoon, the zonal tilt of the thermocline is reversed.

If the horizontal pressure gradient exactly balanced the surface wind stress, there would be no surface motion along the equator. However, the balance of forces is not exact and the currents respond quickly to the imbalance (see below). Below the surface layer, unimpeded by the wind stress, the eastward pressure gradient in the thermocline drives an eastward undercurrent along the equator (Figure 7.8). In the Pacific Ocean, the undercurrent is about 14,000 km long, but only 400 km wide. It is confined to within 2° of the equator and has a maximum velocity of 2 m s^{-1} close to its core in the thermocline. In both the Pacific and Atlantic Oceans the undercurrent slopes upwards towards the east and can, occasionally, surface in the eastern basins.

7.5 THE EL NINO

The strong coupling between the atmosphere and ocean of equatorial latitudes is symptomised by the El Niño-Southern Oscillation phenomenon.

As noted in Lecture 6, there is, in the climatic average, a marked sea surface temperature difference between the warm water of the western Pacific and the relatively cool water in the eastern Pacific. When this temperature contrast is reduced, due to the cessation of upwelling cool water on the eastern side, El Niño sets in. It occurs with differing intensity two or three times each decade. Anomalously warm water, perhaps 2-4 C above normal appears off the coast of Peru and Equador. It has become recognised that El Niño is just one symptom of a world-wide atmospheric event, with the oceanic component primarily manifest in the eastern tropical Pacific Ocean. Figure 7.9 shows the sea surface temperature anomaly in the in December 1982. This was associated with one of the largest El Niño events of the last 100 years, the anomaly covering an area equivalent to about 10% of the global ocean surface. The atmospheric impacts of El Niño will be discussed in the series on **Climates of the World**. We will therefore confine ourselves to a brief discussion of some of the ocean aspects here.

The El Niño event is initiated by a collapse of the South Pacific high, which itself appears to be initiated by other, shorter time-scale, air-sea interactions. The weakening of the trades causes the water that is piled up on the western side of the ocean to start flowing to the east in association with a Kelvin wave (see Lectures 2/3) which propogates across the Pacific (Figure 7.10) over several months, with subsequent propogation of Rossby waves to the west. As a result, there is a reduction in the westward tilt of the equatorial thermocline which in turn represents a movement of the sub-surface cold water in the eastern Pacific away from the surface. The large net surface heat flux, between 50 and 100 W m^{-2} (see Lecture 6) into the eastern Pacific implies that the surface mixed layer will, in the asociated reduction of cold upwelling, warm steadily by about 2 C in three months over a depth of 100m. Some additional warming will also occur by advection of warmer water from the central Pacific to the east when the thermocline relaxes. The overall increases in sea surface temperature move the region of highest sea surface temperature from the western towards the central Pacific. The atmospheric convergence zones tend to follow the region of highest sea surface temperature and so they are correspondingly displaced. The subsequent changes in sea surface temperatures affect the wind circulation and eventually cause the interaction cycle to revert back to to pre-El Niño conditions. The whole progression of changes takes between 1 and 2 years on average to complete, from the

reduction in the South Pacific high to the final decay of the sea surface temperature anomalies.

7.6 WESTWARD INTENSIFICATION

We have already noted that a marked feature of the ocean circulation in mid-latitudes is the intensification of the polewards flow on the western side of the main subtropical gyres, with associated large gradients of temperature there. The explanation of the strong flow in these regions of the wind driven gyres was first given by Stommel (1948) and further developed by Munk (1950). Here we shall use an argument based on conservation of potential vorticity (see, e.g. Pond and Picard, 1978; Hasse and Dobson, 1986, whom we follow here).

In the northern hemisphere, we have seen (Lecture 6, Figure 6.13(b)) that the reversal in wind direction at mid-latitudes from high latitude westerlies to low latitude trades, results in oceanic Ekman transports which are oppositely directed in the two wind regimes. These Ekman transports result in some piling up of the water in the convergent zone, the effect of the wind being to impart a generally clockwise upper layer oceanic circulation. The essential factor which provides the explanation for the westward intensification is then the variation of the Coriolis parameter with latitude (Figure 7.11). Ignoring for the sake of argument the effect of variations of depth, d, conservation of potential vorticity:

$$(\zeta + f)/d = \text{constant}$$

means that, on the western side of the ocean, the resultant polewards travelling water gains in clockwise spin both from the wind and from its polewards motion, consequent upon the increase in f (Figure 7.12). The result of this is to intensify the polewards flow, leading to the development of a strong western boundary current and inducing horizontal shears until a balance is developed between the clockwise spin gained from the wind and by the polewards motion and that lost by lateral friction at the boundary. On the eastern side of the ocean, the equatorwards travelling water acquires clockwise spin relative to its surroundings as a result of the change in f, which offsets the continued

input of clockwise vorticity from the wind so that velocities and shears remain much lower.

On the longer timescale the convergence of the Ekman flow results in downwelling which causes the lighter surface water to push downwards on the heavier water below the permanent thermocline and force the deep water outwards. The effect of this can be seen in the horizontal temperature field at depth (Figure 7.13). The rapid flow of water in the western boundary currents carries heat from lower latitudes polewards. In the northern hemisphere this contrasts with the cold water being driven south by the Labrador current in the Atlantic and the Oyashio in the Pacific and yields associated regions of intense horizontal temperature gradient (Figures 7.2 and 6.5). In the Atlantic in particular, the isotherms of the Gulf Stream spread out to the north and east with the North Atlantic Drift (Figures 6.5 and 7.14), with warm water pentrating up into the Norwegian Sea and producing an amerliorating effect on the climate of western Europe. A similar effect is also present in the Pacific, but because of the presence of the coastal boundaries and the width of the basin it does not have such a marked effect on the climate of western North America.

7.7 MESOSCALE OCEANOGRAPHY

7.7.1 Ocean eddies

Over the past several decades the importance of oceanic eddies for the general circulation has gradually been recognised. In some ways they are the dynamical equivalent of the "synoptic scale" disturbances of the atmosphere, but are of much smaller scale being of order tens to 300 km or so across, consistent with their characteristic Rossby radius (Lectures 2/3). Eddies influence the general circulation of the oceans through eddy-mean field interaction and eddy-eddy interaction. Such interactions occur most strongly in intense current systems. In this context, the role of eddy momentum flux divergence is thought to be an important contributor to recirculation of the Gulf Stream. Heat transport by Southern Ocean eddies is considered important to the global heat budget whilst eddies are also thought to transport heat significantly in the region of the Gulf Stream. On the smaller scale, eddies interfere with frontal and long wave generation processes at the

shelf break and with surface layer circulation and mixing, and hence with mass exchange over the continental slope and shelf (Csanady, 1979). Eddies have now been found in most parts of the oceans, but the distribution of synoptic types and eddy activity is spatially heterogeneous and intermittent. The most vigorous variabilty is associated with intense flow regions such as the Gulf Stream. By way of illustration, Figure 7.15 shows a schematic of a typical instantaneous flow pattern together with an observed flow pattern for the North Atlantic.

7.7.2 Gulf Stream rings

The Gulf Stream is a constantly changing meandering stream that often forms large loops which occasionally cut off from the main current forming pinched-off 'rings' (Figure 7.16). These can either be cold-core and (characteristically for the Northern hemisphere) rotating counterclockwise (i.e. cyclonically), when pinched off equatorward of the Gulf Stream or warm-core and rotating clockwise, when pinched off poleward. An example of a cold core Gulf Stream ring is shown in Figure 7.16. Similar, but not identical rings are spawned by the Kuroshio. The eddy is seen to consist of a well defined area of water 50-100 km in diameter, typically cooler than its surroundings by about 5 C. It has, associated with it, approximately geostrophically balanced currents with tangential velocities of up to 1m s^{-1} in the core. In the Gulf Stream the typical vertical extent of the rings is 1500 m. The density distribution within the rings shows the main pycnocline to be as much as 500-600 m closer to the surface than the surrounding ocean, whilst the sea surface is depressed by about 0.4 to 0.5 m. By contrast, warm core eddies are characterised by a sea surface elevation and depression of the main thermocline, both of the same order of magnitude as for the cold core eddies.

The eddies are spawned from the Gulf Stream at the rate of 5 to 8 per year on each side of the Stream. Their life time, before decaying or being reabsorbed, is up to two years for cold core and less than one year for warm core rings. They move at rates of 2 to 10 km day^{-1} and, in the generally southerly Gulf Stream recirculation region tend to move in a southwesterly direction. To see the reason for the southwesterly drift, consider a cold core, counterclockwise rotating eddy which is in geostrophic equilibrium, so its pressure gradients are balanced exactly

by the mean Coriolis force at its central latitude. Since water equatorwards of the central latitude has higher cyclonic angular momentum (as measured by $\zeta + f$) than the water polewards of the central latitude, the equatorwards water will turn poleward with a slightly smaller radius of curvature than that originally moving polewards on the opposite side. This effect, due to the latitudinal variation of the Coriolis parameter, causes all eddies, warm core and cold core, to propogate westwards.

7.7.3 Frontal processes

Oceanic fronts, which we only briefly consider here, are, as their name implies, boundaries between water masses with dissimilar properties. They are often marked at the surface by disturbances of the waves there or by lines of foam or debris. They generally have associated with them regions of convergence and relatively strong vertical motions and may occur at any depth, including the vicinity of the sea bottom. They are also regions across which strong mixing of the water properties on either side can occur (for a review see Garrett, 1982). Following Bowman and Esaias (1978) (Hasse and Dobson, 1986) they may be classified into six types, according to their scale and dynamical origin:

Planetary fronts are those associated with large scale convergence of surface Ekman transports, and are typically found in mid-ocean. A good example is the Antarctic Convergence Zone, or Polar Front (see Figure 7.17), which is at about 60° S and forms the northern limit of the so-called Antarctic surface water formed by ice melt in summer and surface cooling in winter.

Western boundary current edges often behave as fronts, since warm, salty tropical water is brought into relatively close proximity with cold, fresh high latitude water by the western boundary currents.

Shelf break fronts are formed at the edges of continental shelves where waters characteristic of the shallow shelf regions meet and mingle with the water types typical of the continental slopes and deep ocean.

Upwelling fronts (see Figure 7.18) are generally associated with offshore Ekman transports generated by alongshore winds. They are

characterised by a pycnocline that reaches the surface with surface water offshore and deep water at the surface inshore. Such fronts are commonly found off the west coasts of the continents (California, Peru, Africa). They interact strongly with the local meteorology and are one of the few locations in the globe where waters beneath the permanent pycnocline come into direct contact with the atmosphere. They thus act as important pathways by which airborne particles and gas can be exchanged with the deep ocean.

Plume fronts occur on the boundaries of fresh water discharge plumes produced by large rivers such as the Amazon. They act to stir the fresh runoff waters, with their load of terrestrial solutes into the ocean.

Finally, shallow sea fronts are formed in shallow seas and estuaries and around islands, capes etc. They form in the boundary between well-stratified offshore waters and waters in the shallow seas, which are well mixed by waves and tides. In general they are local phenomena (Figure 7.19).

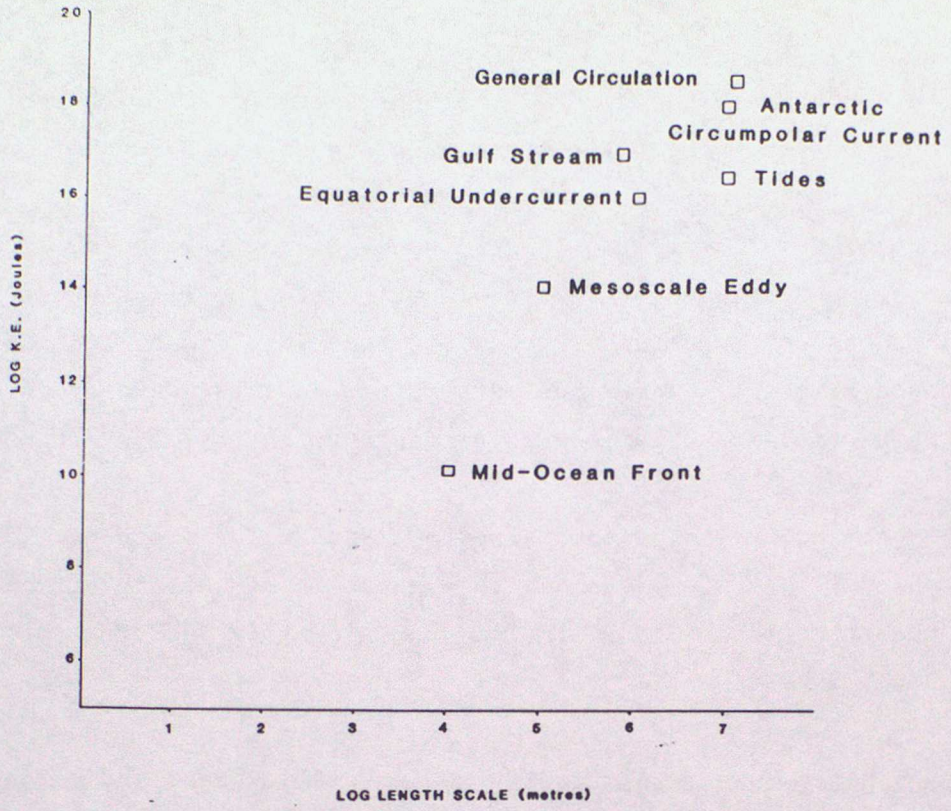

Figure 7.1 Kinetic energy of oceanic phenomena. (From Wells, 1986)

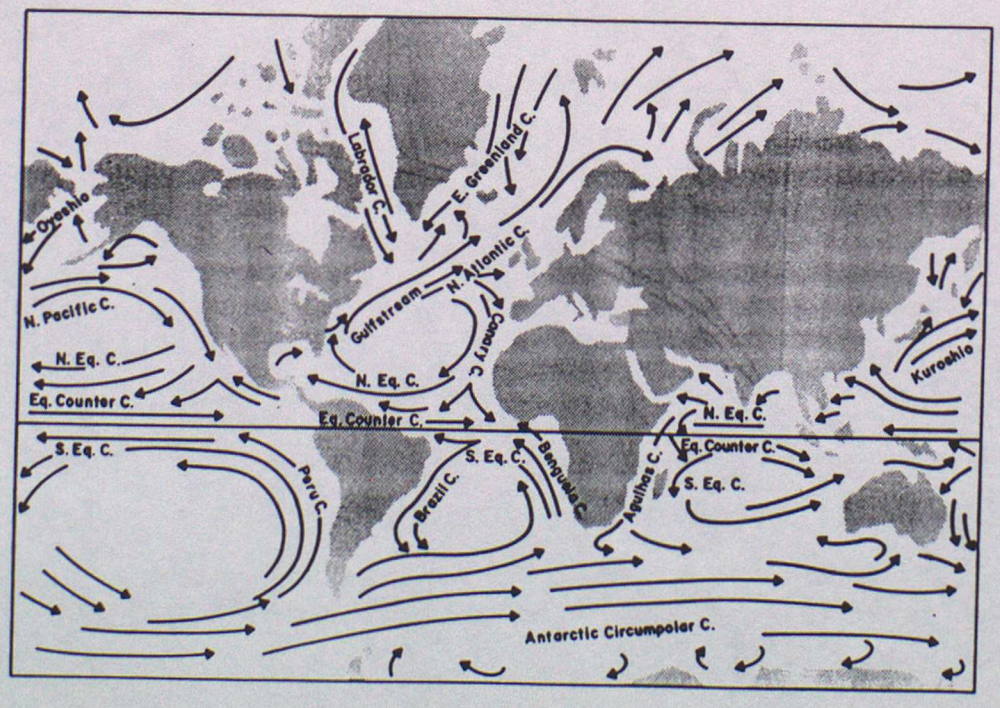

Figure 7.2 Schematic of the Earth's major surface currents

(a)

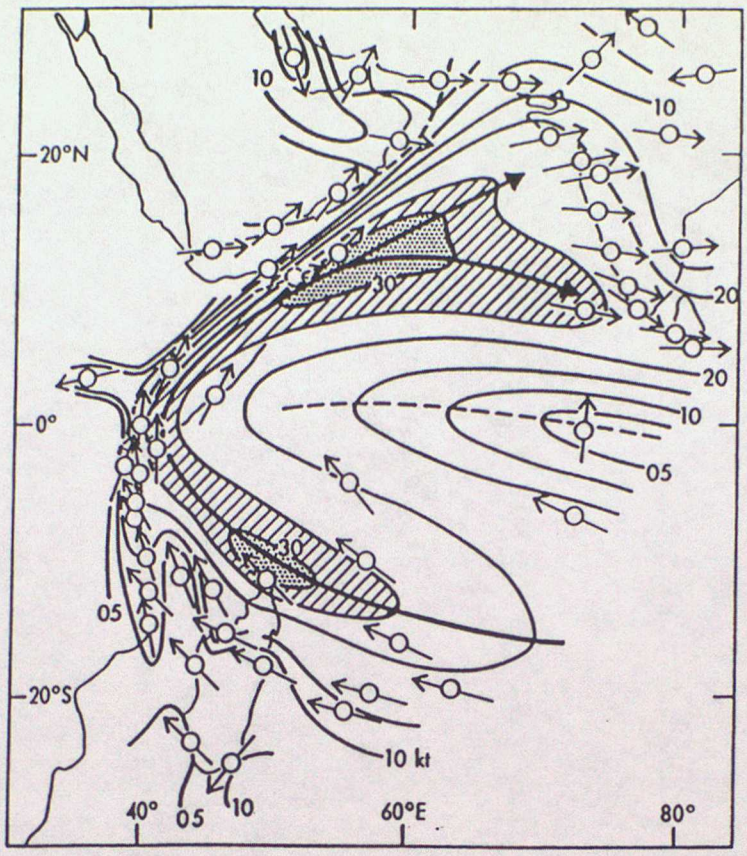

(a) East African jet in atmosphere: monthly mean air flow at 1 km in July. Wind speeds at 5 knot intervals. (Reproduced from J. Findlater, Geophysical Memoirs, *No. 115, figure 1, with permission of HMSO (London).) (b) Somali jet in the Indian Ocean. (Reproduced from J. C. Swallow and J. G. Bruce (1966),* Deep Sea Research, **13**, *866, figure 2, with permission of Pergamon Press.)*

(b)

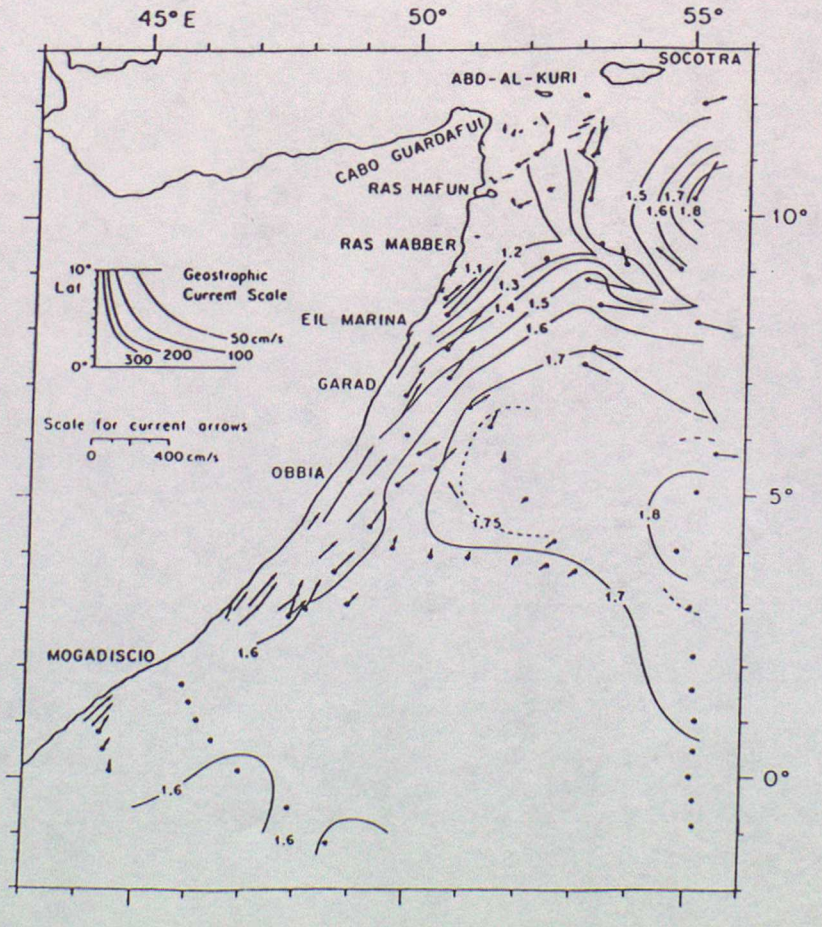

Figure 7.3
7.13

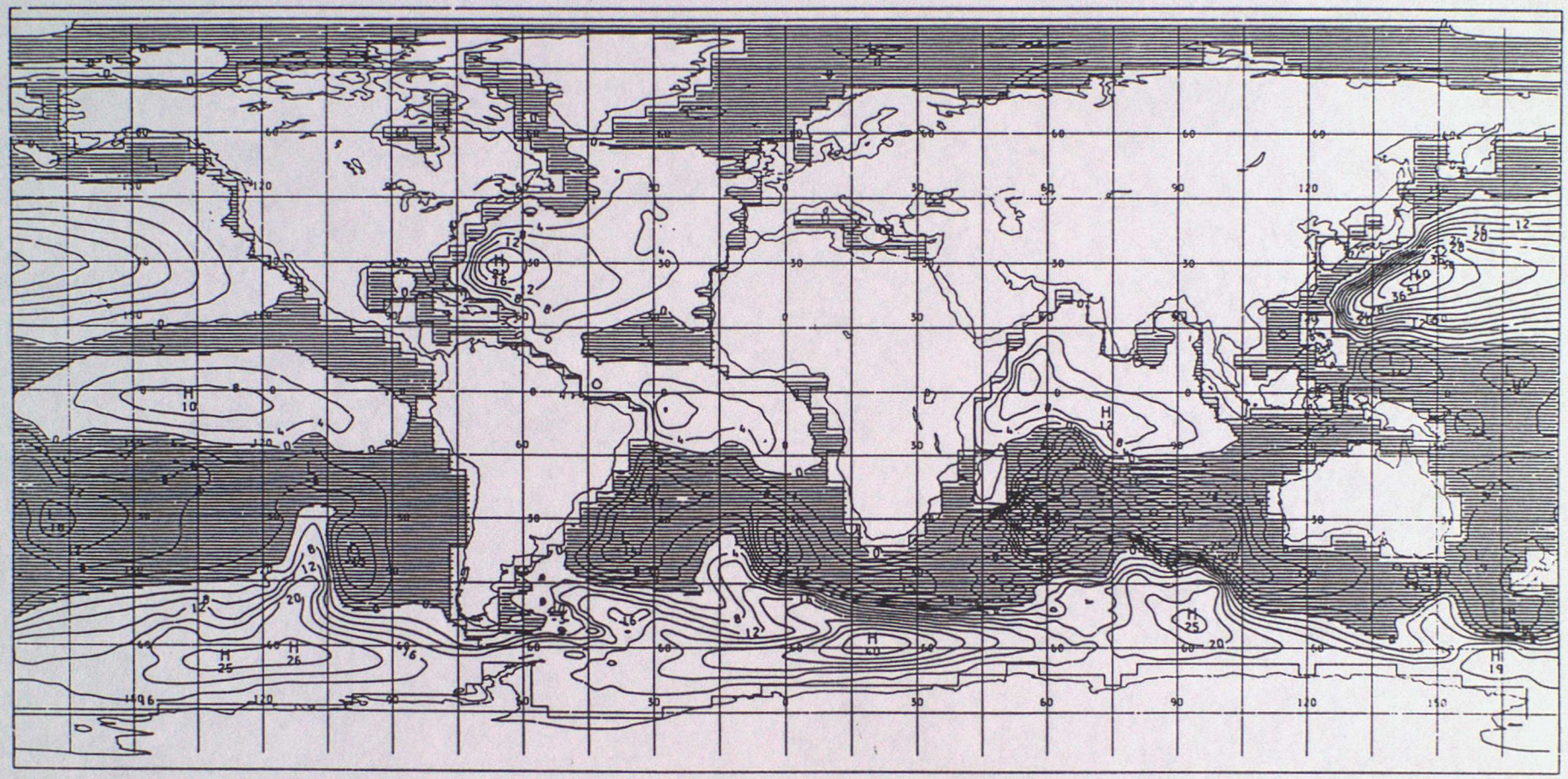

Figure 7.4 Mass transport streamfunction from a barotropic integration of the Bryan/Semtner ocean model on a 2.5° x 3.75° grid forced by the annual mean wind stress. Units are Sverdrups (see text)

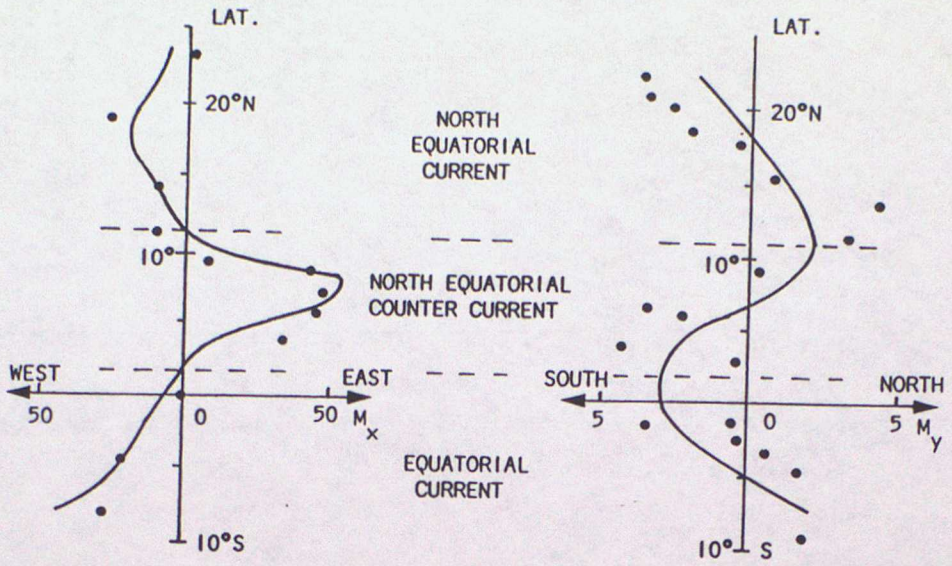

Figure 7.5 Mass transport components in the eastern Pacific calculated from the mean wind stress (lines) compared to those from geostrophic calculations from oceanographic data (dots). M_x and M_y in tonnes per second through a vertical area 1 m wide and 1,000 m deep (approximately equivalent to 0.1 Sv per degree latitude). (From R.O. Reid, *J. Mar. Res.*, 7, 90 & 91, 1948.)

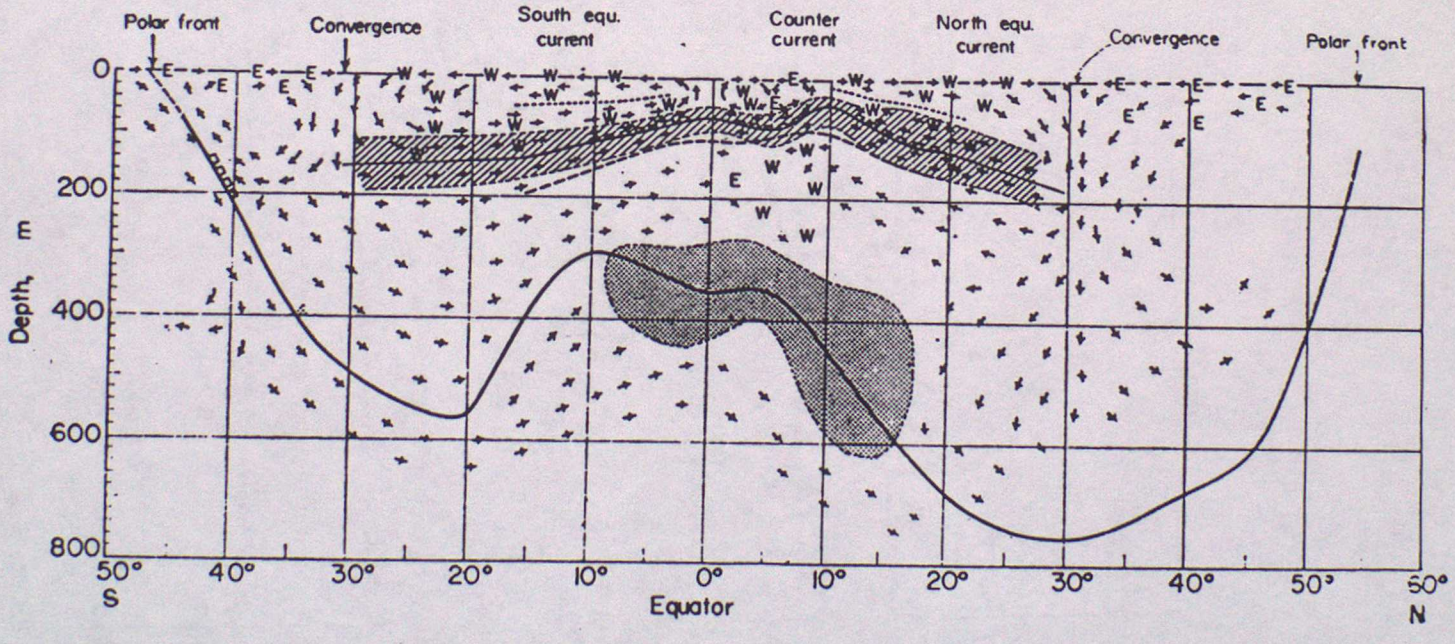

Schematic picture of structure and circulation in the troposphere of the Atlantic Ocean in the meridional direction. (Reproduced from Physical Oceanography, *Vol. 1, by A. Defant, p. 600, figure 274, with permission of Pergamon Press.)*

Boundary between the warm upper ocean and the cold polar ocean.
Tropical–subtropical thermocline
Layers of extremely low oxygen contents ($< 1 \cdot 5$ cm^3 l^{-1}).
Position of tropical–subtropical salinity maxima.
W, E *Zonal velocity component (W toward west, E toward east)*

Figure 7.6

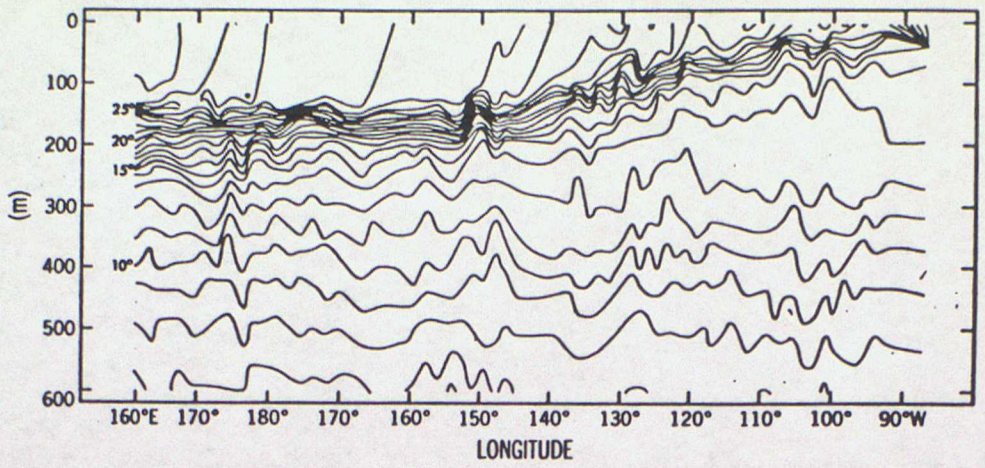

Temperature as a function of longitude and depth along the equator in the Pacific Ocean as measured by Colin *et al.* (1971).

Figure 7.7

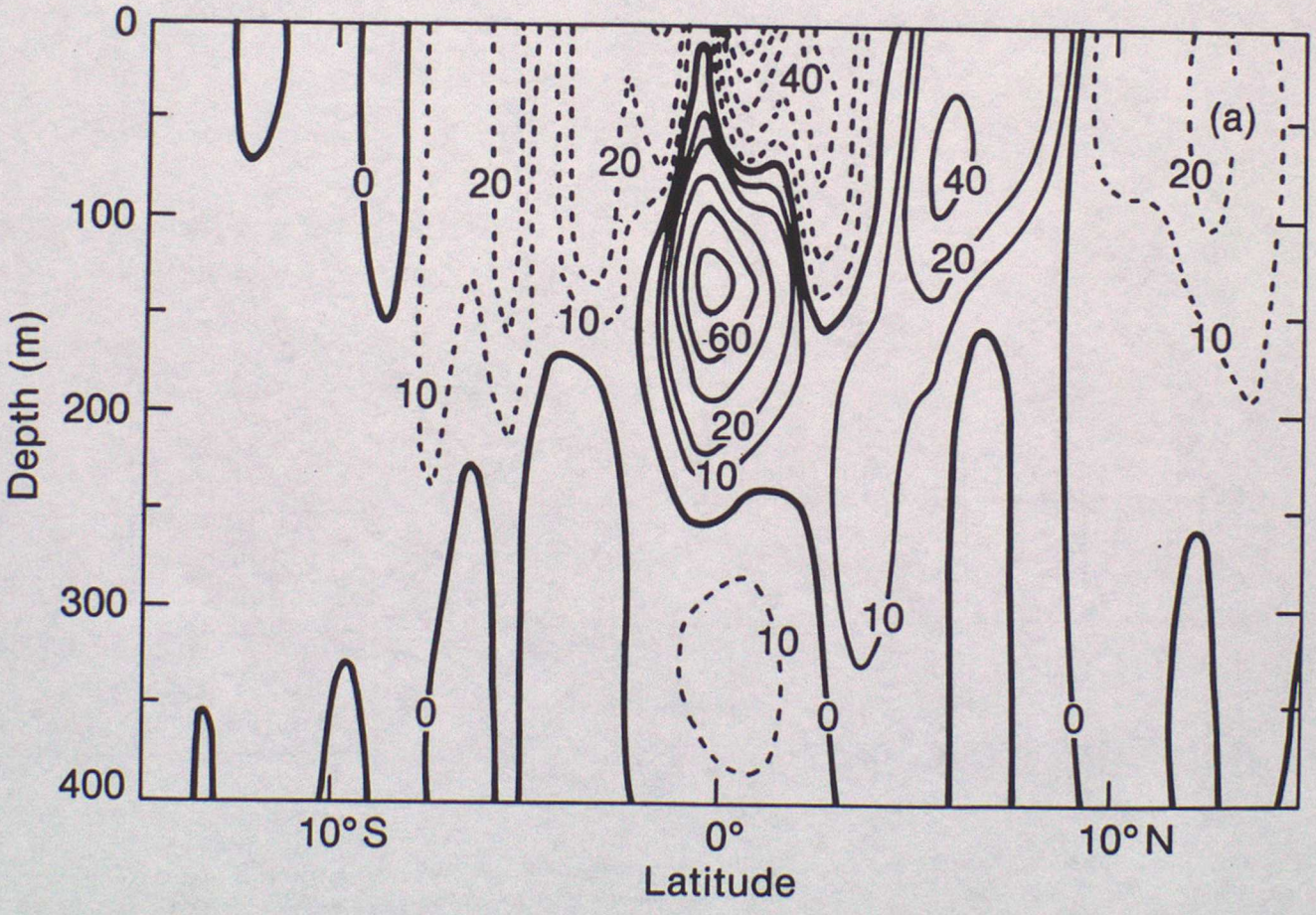

Figure 7.8 Annual mean latitude-depth cross section of the observed E-W current component (solid lines) and the W-E component (dashed lines) at 155° W.

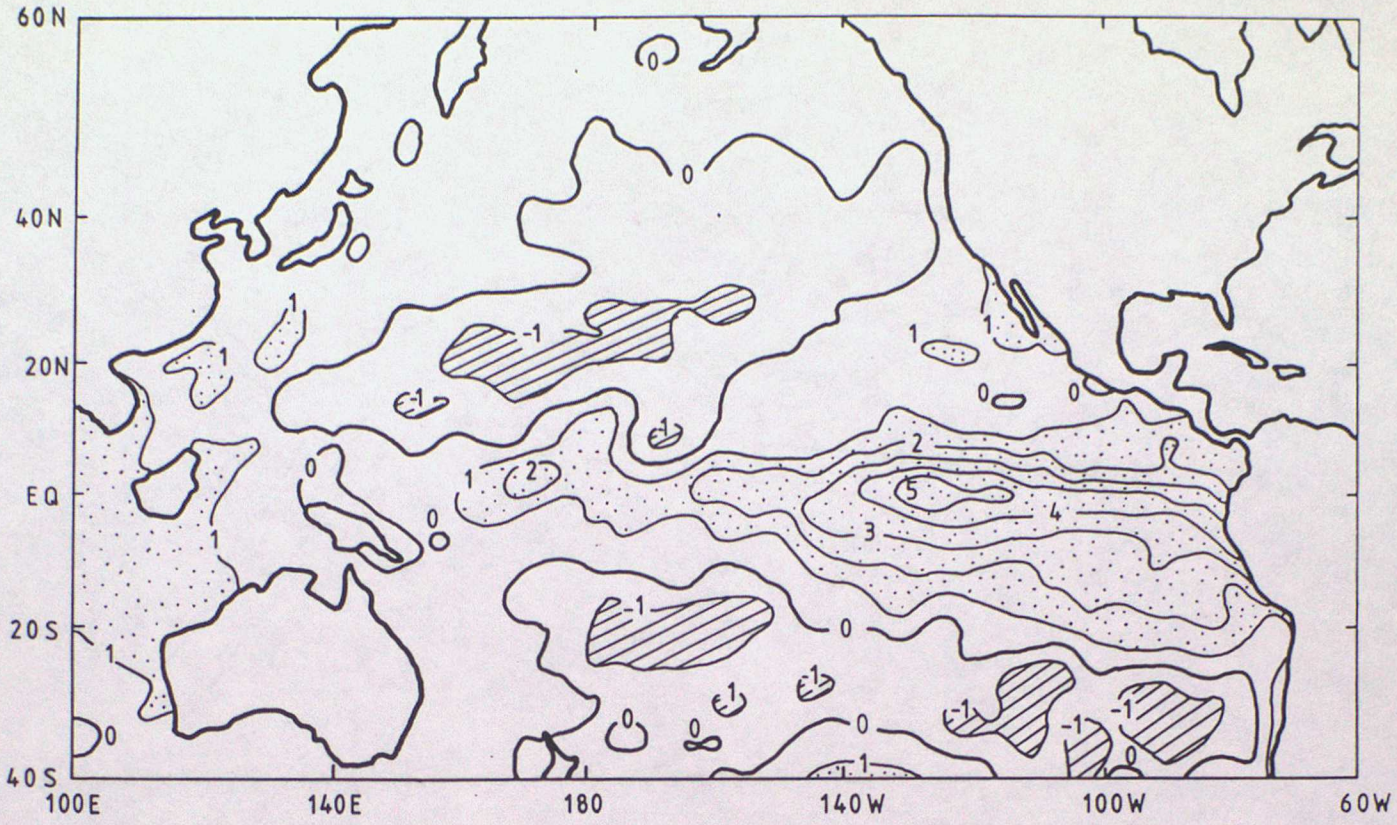

Sea surface temperature anomalies (°C) in the tropical Pacific Ocean during an El Niño event (December, 1982).

Figure 7.9

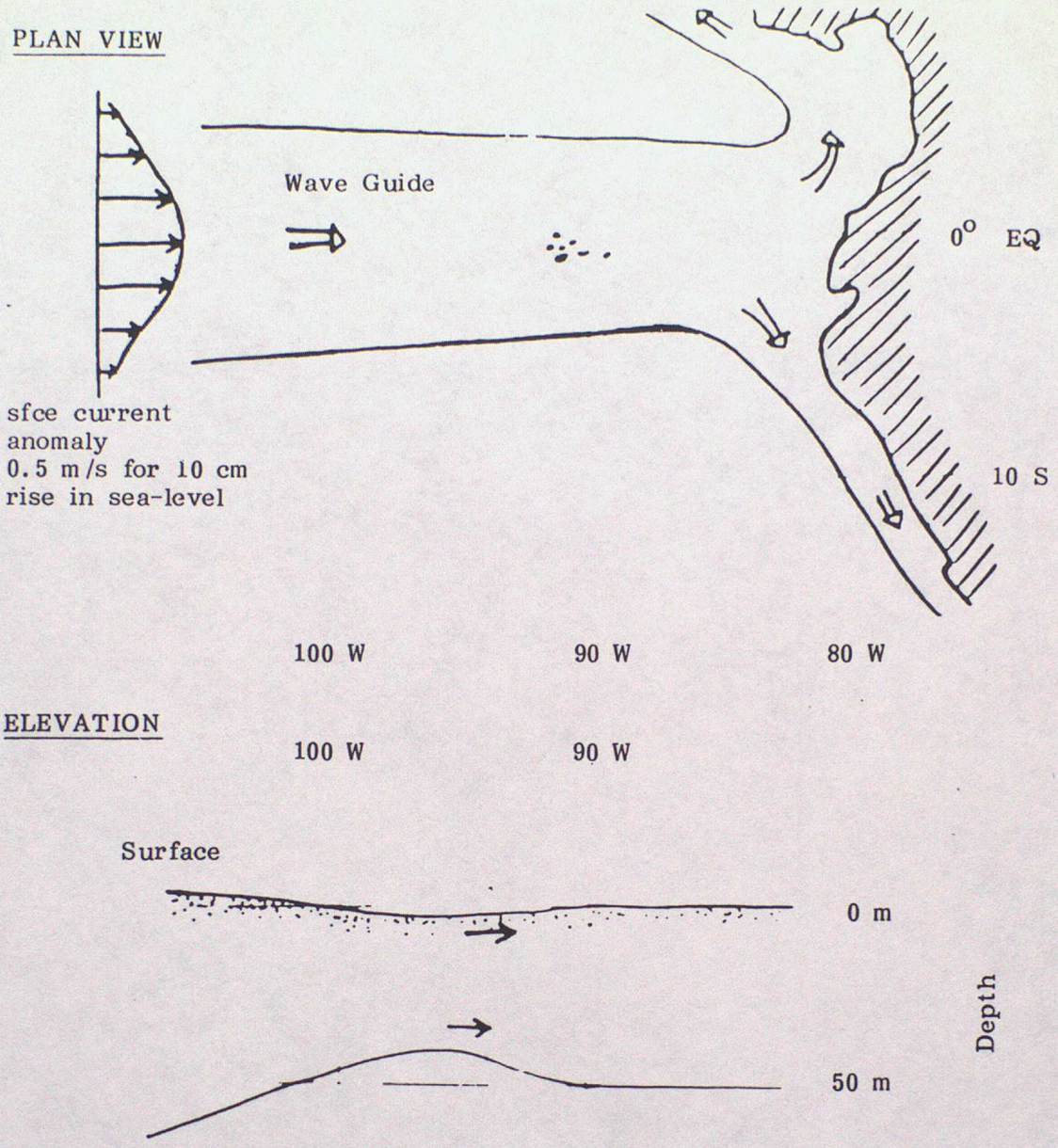

Figure 7, 10 Structure of an equatorial Kelvin wave which propagates eastwards along the equator

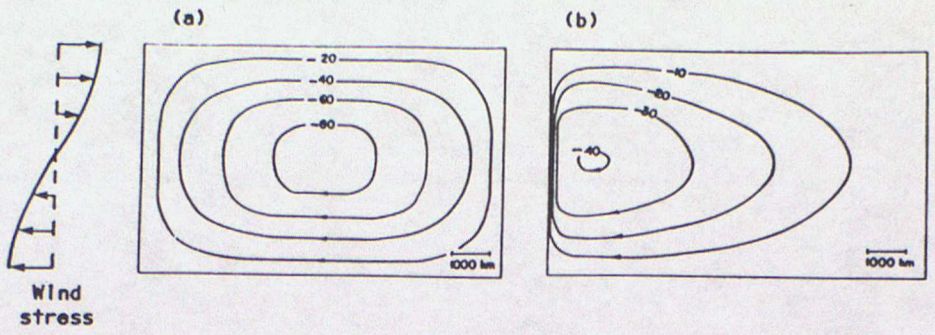

Figure 7.11 Flow patterns (streamlines) for simplified wind-driven circulation with: (a) Coriolis force zero or constant, (b) Coriolis force increasing linearly with latitude (from Stommel, *Trans. A.G.U.*, 29, 205, 1948).

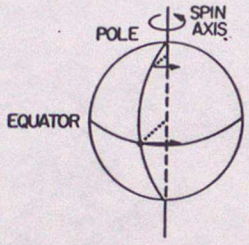

Intrinsic CCS (Counter ClockWise) angular momentum of fluid on earth's surface is zero at poles, maximum at equator: distance r from spin axis increases, equatorward.

Angular momentum

Poleward-moving water conserves total angular momentum by spinning CW to offset CCW tendency caused by decreasing distance from spin axis.

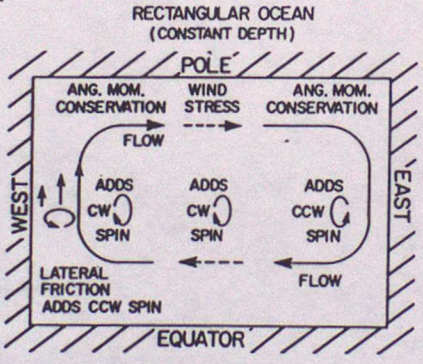

Angular momentum

Equatorward-moving water conserves total angular momentum by spinning CCW to offset CW tendency caused by increasing distance from spin axis.

Spins do not balance. Flow speeds up until lateral friction with boundary provides balancing CCW spin.

Spins balance, flow in equilibrium.

Figure 7.12 **Westward Intensification.** Schematic of the flow in a rectangular, flat-bottomed "ocean" on a rotating earth, induced by a wind stress pattern (dotted line) which is eastwards near the pole and westwards near the equator. To conserve total spin (vorticity) in the gyral flow, the polewards-moving water on the western side of the "ocean" must speed up until its CW spin is balanced by lateral friction with the boundary. The result is a circulation which is "Westward intensified". The Gulf Stream and the Kuroshio are examples of the effect.

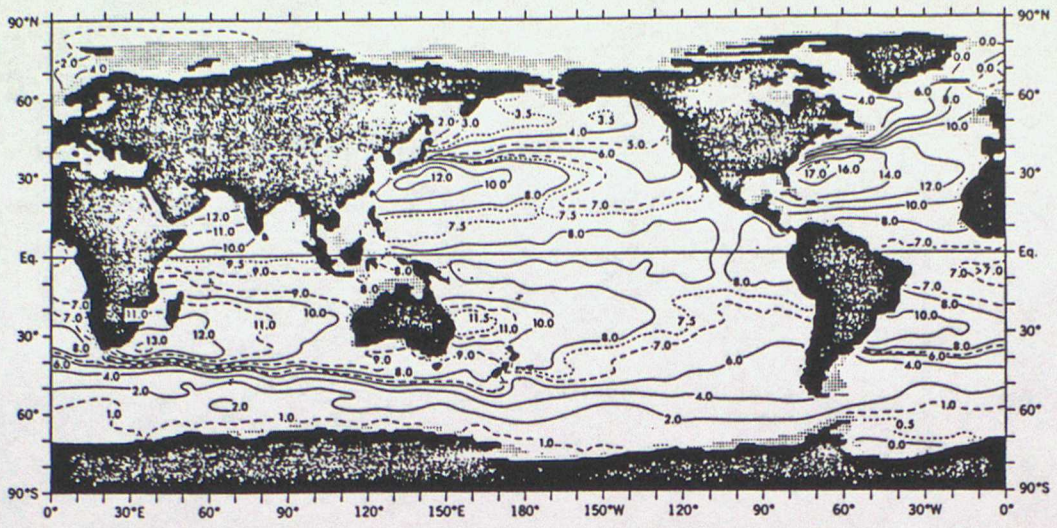

Annual mean potential temperature (°C) at 500 m depth.

Figure 7.13

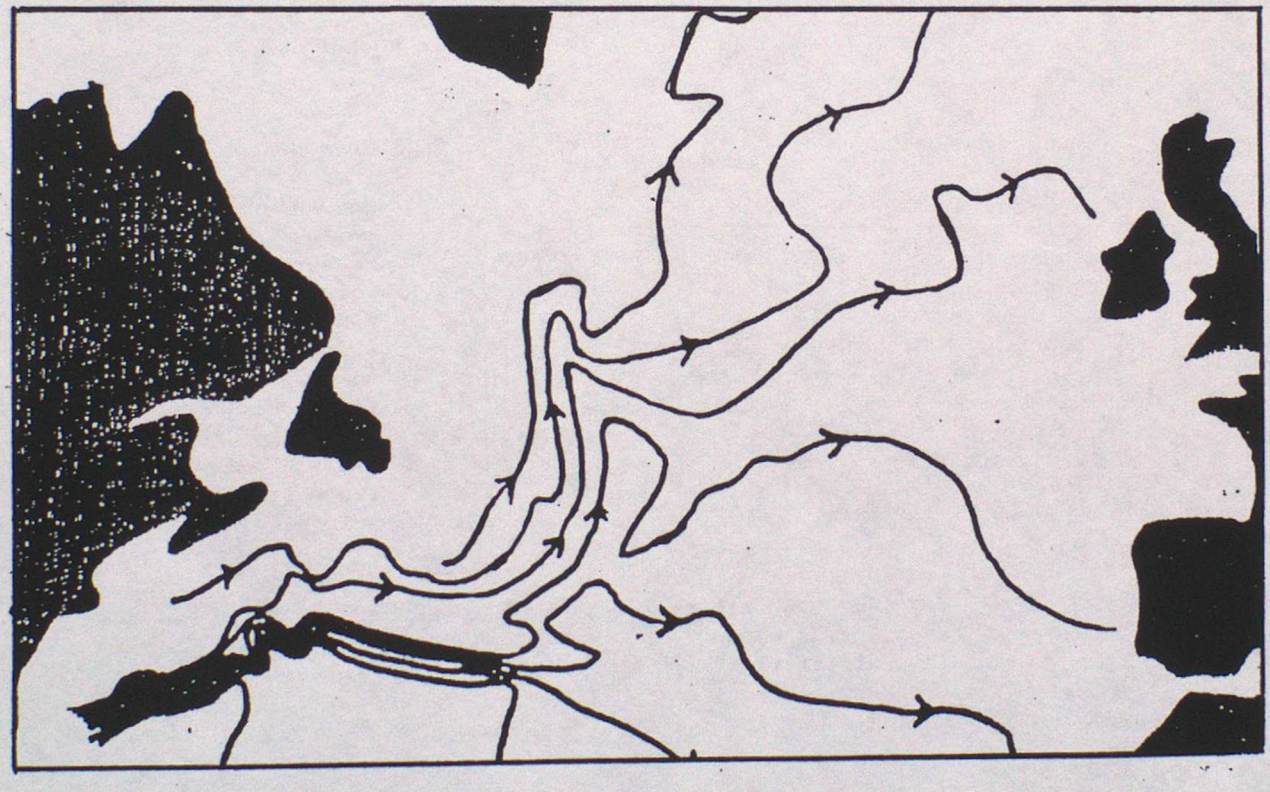

Figure 7.14 Dynamic topography of the 100 decibar surface relative to 700 decibar (after Stommel, Niiler and Anati 1978). The currents at the 100m level, relative to those at 700m flow along the isolines in the direction shown and are approximately in inverse proportion with the contour spacing.

(a)

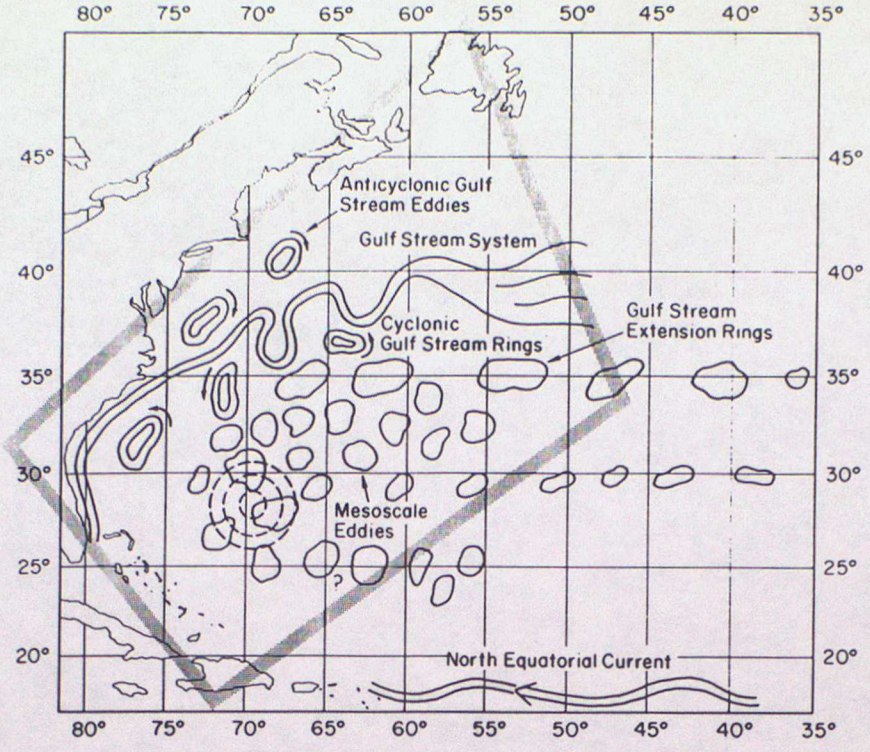

Schematic of a typical instantaneous surface flow pattern in the North Atlantic. The corresponding typical variation of the zonal averaged wind stress with latitude would indicate, for instance, a general westerly direction of winds in mid-latitudes and a general easterly direction of winds in the tropics and high latitudes. [From Semtner and Mintz (1977).]

(b)

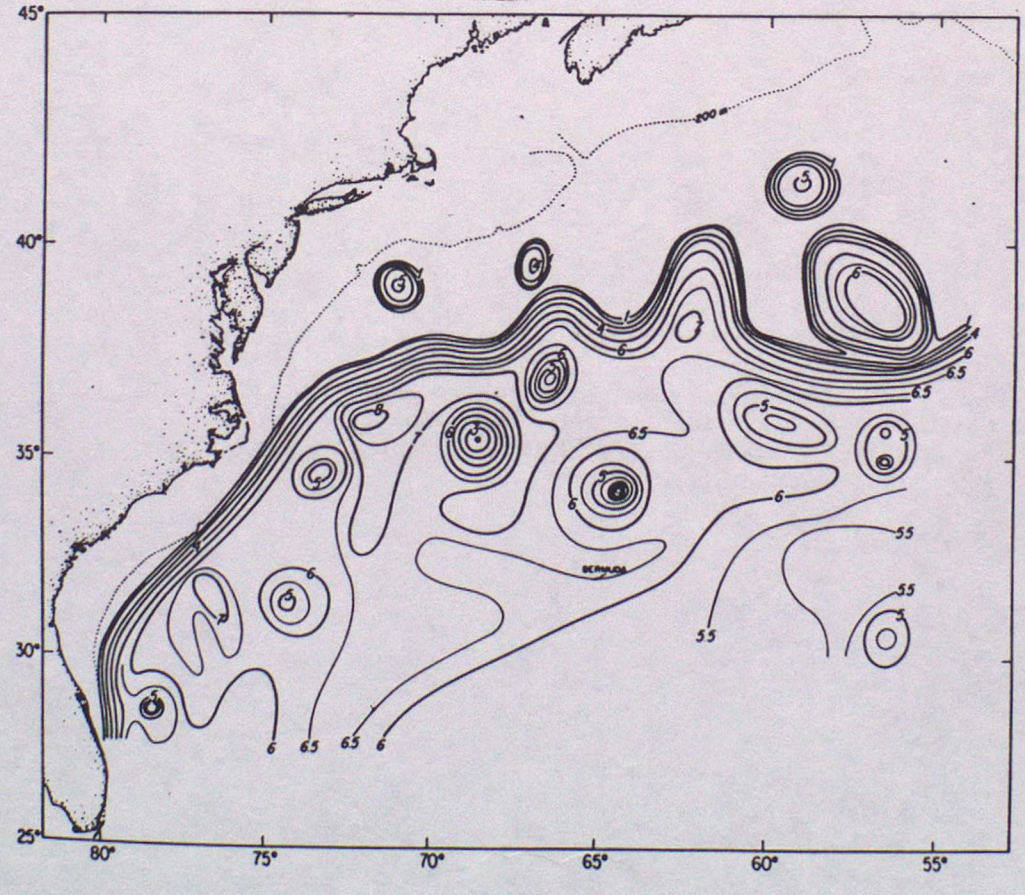

Chart of the topography (hectometres) of the 15° isothermal surface showing the Gulf Stream, nine cold-core and three warm-core rings. Contours are based on XBT, CTD, hydrographic and satellite infrared data from the period March 16 to July 9, 1975. (Richardson et al., 1978).

Figure 7.15

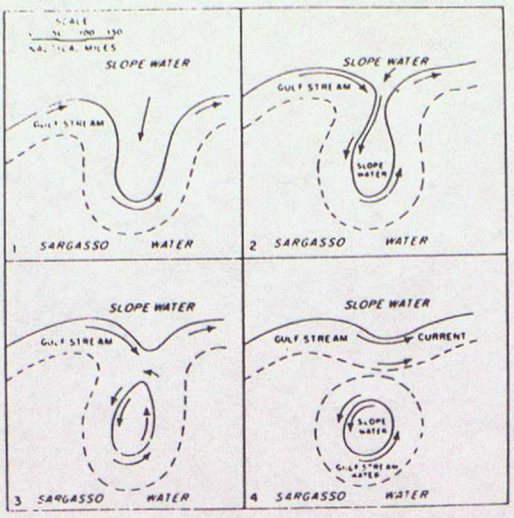

a. Schematic of the birth of a cold core ring from the Gulf Stream. (After Parker, 1971.)

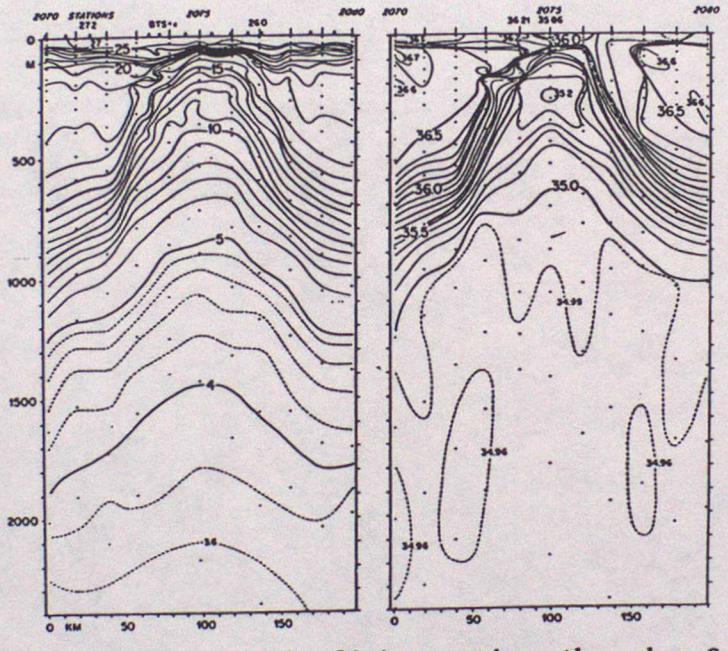

b. Temperature and salinity sections through a Gulf Stream "cold core" ring, or eddy. Location is 36.5°N, 64°W, on 31 July 1967; data from R.V. "Crawford" cruise 158. (After Fuglister, in Angel, 1977.)

Figure 7.16

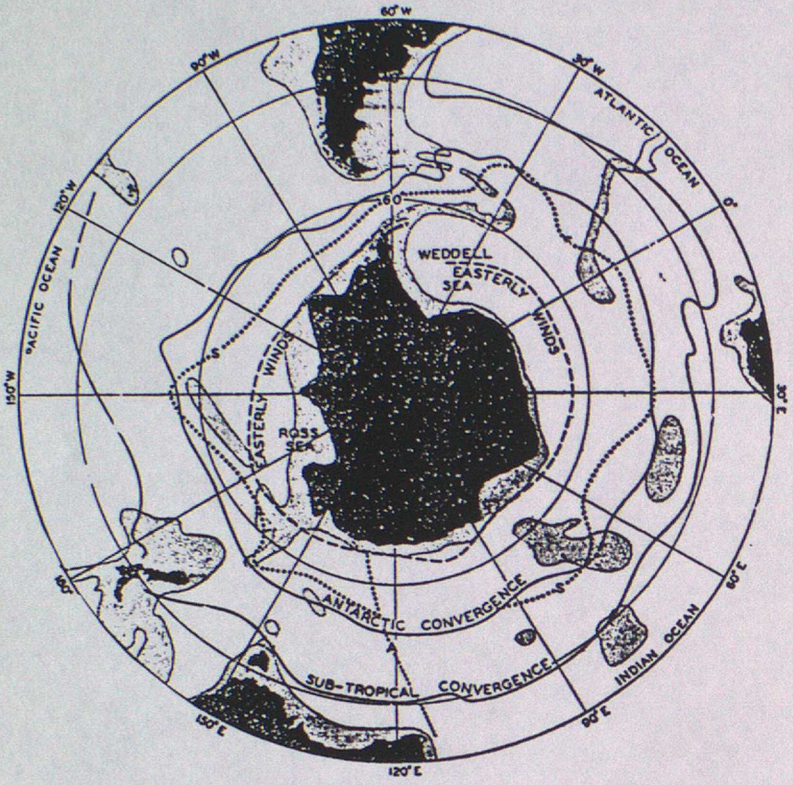

a. Map of Antarctica, showing (solid lines) the position of the Sub-tropical and (winter) Antarctic Convergence Zones, and (dotted line) the summer Antarctic Convergence zone. the dashed line shows the outer limits of the Antarctic easterlies. The roughly meridional dotted line marked "A" is the position of the line of stations from which Figure 11b is derived.

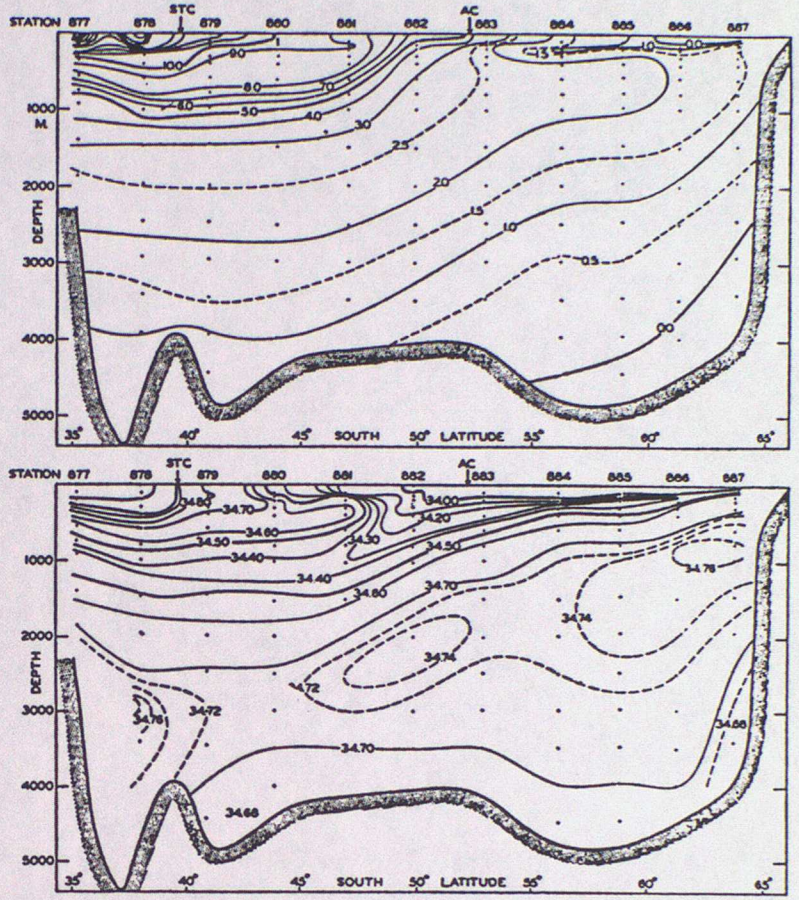

b. Temperature (top) and salinity (bottom) sections from Australia (on the left) to Antarctica (section marked "A" on Figure 11a). Positions of Sub-tropical and Antarctic Convergences marked "STC" and "AC". (After Sverdrup, Johnson and Fleming, 1942.)

Figure 7.17

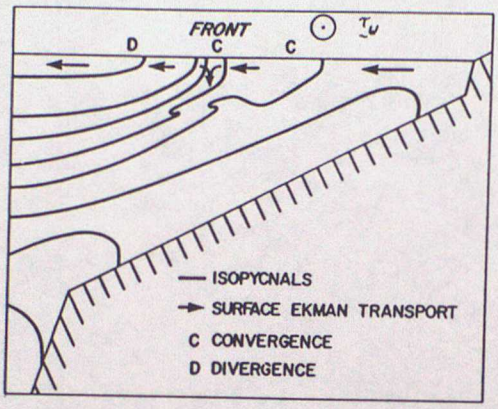

Figure 7.18 Diagram of an "upwelling front" in the Northern Hemisphere. A wind stress τ_w, out of the paper, drives surface water offshore ("surface Ekman transport" arrows). The dynamics by which the front is maintained between the inshore upwelled deep water and the offshore surface water causes convergence and sinking at the front ("C") and divergence offshore ("D"). (After Bowman and Esaias, 1978.)

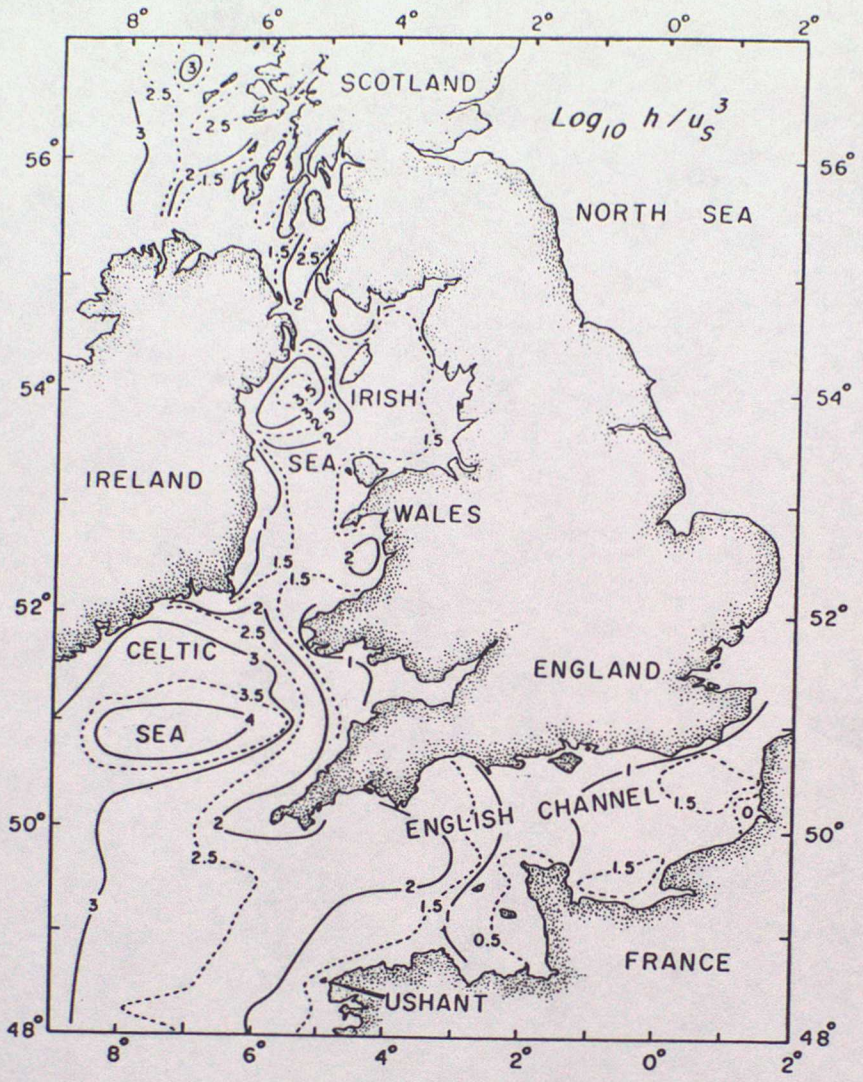

Figure 7.19 Plot of the $\log_{10}$ of the tidal mixing parameter h/u_s^3, where h is the water depth and u_s is the surface tidal speed of the water, for the seas of southwest England and Ireland. Tidal mixing fronts are found between regions of little mixing (Celtic Sea, western Irish Sea) and strong mixing the coast of South Wales, eastern Irish Sea), and in the vicinity of major headlands (Land's End and Ouessant or "Ushant"). (After Bowman and Esaias, 1978.)

PHYSICS AND DYNAMICS OF THE CLIMATE SYSTEM

LONG TIME-SCALE PARTS OF THE CLIMATE SYSTEM

H Cattle

Met O 20, Meteorological Office, Bracknell

8.1 INTRODUCTION

The climate system shows variability on a wide range of timescales. Figure 8.1 shows a reconstruction of the Earth's surface temperature during the past 1 million years, based on a variety of proxy data. The record of temperature shown the figure shows that variations in the recent past are about one order of magnitude less than those associated with the glacial and interglacial cycles. A detailed description of the characteristics of the climate revealed by Figure 8.1 will be given in **Climates of the World**. We shall be concerned here with some of the aspects of the physics and dynamics of the climate system which may be important for long term climate change. The large variation in amplitude and time scales of the climatic record depicted suggests that it is highly unlikely that one mechanism is responsible for all climate fluctuations. An idea of the variety of processes which may be bought into play may be obtained from Figure 8.2. These potential processes can be broadly grouped into 'external' and 'internal' mechanisms. The main external mechanisms include changes in the energy output from the sun and variations in the earth's orbital parameters (the Milankovitch hypothesis - see **Climates of the World**, Lecture 7). The internal mechanisms can be sub-divided into three groups. First there are the processes which involve the Earth's lithosphere such as continental drift, mountain building and volcanic activity. Second there are the internal oscillations between atmoshere, ocean, cryosphere, biomass and land surface. A shorter time scale phenomenon, the ENSO phenomenon has already been shown (Lecture 7) to involve an internal interaction between the atmosphere and ocean. Thirdly there are the possible effects of man's activities - addition of carbon dioxide to the atmosphere by burning of fossil fuels, addition of other radiatively active gases (e.g. CFCs) and aerosols to the atmosphere, and changes brought about by changes in land use, particularly deforestation. In this lecture, we shall consider in

particular some aspects of the influence of the deep ocean circulation and of the cryosphere. Note, from Figure 8.2 that we are dealing here with systems with widely varying response times. The effect of the longer time scale components of the climatic system on the atmospheric response characteristics is illustrated schematically in Figure 8.3 (Hasselmann, 1979). The response curves correspond to an idealised 3 layer box model consisting of the atmosphere (a), a mixed ocean layer (m) and the deep ocean (d). Each layer is assumed to be characterised by a single temperature T_a, T_m and T_d. The heat balance of the layers is assumed to be governed by the external input q, the radiative heat loss, $-\alpha T_a$, of the atmospheric layer and a simple Newtonian heat exchange between the layers, according to the equations shown in the figure. The heat capacities of the three layers satisfy the inequalities $c_a << c_m << c_d$.

The response of the system to a step change in q then consists of three regimes in which first the atmosphere, then the atmosphere and mixed layer, and finally all three layers attain a state of approximate equilibrium between the ingoing and outgoing heat fluxes. Though we shall not address the question further here, this evidently presents a problem in modelling in terms of establishing the equilibrium state of the coupled system.

8.2 THE DEEP OCEAN CIRCULATION

8.2.1 Characteristics of deep water formation and circulation

The deep ocean is, as yet, much less well described dynamically than the upper layer circulation. From water property distributions it is evident that, in terms of the present day climate, the main source of deep water and its circulation is deep oceanic convection off Greenland in the North Atlantic, in the Norwegian Sea and in the Weddell Sea (Figure 6.17(c)). Deep convection also occurs in the Mediterranean, playing a part in the production of saline Mediterranean water, important for the circulation of the North Atlantic following its injection into the Atlantic basin via the sub surface flow through the Straits of Gibraltar. Figure 8.4 shows (on the 3 C potential temperature surface) the resultant tongue of highly saline water which is a permanent feature of the North Atlantic salinity structure. Figure 8.5(a) shows a schematic diagram of the water masses of the Atlantic Ocean and Figure 8.5(b) (from Gordon (1971) illustrates possible flow rates.

Deep convection is associated with thermohaline processes, being due to increase of density of the upper ocean consequent on decrease of temperature due to surface heat loss and/or increase of salinity due to freezing out of ice. The sinking motions associated with deep convection have been observed to occur over small (< 10 km diameter) regions of the ocean surface. Lateral mixing with the surrounding water produces large amounts of water with closely defined temperature and salinity characteristics, which then spreads out from polar regions along the bottom of the world's oceans. An indication of this is shown in Figure 8.4 which, in addition to the saline Mediterranean water, also shows a low salinity tongue corresponding to the fresher water moving down the northwestern boundary from the overflow regions to the north.

For a long time, the deep ocean circulation was envisaged as a very slow flow (mm day^{-1}) of the entire mass. However, Wüst (1955) showed for the Atlantic, both from data on dissolved oxygen and from geostrophic calculations, that a considerable volume transport occurs in a relatively narrow bands on the west side of the ocean , flowing to the south in the North Atlantic deep water and to the north in the Antarctic bottom water. An example of such a flow is shown in Figure 8.6. The first realistic model of the deep ocean circulation was proposed by Stommel (1958) and Stommel and Aarons (1960). In company with the concept of the presence of intense deep western boundary currents they made the assumption that the mean horizontal deep flow in the open ocean is geostrophic. They also used the idea that, in compensation for the known sinking of near-surface water in small regions, there is a general slow upward movement of deep water over most of the rest of the ocean which balances the downward diffusion of heat from the upper layer and which thus accounts for the existence of the main thermocline.

In Stommel and Arons' model (illustrated in Figure 8.7) the three oceans were represented as flat bottomed basins bounded by either parallels or meridians and connected to the south by an analogue of the Antarctic circumpolar current. The flow was taken to be barotropic, driven by sources in the model counterparts of the Weddell Sea and northern North Atlantic (representing sinking from the surface layer), and by compensatory upwelling, distributed uniformly over remainder of the world ocean. The interior flows were considered everywhere poleward and eastward, fed by the intense currents along the western boundaries. In the Atlantic, the boundary current emanating from the northern source flows to the southern

limit of the South Atlantic. There it, the interior flow and the Weddell Sea source increase the transport of the deep Circumpolar current which, in turn, is the source for the northward-flowing western boundary currents in the Indian and Pacific Oceans, entering at their southwestern corners.

Note that this model was not intended as a realistic description of the deep ocean circulation. By treating the ocean floor as level, it gave single circulation systems in the northern and southern hemispheres of each ocean, whereas the mid-ocean ridges divide the oceans into separate basins with multiple circulation systems and multiple entrance points for deep water from the Antarctic. Also, because it is barotropic, it cannot allow layered deep flow, with opposed boundary currents one above the other, as occurs most spectacularly in the South Atlantic where Antarctic bottom water flows northward beneath the southward current of North Atlantic deep water (Figure 8.8). Nevertheless, when the oceans have been reconnoitered with an appropriate observational strategy, deep western boundary currents have been found where anticipated, both close to the continents and in association with the mid-oceanic ridges. However, as yet, these deep density driven flows are not understood quantitatively. Only rarely has their strength been measured well; typical speeds are modest when compared to with surface western boundary currents. They are generally less than 10 cm s^{-1} over a width of order 100 to 200 km.

8.2.2 Tracer studies

Evidence for water mass formation, mixing and circulation comes to a large extent from studies of tracers in the ocean. Temperature and salinity are prime examples, but extensive use has also been made of other tracers, both naturally occurring (such as dissolved oxygen and carbon-14 (^{14}C)) and man made.

Much work has been done under the Geochemical Ocean Sections Study (GEOSECS) initiated in the early 1970s. Dissolved oxygen has been measured in the ocean, in conjunction with temperature and salinity, since the 1930s and much information on its global distribution is available. Oxygen is absorbed most efficiently at low temperatures and thus the largest concentrations are found in Arctic and Antarctic waters. It is a good tracer for studying the mixing of water masses, such as the North Atlantic deep water and Antarctic bottom water, but it has to be monitored continuously because it is consumed by bacteria and animals, even in the deep ocean. Note, in Figure 8.8(c) the relatively high oxygen contents of

the northward flowing Antarctic Bottom Water and southward flowing North Atlantic Deep Water above. Figure 8.6(d) shows the corresponding silica concentration. Silica is produced from siliceous bottom sediments such as red clays, which are plentiful in the Pacific Ocean and also occur, though to a lesser extent, in the Indian and Atlantic Oceans. Silica is consumed by biological processes in the upper layers of the ocean and is thus most useful for studying bottom and intermediate water circulations. In the North Atlantic Deep Water, the silica concentrations are low compared with those in the Antarctic Bottom Waters (c.f Figure 8.8(d)) and this tracer is therefore ideal for sudying mixing between the two water masses. North Atlantic deep water is composed of a number of different water types and so its temperature-salinity characteristics vary accordingly. However, the silica concentration is remarkably uniform, which makes it a very consistent tracer.

It should be noted that use of such 'passive' tracers is only qualitative, because of lack of knowledge about rates of production and consumption. Quantitative information on the age and circulation time scale of any given water mass can be obtained using radioactive tracers. Some, such as ^{39}Ar are produced naturally from cosmic rays. Some, such as ^{90}Sr and ^{137}Cs are by-products of nuclear tests. Others, such as ^{3}H (tritium) and ^{14}C are by products of both nuclear tests and cosmic rays. Typically, ^{14}C measurements give a mean ventilation time of 1400 (± 250) years for deep water circulation, though recent evidence suggests that this is an over-estimate because it is not possible to distinguish old water masses which have been recirculated round the ocean a number of times from newly formed water masses. Measurements on North Atlantic Deep Water have indicated an apparent age of between 80 and 225 years. Evidence for such rapid ventilation is shown in Figure 8.9, which shows the relatively high concentrations of tritium in the North Atlantic Deep Water only 20 years after its surface input following nuclear tests. The largest concentrations of both tritium and ^{14}C are located in the Pacific and Atlantic Oceans at about 50° N. The concentrations decrease towards the southern hemisphere but the concentration gradient is not uniform. Near 15° N there is a remarkable reduction in the concentration of both tracers which is associated with a frontal boundary between the sub-tropical gyre to the north and the equatorial waters to the south. The low concentrations and limited vertical penetration between 15° N and S suggest that water is being upwelled from depths of at least 500 m. Broecker (1978) has suggested that this equatorial upwelling flux of 45 x 10^{6} m^{3} s^{-1}

(45 Sverdrups) is comparable with the total production of bottom water in the global ocean.

8.2.3 Deep water formation and climate change

There has recently been increasing interest in the question of whether the ocean-atmosphere system has more than one stable mode of operation, in which the role of deep water formation plays a part. By way of illustration of the possible interaction of the deep waters of the ocean with changes in the atmospheric climate, we shall here consider some of the arguments for this suggested in a review article by Broecker, Peteet and Rind (1985).

Overall, the meridional overturning in the North Atlantic due to production of deep water is estimated to amount to some 20 x 10^{6} m^{3} s^{-1} or 20 Sverdrups (Broecker, 1979). The water feeding the source region for the deep water has a temperature of order 10 C, whereas the water leaving the region has a temperature of order 2 C. Thus, as a by product of the deep water formation, around 2 x 10^{22} J of heat are released to the atmosphere each year, an amount corresponding to about 30% of the solar heat reaching the surface of the Atlantic Ocean in the region north of 35° N. This large heat loss from the ocean surface is such as to actually demand a reversal in direction of the intuitively expected equator to pole heat flux in the South Atlantic (Lecture 6, Figures 6.18 and 6.21). In contrast to the North Atlantic, there is a marked absence of deep water production in the Northern Pacific, which is considered to be primarily rooted in the large salinity difference between the two basins. The upper layer waters of the North Atlantic are saltier than in the global mean, whereas those of the North Pacific are fresher (Figure 6.3). The Atlantic's extra salt allows surface waters of density approaching that as great as any found in the deep sea to be generated during the winter months. By contrast, if cooled to their freezing point, North Pacific waters achieve a density no greater than that of the intermediate depth water of that region.

Although, not necessarily immediately obvious from Figure 6.20, budget studies indicate that, though the Atlantic basin north of 30° N receives a sizeable proportion of the world's river runoff, the surface waters also lose an even greater amount of freshwater through an excess of evaporation over precipitation (Table 8.1). The resulting net loss of fresh water leads to the relatively high salinity of the North Atlantic water. The

relative freshness of the North Pacific waters, on the other hand, is maintained by an overall excess of precipitation over evaporation. A factor in this (Warren, 1983) is that the waters polewards of 30° N are warmer in the Atlantic than in the Pacific, leading to enhanced evaporation over the former basin. To some extent, the warmer waters of the surface waters of the North Atlantic must be related to the deep water formation. Overall, there must be a net near surface polewards flow of warm water in the North Atlantic, to supply that which goes into deep water production, with a return flow southwards at depth. By contrast, in the Pacific, the cold deep flow at depth is polewards. The deep water upwells in the North Pacific, to be carried southward in the upper ocean. In this sense, the system is self sustaining. The deep water circulation pattern maintains the surface temperature of the North Atlantic at a higher value than the Pacific. This temperature difference causes the Atlantic to be enriched with salt, whose excess leads to deep water formation. At steady state, deep water formation must carry away just the amount of excess salt left behind from the atmospheric transport of water from the Atlantic to the Pacific. The standing excess of salt in the Northern Atlantic is presumably just enough to allow the generation of water sufficiently dense to enter the deep Atlantic.

During glacial times, there is evidence from analyses of fossil plankton in deep sea cores that the North Pacific was warmer overall than the North Atlantic. As an example, Figure 8.10 compares present annual mean sea surface temperatures with a reconstruction of the annual mean sea surface temperature field for 18,000 b.p. at the height of the last glaciation. This and other evidence from ice and ocean core data led Broecker et al. (1985) to suggest the possibility of a reversal in the roles of the Pacific and Atlantic in the production of deep water, or at least a reduction in the rate of production (Figure 8.11) during glacial periods, the root causes of the latter being the Milankovitch orbital changes. It may also be that oscillating roles of the two basins in this context explain climate oscillations observed, for example, by Oeschger and his coworkers (1984) in CO_2 data in ice cores and which occur at intervals with climates lying between those characterising glacial and interglacial time.

At first sight, it may seem strange that *decreased* surface temperature in the Atlantic could be associated in a reduction in the rate of production of deep water there. However, remember that a crucial factor is the surface salinity and it is hypothesised that, during glacial times a marked

halocline was present in the sub-polar gyre which would lead to stabilisation of the surface waters (see below). The sub-polar gyre itself may have increased in intensity due to the increased north-south temperature gradient, but with flow such that most of the Gulf Stream water was directed at Southern Europe, with the North Atlantic drift current weaker than it is today.

8.3 SEA ICE AND THE POLAR HALOCLINE

Sea ice covers roughly 7% of the worlds's oceans. It is affected (Figure 8.12 both by dynamical processes (wind stress, water stress, sea surface slope) and thermodynamic processes (in particular the heat flux from the ocean to the ice and the surface heat balance). These affect both the ice motion and the amount of freezing and melting which can take place and which, in turn, determine the thickness and extent of the ice itself. By its presence on the sea surface, the ice substantially increases the albedo of the oceanic regions where it forms, raising it from a value of 0.06 or so to 0.8 or more where the ice is snow covered. It also forms a barrier to direct exchange of sensible heat and moisture between the ocean surface and atmosphere in polar regions and allows much lower surface temperatures to be attained in winter than would otherwise be the case, modifying both the atmospheric boundary layer structure and the outgoing longwave radiative flux.

We have already (in Lecture 6) seen that in the process of freezing, ice exudes salt so that, for example, sea water with a salinity of 34‰ may freeze to give ice with a salinity of only 4‰. This salt passes into the oceanic mixed layer where it enhances convection, leading to mixed layer deepening. During ice melt, relatively fresh water is deposited onto the surface layer of the ocean, often in layers far removed from the original locations of ice growth, again modifying the mixed layer structure. Both of these processes substantially influence the regions of the ocean where deep convection can occur.

The areal extent of floating ice in the southern hemisphere typically varies within the year from a minimum of 4×10^6 km^2 to a maximum of 20×10^6 km^2 (from 2.5% to 13% of the southern hemisphere oceans). The sea ice extent in the northern hemisphere varies far less, ranging from a summer minimum of 8×10^6 to a winter maximum of 15×10^6 km^2, the latter being

roughly 10% of the ocean area in the northern hemisphere. The Arctic Ocean itself, ignoring the peripheral seas, remains covered with ice during most of the year (Figure 8.13(a)). Typically, the ice in the central Arctic is of order 3-4 m thick. In some places it is grounded to the shore horizontally, or to the ocean floor vertically. Such 'fast ice' may extend outward from the coast for a distance of up to 500 km in the region of the Siberian continental shelf. Sea ice moves into the North Atlantic by way of the cold East Greenland and Labrador currents and, to a much lesser extent, into the North Pacific (where it also forms in-situ) through the Bering Strait. Ice also forms in winter in Baffin bay, Davis Strait and Hudson Bay. By contrast, to the Arctic, the Antarctic sea ice distribution is more symmetric, thinner (typical thickness is 0.5-1 m) and less compact. These differences arise as a consequence of at least three major factors: the lower latitudes of Antarctic ice, the non-enclosed nature of the Antarctic ice cover and the divergent nature of the ice cover, which is largely a consequence of the prevailing winds. An additional factor is the generally greater stability of the Arctic waters. Characteristically, (Figure 8.14) the Arctic Ocean has a surface layer of cold and relatively fresh water some tens of metres deep. Beneath it, to a depth of 100-150 m lies the Arctic halocline, in which salinity increases markedly with depth, though temperatures remain close to freezing point like those at the surface. Below the halocline, salinity increases more slowly with depth, and temperatures *rise*. This warmer water is of Atlantic origin. It enters the Arctic basin mainly by the West Spitzbergen current, flowing northward through the Fram Strait between Greenland and Spitzbergen (Coachman and Aagard, 1974) and losing heat at the surface before submerging beneath the cold, but relatively fresh waters of the Arctic surface layer. Thus, though the resulting temperature profile suggests instability, increasing density due to salinity keeps the water column from overturning in all but the shallow surface layer (Figure 8.14(b)). The low salinity surface waters in the Arctic originate mainly from river inflow, though the annual cycle of ice freeze and melt also contributes and leads to a similar, if less marked effect in the Antarctic. Note that if it were not for the presence of the halocline, it would be necessary for the whole of the Arctic ocean to cool to freezing throughout its depth before sea ice formation could take place. This fact has led to speculation that planned diversions of major Soviet rivers flowing into the Arctic basin (to counteract the drying up of the Aral and Caspian seas to the south) might lead to a reduction in the sea ice cover, with impacts on northern hemisphere climate. For a review, see Cattle (1985).

The evidence that sea ice plays a significant role in climatic variations is based on both theoretical and data based studies. On long time scales there is convincing evidence from both model experiments that sea ice plays a major role in contributing to the energy balance of the earth-atmosphere system. On regional and hemispheric scales, atmosphere-sea ice relationships are evident in both data-based and theoretical studies. There is also evidence that ice fluctuations are important locally, primarily through their correlation with air-temperature. Important for long term climate variations are the influence of sea ice processes (ice formation and melt) on the location of bottom water formation and ice-albedo feedbacks. The latter is the dominent factor, for example, in the polar amplification of the temperature rise due to increased CO_2 (Figure 8.15). Increased CO_2 itself leads to atmospheric warming and melting of sea ice, which itself reduces the seasonal range of surface temperature over the areas of reduced ice cover. In addition, the reduction in ice cover decreases the albedo of the surface, leading to increased absorption of solar radiation in summer, further warming and therefore increased ice melt.

8.5 ICE SHEETS AND CLIMATE

Ice sheets are important for climate and the atmospheric circulation because, like snow and sea ice cover, they have a marked effect on the albedo of the earth and the seasonal range of surface temperature, because of their topographic impact on the atmospheric circulation and because changes in their volume could cause large changes in mean sea level. Indeed, during glacial times the volume of water locked up in ice sheets (Figure 8.16 and Table 8.2) was such as to cause exposure of many continental shelf areas (c.f Figure 8.10).

Two large ice sheets are in existence today, covering Greenland and the Antarctic continent (Figure 8.17). With mean topographic surface elevations of over 1500 m and 2000 m and maximum elevations of over 3000 m and 4000 m respectively, both are the highest land masses on earth. The bedrock beneath the Greenland ice sheet is disk shaped, with its central portion well below sea level. The continental plate of Antarctica is more structured. The West Antarctic ice, from opposite South America to about the meridian opposite New Zealand, is underlain by rugged terrain that would form a group of islands if the ice were removed and the West

Antarctic ice sheet itself is grounded in water as deep as 2500 m (Figure 8.18). The East Antarctic ice sheet contains 80% of the ice volume and has little bottom topography, though its deepest point is 500 m below sea level. An important difference between the Greenland and Antarctic ice sheets is that practically no surface melting occurs in Antarctica and the surface accumulation is balanced (or nearly so) by the discharge of icebergs into the sea and by the ablation under the large ice shelves extending out into the ocean. In contrast, the Greenland ice sheet has significant surface melting in its southern portion and an equilibrium line with zero mass balance, like a mountain glacier. Greenland has no major ice shelves; ice not lost by ablation is discharged into the ocean by icebergs calving from glaciers.

Neglecting crustal adjustment, itself an important factor in ice-sheet related climate change on long (palaeoclimatic) time scales, the melting of the Greenland ice sheet would raise mean sea level by 8 m, of the West Antarctic ice sheet by 5-6 m and of the East Antarctic ice sheet by 55 m. For this reason, there has been increasing interest in the possible effects of CO_2 warming on ice sheets and suggestions (e.g by Mercer, 1978) that a climatic warming would trigger a disintegration of the main part of the Antarctic ice sheet. There are, basically, three different ways in which ice sheets react to a climatic warming (Oerlemans, 1985):

(i) a change in the surface mass balance
(ii) larger ice-mass discharge because the ice temperature increases
(iii) grounding-line instability due to thinning of ice shelves.

Mechanism (i) has an immediate effect on sea level and it is certain that an increase of temperature would lead to a decrease in the mass of the Greenland ice sheet. Amach (1980) has estimated a 3% decrease in the Greenland ice volume after 250 yr in the case of a 3 C warming. For the Antarctic ice sheet, the situation is different. Since climatic conditions are much colder, the higher temperatures would lead to higher accumulation rates over the entire ice sheet. Melting may be induced over some very restricted coastal areas, but the total effect on the mass balance would probably be small. A study of the response of the Antarctic ice sheet (Oerlemans, 1982) indicates a 0.5% increase in the ice volume after 100yr. Converting these figures to sea level, it appears that typical changes from this cause are 10 cm per century. Note that natural variability in

accumulation rates may give rise to sea level variations of the order of 5 cm per century (Oerlemans, 1981).

Warming of the ice sheet (mechanism (ii)) is a very slow process and the time scale for the basal layers (which are relevant to the possibility of ice-mass discharge) to feel the effects of temperature changes is typically thousands of years.

Grounding line instability is a more spectacular process relevant in particular to the ice shelves of the West Antarctic ice sheet. The shelves themselves are characteristically 200 to 800 m thick and at several places run aground (Figure 8.19). It is probable that these so-called pinning points exert a strong influence on the stress field of the ice shelf. Upstream of the pinning points, compressive stresses tend to thicken the ice and these thus regulate the mass discharge from it. If for some reason, the ice shelves become thinner, due to increased bottom melt as a result of higher water temperatures for example, the pinning points will disappear. Reduction of the compressive stress will then cause upstrean thinning and a retreat of the grounding line, with possible total collapse of the ice sheet. In this context, there is some geological evidence that at the last glacial maximum (20,000 yr b.p.) the grounded ice in the Ross Sea extended much further out, implying a grounding line retreat of hundreds of kilometers since that time. This retreat was probably initiated by a rising sea level (about 100 m) due to melting of the northern hemisphere ice sheets.

8.6 CONCLUDING REMARKS

In this lecture we have only been able to touch on a few of the mechanisms important for long term climate change. In particular, we have not discussed the influence of the changes in the land surface, though aspects of land surface processes important for shorter term variations (including desertification) were discussed in Lecture 5. On longer timescales, many of the important aspects of land surface processes (vegetation change, snow and ice cover et.) for climate are associated with their influence on the planetary albedo. Thus the increase of albedo with increased snow and ice during the last ice age is generally as a major feedback term with regard to the global radiation balance. Table 3, which gives the decrease in global average July surface albedo from 18,000 b.p. to present as derived in the CLIMAP dataset for land changes between 50° N and S, briefly illustrates this.

Table 8.1 (From Broecker et al., 1985)

Freshwater budget for the North Atlantic Basin, including the Arctic, Mediterranean and Caribbean

Source	Input rate fresh water ($m\ yr^{-1}$)	Freshwater flux (sverdrup)
River runoff[50]	+0.21	+0.33
Precipitation[50]	+0.87	+1.36
Evaporation[50]	−1.21	−1.89
Mediterranean exchange*	−0.07	−0.10
Net†	−0.20	−0.30

The combined area of the North Atlantic basin (0°–80° N) excluding the Mediterranean Sea is $4.9 \times 10^{13}\ m^2$. For freshwater flux, 1 sverdrup represents a flow of a million cubic metres per second.

* The exchange between the more salty waters of the Mediterranean Sea and the less salty waters of the open Atlantic leads to a loss of fresh water from the Atlantic. This process is driven by the high evaporation rate (relative to precipitation and runoff) for the Mediterranean Sea.

† Using a deep water production rate in the northern Atlantic of $20 \times 10^6\ m^3\ s^{-1}$ and a salinity excess for this water of 0.50‰, a fresh water flux of 0.3 sverdrups would be obtained, indicating that no large discrepancy exists between oceanographic and meteorological budgets.

Table 8.2 (From Oerlemans, 1985)

	present	ice age	res. time
oceans	1 370 000	1 330 000	3000
land ice	24 000	64 000	15 000
groundwater	64 000	?	10 000
lakes	230	?	10
soil	80	?	0.5
atmosphere	13	11	0.02

Some data on the water budget of the earth, from Ref. 4 with some additions. Volumes are in $10^{12}\ m^3$, residence times in years. Residence time for land ice refers to ice sheets, glaciers have a much shorter turnover time (centuries).

Table 8.3 (From Dickinson and Hanson, 1984)

Decrease of global average July surface albedo from 18000 BP to present for land changes between 50°N and 50°S

Changed surface	$\Delta\alpha_g$ (%)
Water	0.29
Vegetation	0.45
Permanent ice	0.73
July total	1.46

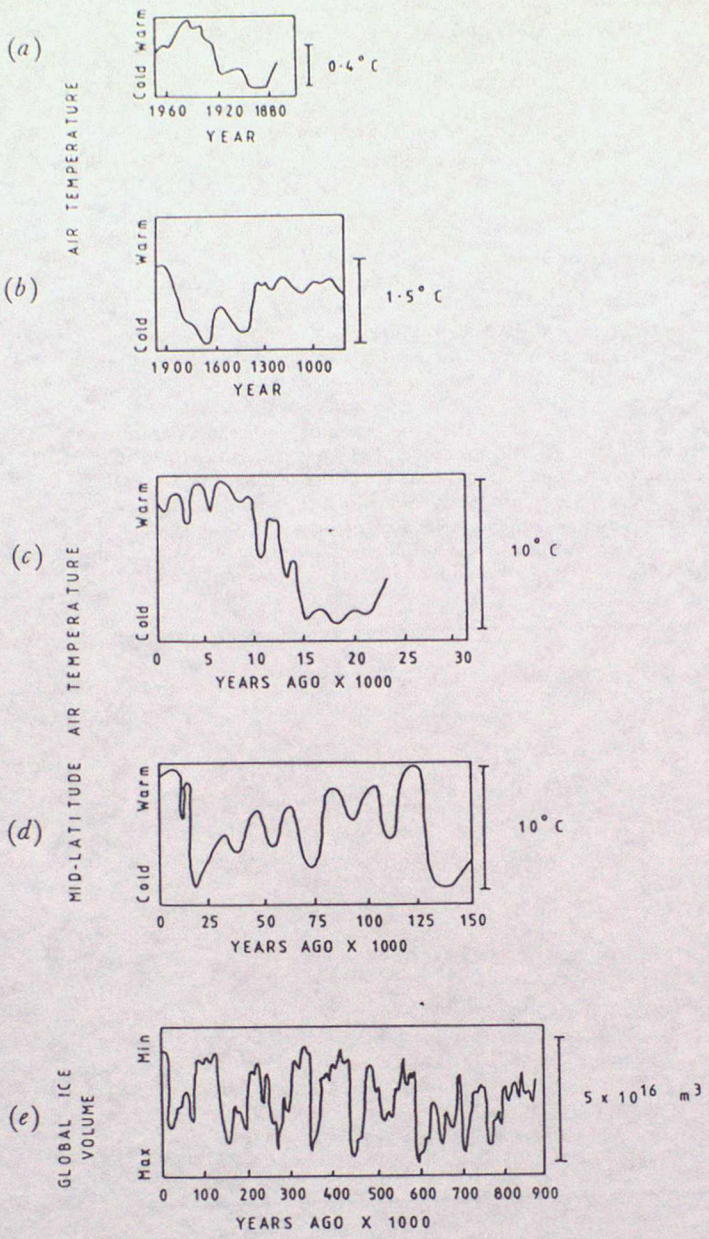

General trends in global climate; the past million years. (a) Changes in the 5 year average surface temperatures over the region 0–80°N. (b) Winter severity index for eastern Europe. (c) Generalized Northern Hemisphere air temperature trends, based on fluctuations in alpine glaciers, changes in tree lines, marginal fluctuations in continental glaciers and shifts in vegetation patterns recorded in pollen spectra. (d) Generalized Northern Hemisphere air temperature trends based on mid-latitude sea surface temperature, pollen records and world-wide sea level records. (e) Fluctuations in global ice volume recorded as changes in isotopic composition of fossil plankton in a deep-sea core. (Reproduced from The Physical Basis of Climate and Climate Modelling, *WMO Garp Series, No. 16, p. 8, figure 2.5, with permission of WMO.)*

Figure 8.1

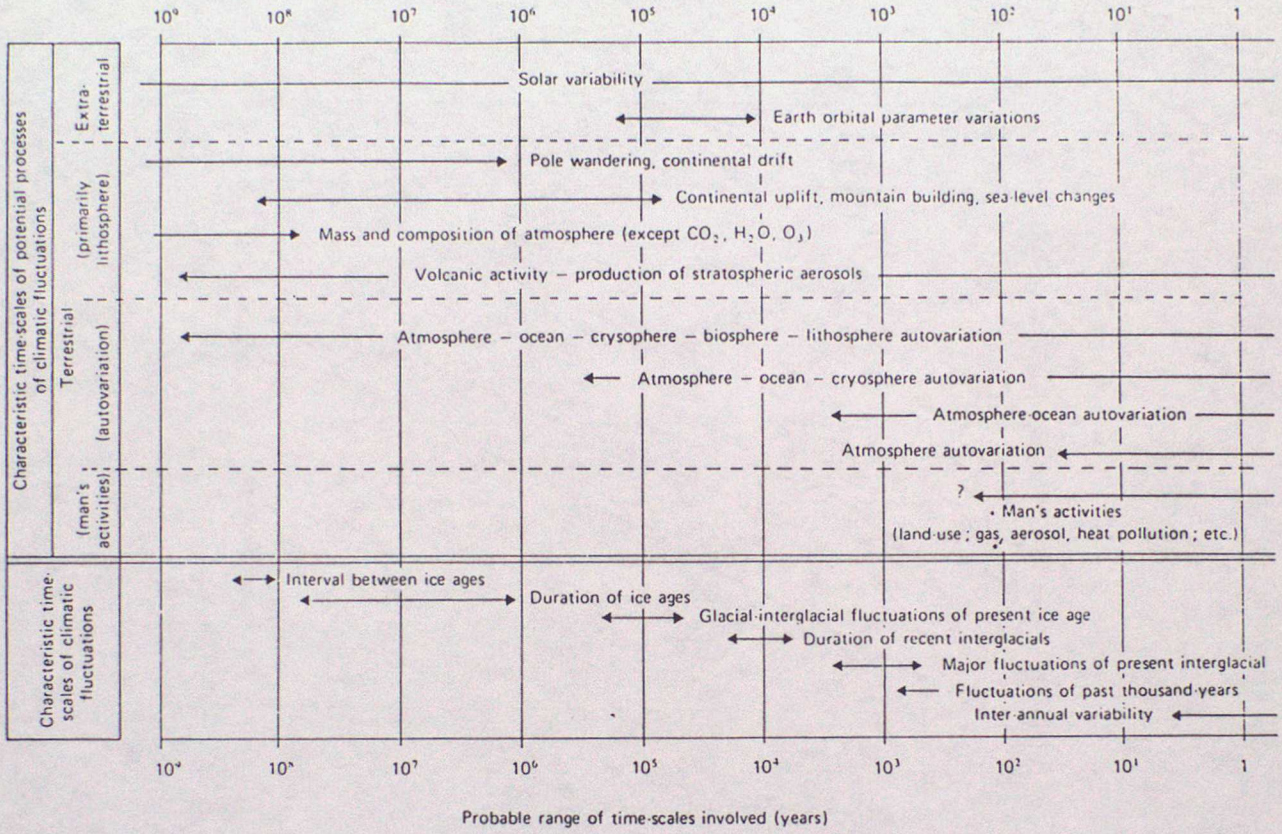

Examples of potential processes involved in climate fluctuations (top) and characteristic time scales of observed climatic fluctuations (bottom) (Kutzbach, 1974). (Reproduced from The Physical Basis of Climate and Climate Modelling, *WMO Garp Series, No. 16, p. 9, figure 2.6, with permission of WMO.)*

Figure 8.2

$$c_a \dot{T}_a = -\alpha T_a - \beta(T_a - T_m) + q$$

$$c_m \dot{T}_m = \beta(T_a - T_m) - \gamma(T_m - T_d)$$

$$c_d \dot{T}_d = \gamma(T_m - T_d)$$

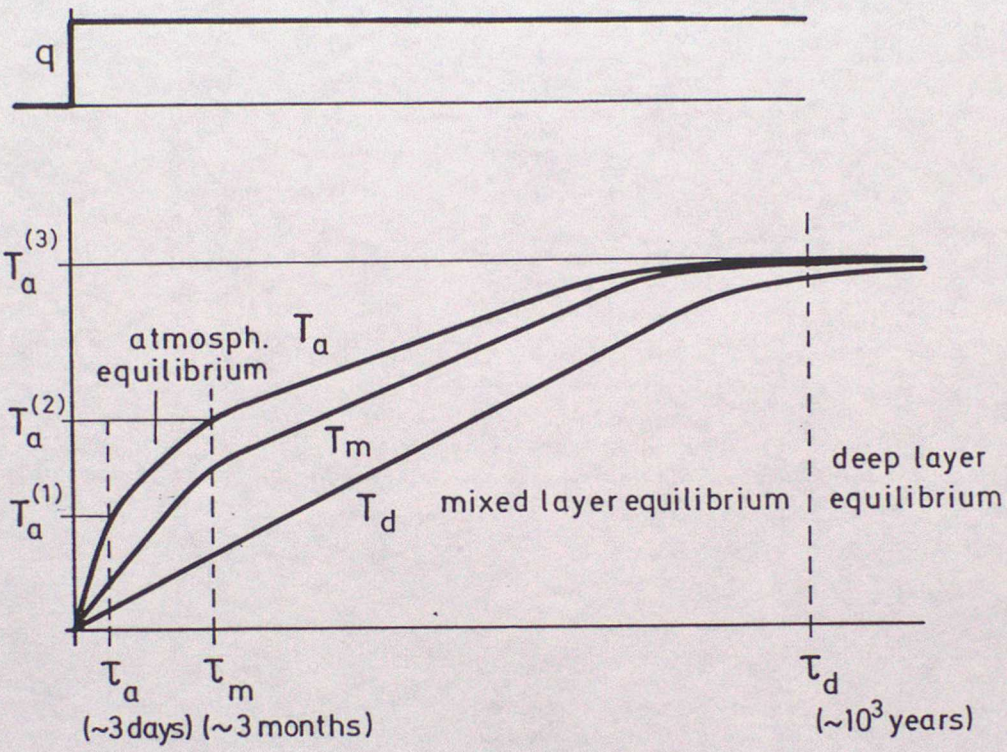

Response of the atmospheric temperature T_a, mixed-layer temperature T_m and deep-ocean temperature T_d to a step-function change in heating q (schematic).

Figure 8.3

Figure 8.4 Salinity on the 3 C temperature surface (From Worthington and Wright, 1970)

Schematic diagram (Dietrich, Kalle, Kraus and Siedler, 1980) of water masses of the Atlantic.

(a)

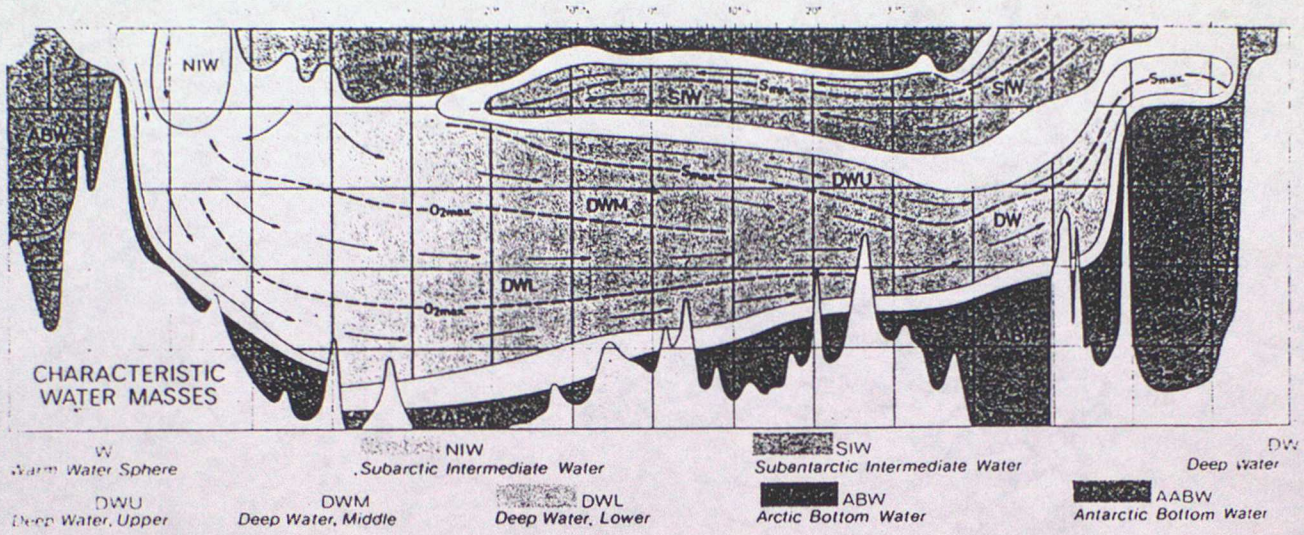

(b)

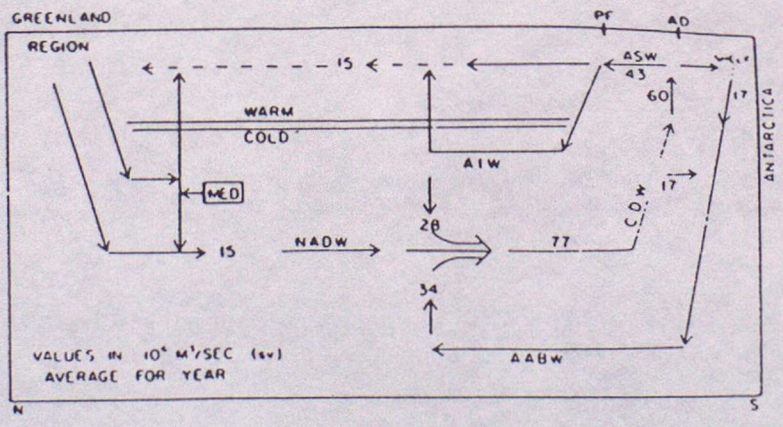

Figure 8.5

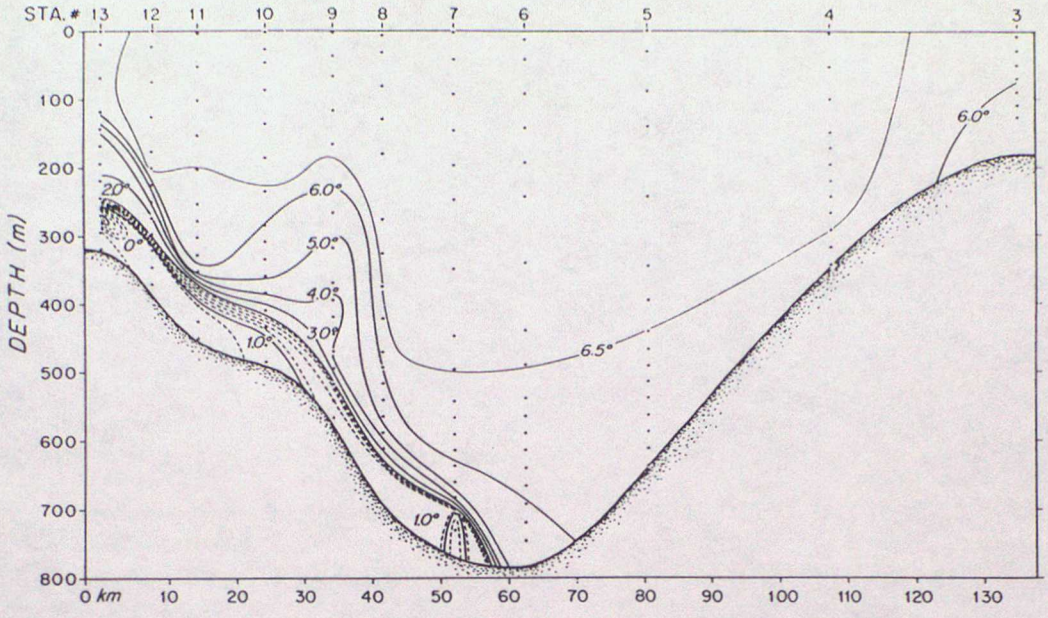

Temperature (°C) section across the Denmark Strait in lats. 65-66°N (left, west; see figure 1.7), illustrating the southward flow of cold water from the Norwegian Sea. C.S.S. *Hudson* cruise BI 0267, stations 3-13, 28-29 January 1967. (Worthington, 1969.)

Figure 8.6

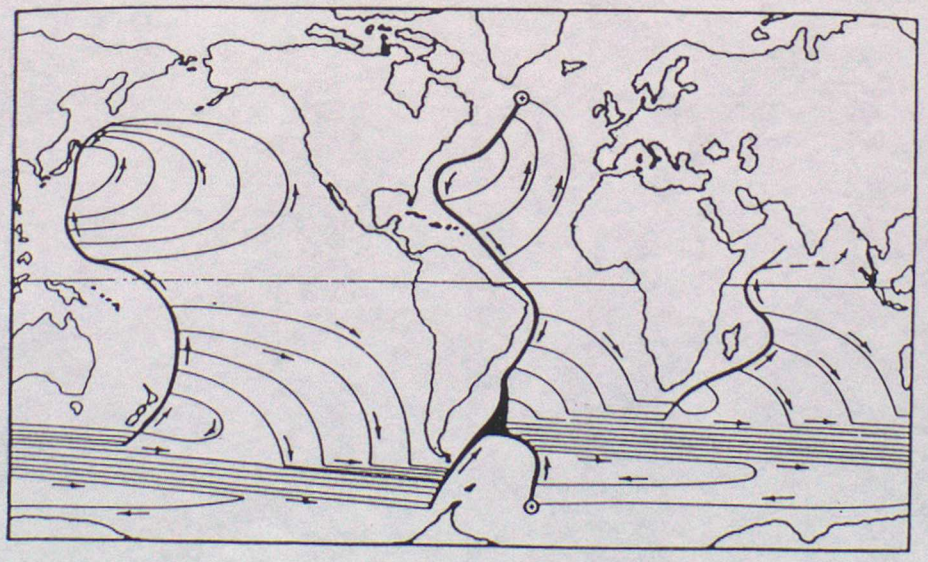

A schematic of the abyssal circulation of the world's ocean, driven by sources in the North and South Atlantic. If the two sources, ⊕, in the North and South Atlantic are taken as $20 \times 10^6\ m^3\ s^{-1}$ *each, then transport between the streamlines is of the order of* $5 \times 10^6\ m^3\ s^{-1}$. *(Reproduced from H. Stommel (1958),* Deep Sea Research, *5, 81, figure 1, with permission of Pergamon Press.)*

Figure 8.7

Figure 8.8

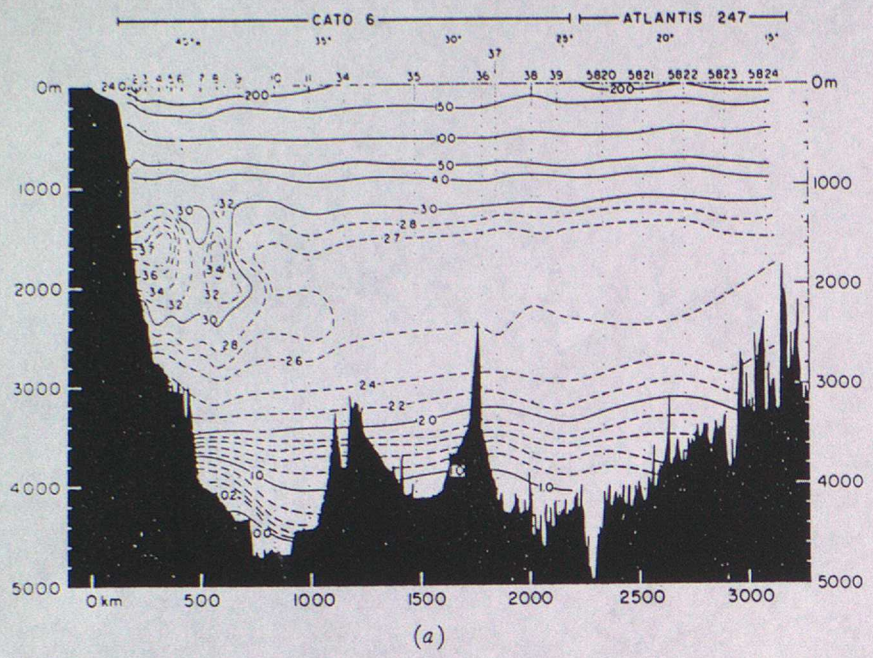

(a)

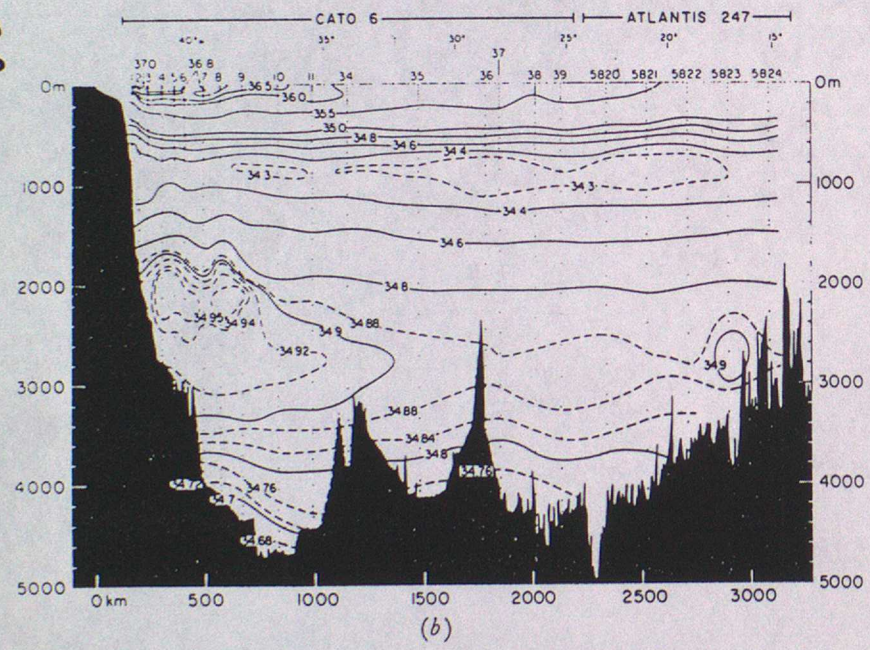

(b)

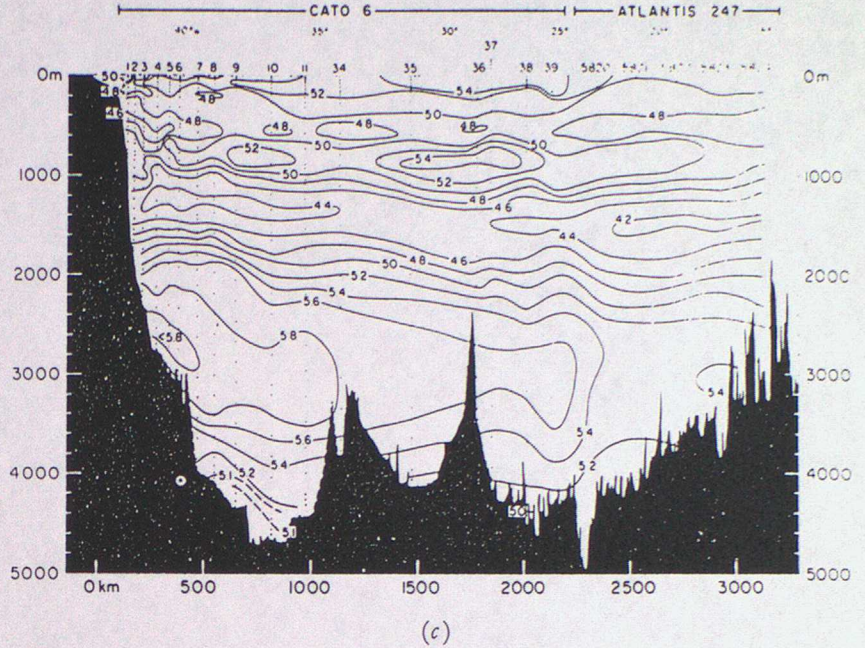

(c)

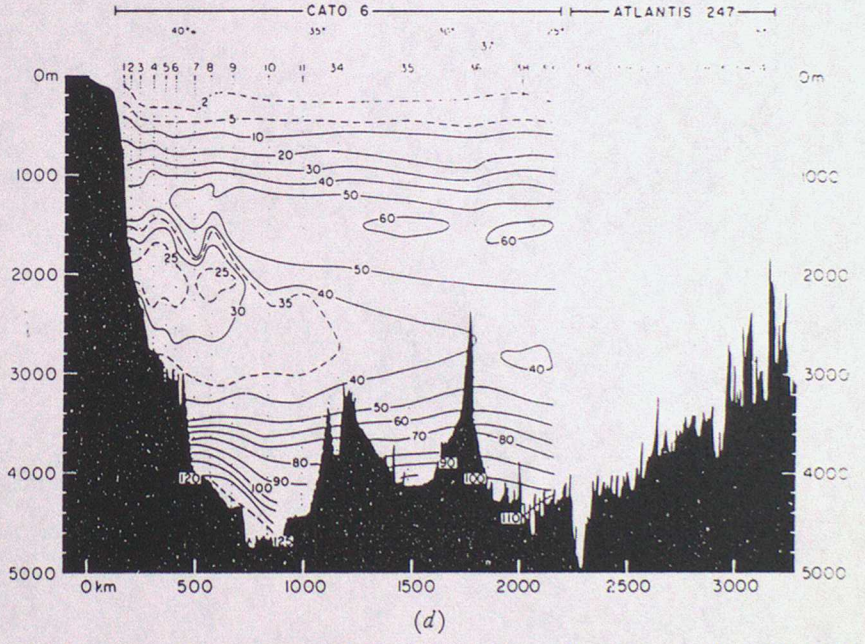

(d)

Sections of (a) potential temperature (°C), (b) salinity (‰), (c) concentrations of dissolved oxygen (ml l^{-1}) and (d) silica (ml l^{-1}) along roughly latitude 30°S from South America (left) to the Mid-Atlantic Ridge, illustrating the two deep western boundary currents of the South Atlantic, namely, the northward flowing Antarctic Bottom Water and the southward flowing North Atlantic Deep Water above. (Reproduced from J. L. Reid et al., J.P.O., *7, 62–91, figure 3a and 3b, with permission of the American Meteorological Society.)*

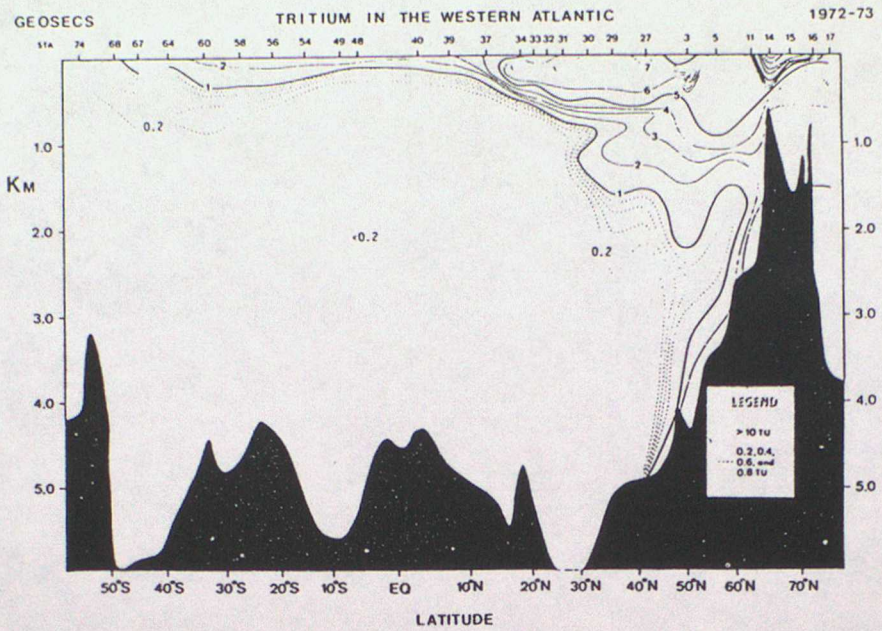

Figure 5.16. Tritium section along the western basin of the Atlantic Ocean obtained during the GEOSECS programme. (Reproduced from Ostlund and Fine (1979), I.A.E.A. –SM–232167, with permission of the IAEA.)

Figure 8.9

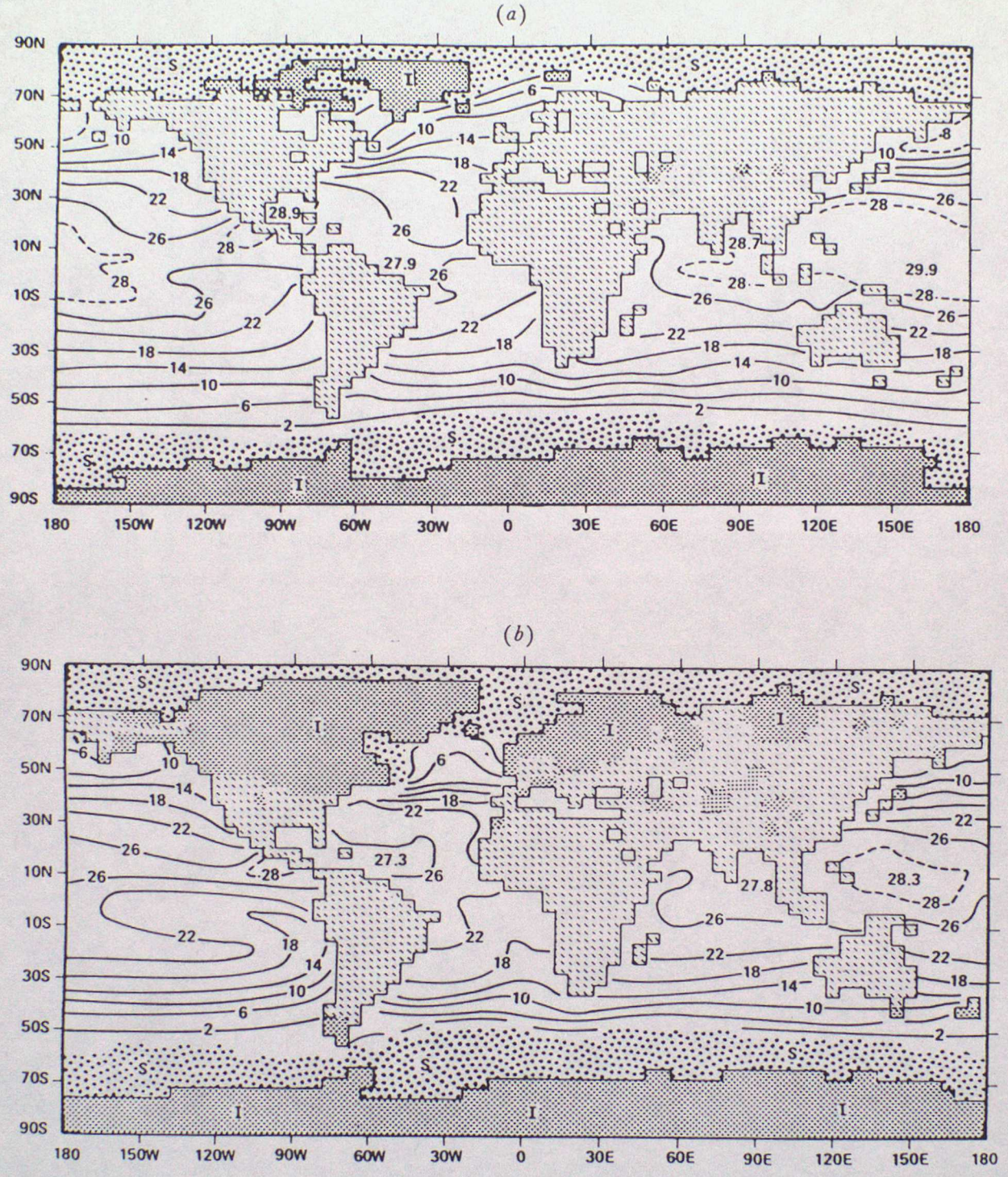

(a) Present annual mean sea surface temperature. (b) Estimated sea surface temperature 18,000 years ago at height of glaciation as determined by CLIMAP studies of fossil assemblages in deep-sea cores. (Reproduced from W. L. Gates (1976), Modelling the Ice Age climate, Science, **191**, *1139, with permission of the American Association for Advancement of Science.)*

Figure 8.10

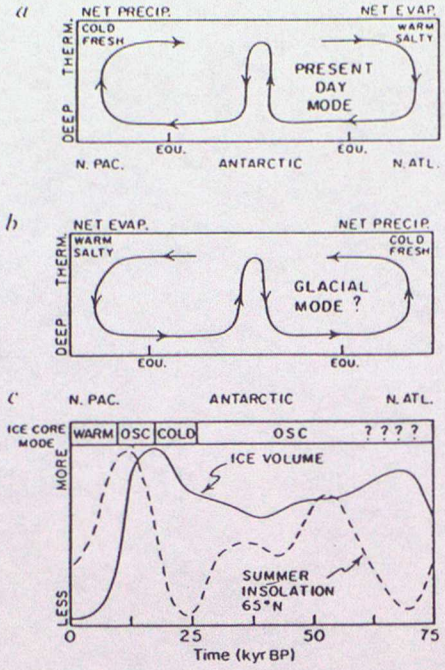

Figure 8.11

a, *b*, Two possible extreme modes of ocean circulation are proposed here, corresponding to the warm and cold intervals seen in the ice-core record. *c*, The times when the ice-core record shows the system to have been locked in its warm mode, to have been locked in its cold mode or to have been oscillating between these modes are shown with the ice-volume record and the Northern Hemisphere high-latitude summer insolation record. The intervals of warm Greenland climate correspond to intervals of low ice volume and high summer insolation and the intervals of cold Greenland climate correspond to times of high ice volume and low summer insolation. The intervals when Greenland climate oscillated between warm and cold corresponded to times when the ice volume–summer insolation product had intermediate values. This suggests that the atmospheric transport of water vapour between the Atlantic and Pacific changes with ice cover and summer insolation.

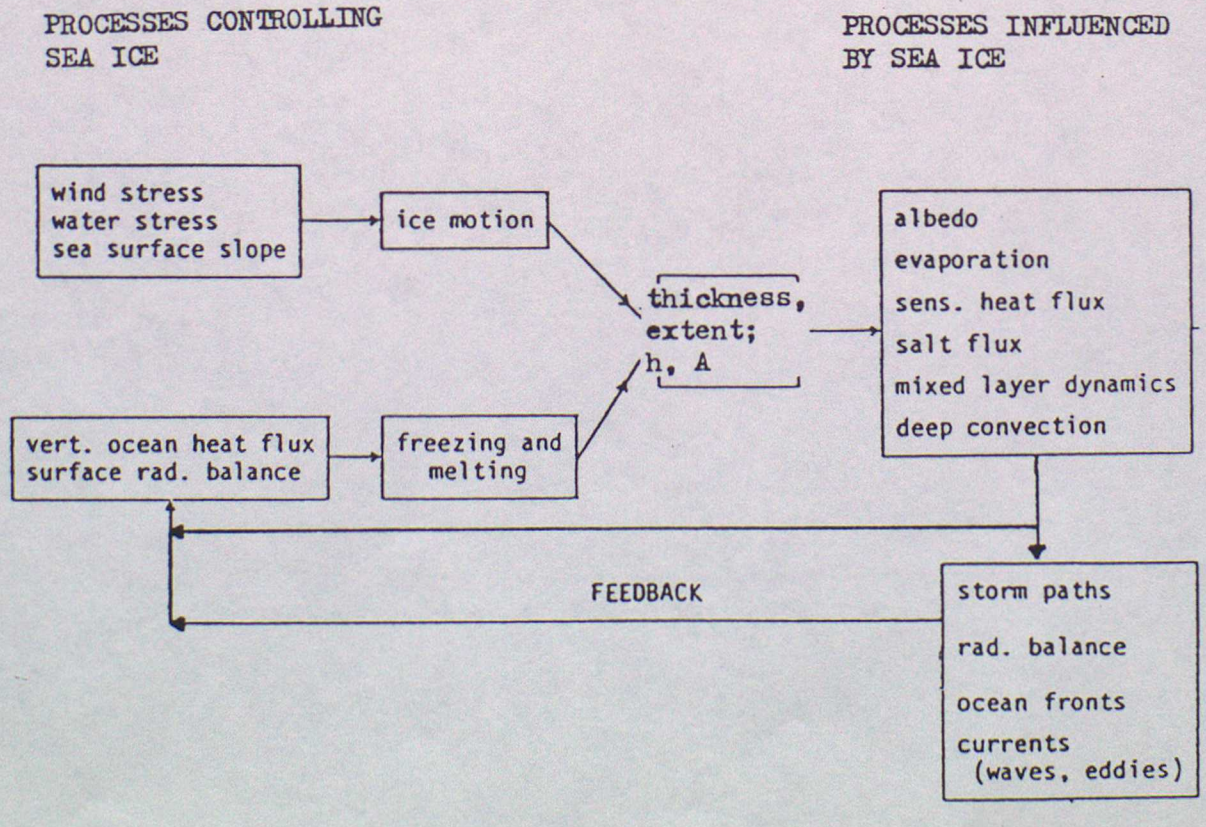

Figure 8.12 Schematic illustration of sea ice processes.

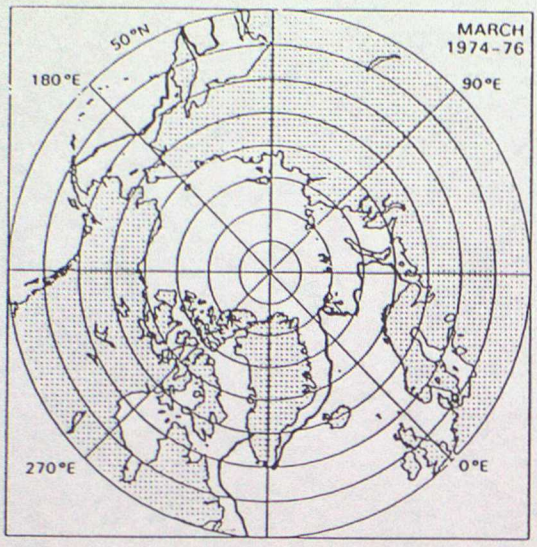

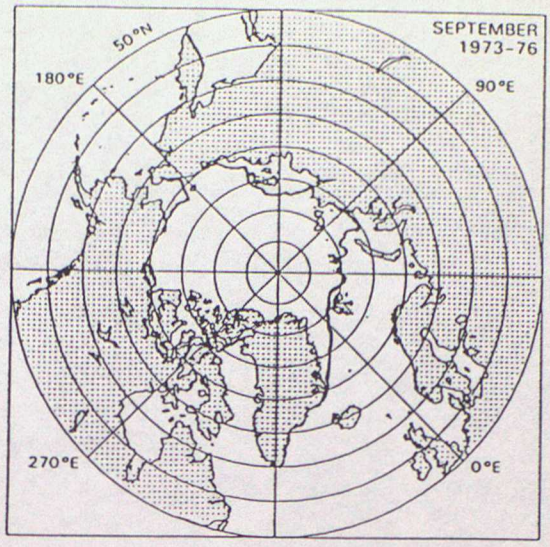

(a) Sea-ice extents for March and September, derived from satellite data.

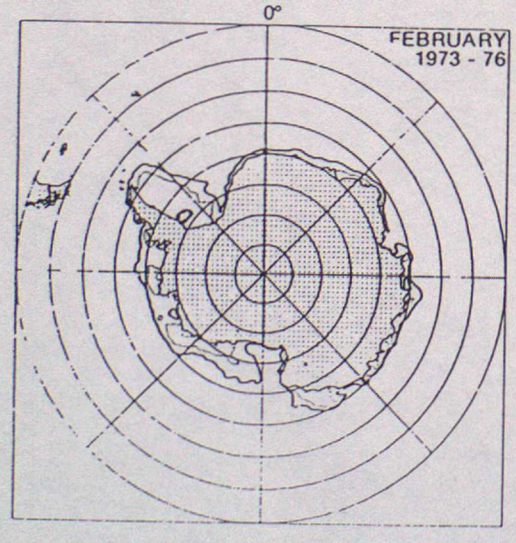

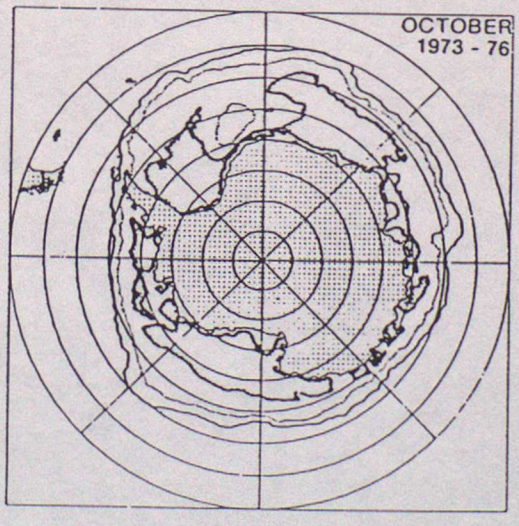

(b) Sea-ice extents for February and October, from satellite data. Here the solid, dotted and spiked lines indicate ice concentrations of 15%, 50% and 85% respectively.

Figure 8.13

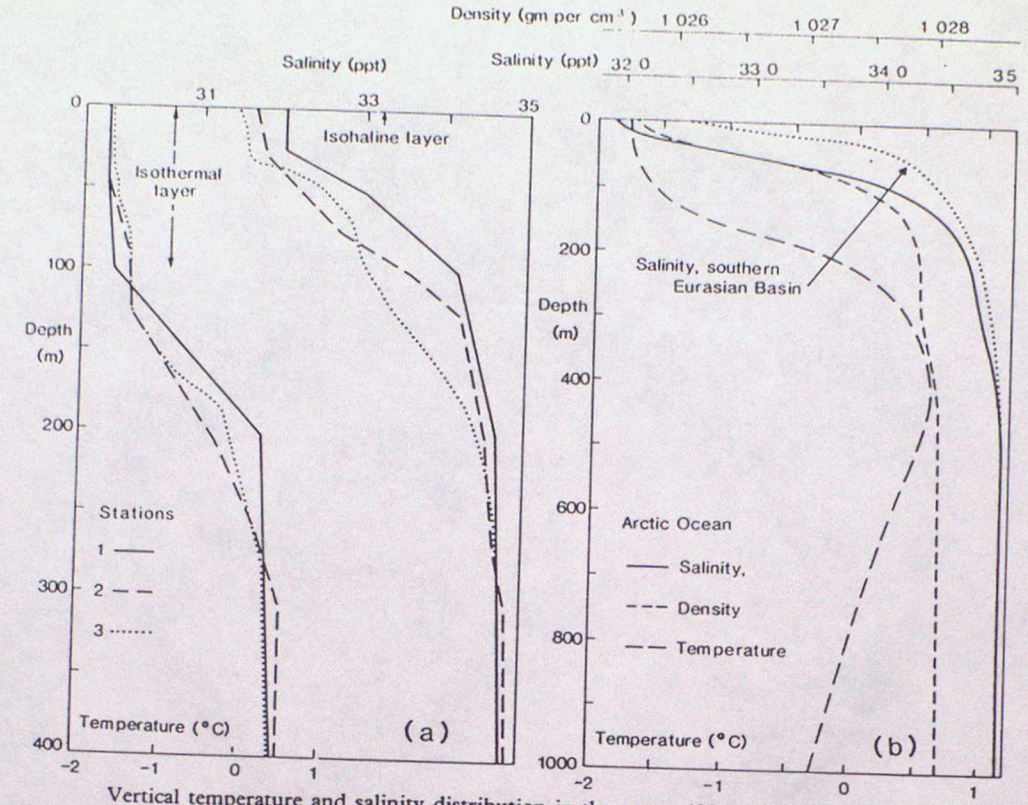

Vertical temperature and salinity distribution in the upper 400 m of the Arctic Ocean in winter; for positions of stations see Figure 3. After Aagaard and others (1981); (b) Composite vertical distributions of temperature, salinity and density (calculated for a pressure of 1 atm.) in the Arctic Ocean, and of salinity in the Southern Eurasian basin. From Aagaard and Coachman (1975).

Figure 8.14

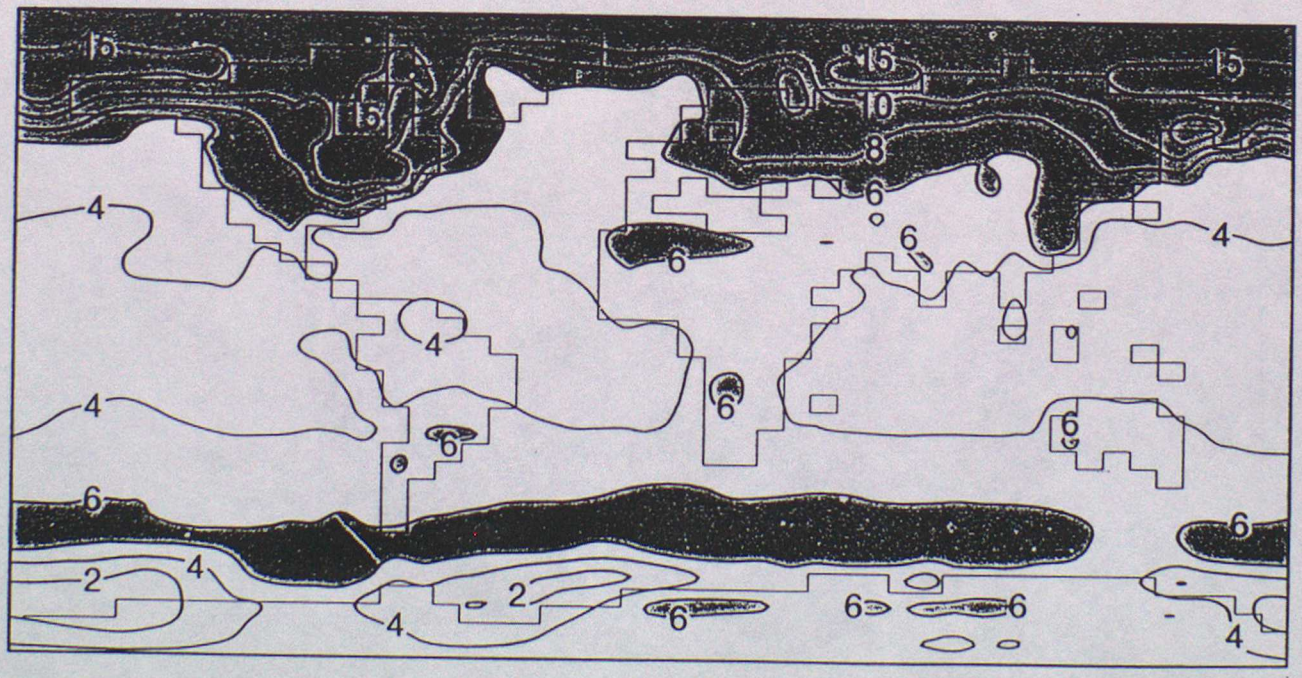

Figure 8.15 Average (15 year mean) changes in surface temperature (° C) for Dec-Feb due to a doubling of CO_2 in a coupled slab ocean-atmosphere model. (J F B Mitchell, Met O 20)

Northern hemisphere continental ice, sea ice, and sea surface temperatures in August at present and 18000 BP. (From CLIMAP, 1981.)

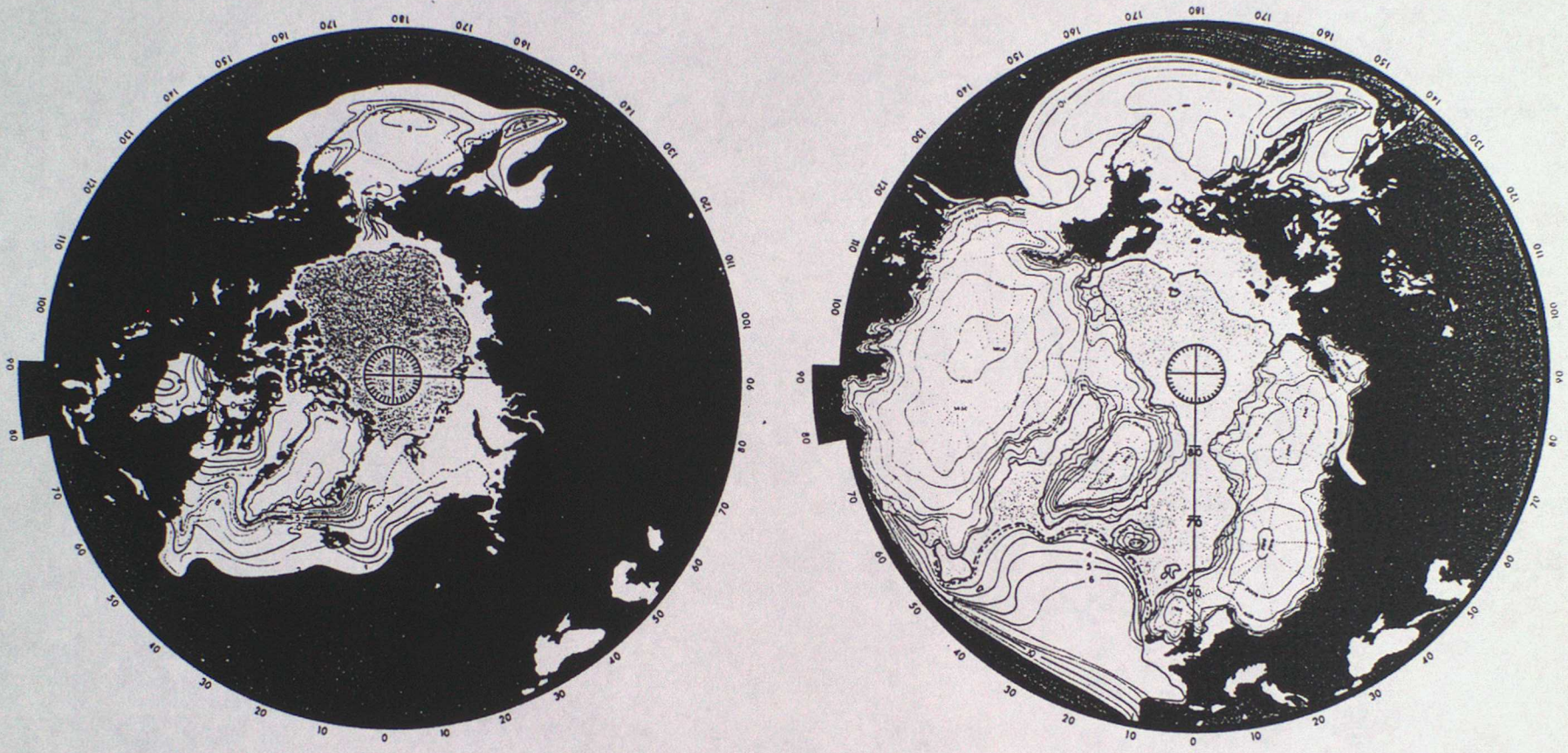

Figure 8.16

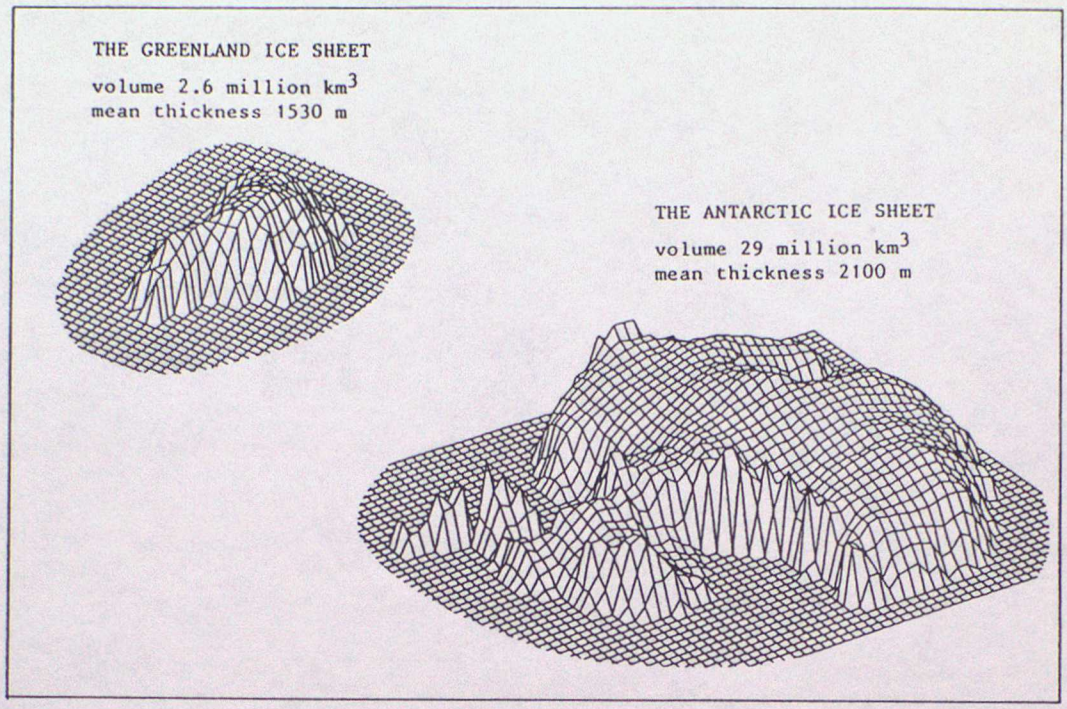

Isometric plots of the Greenland and Antarctic ice sheets. The grid parameter is 100 km.

Figure 8.17

The west antarctic ice sheet, containing the two largest ice shelves of the continent, and a large area of ice grounded below sea level (to a maximum depth of 2500 m). (After Mercer, 1978.)

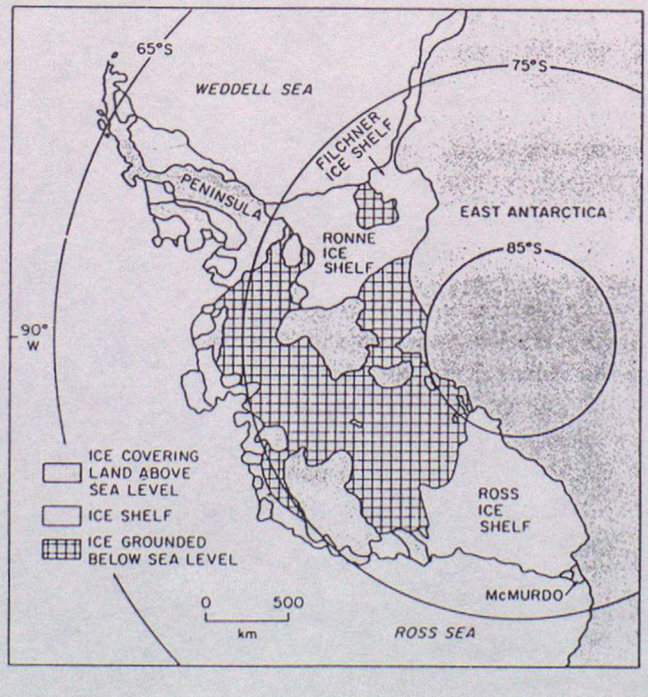

Figure 8.18

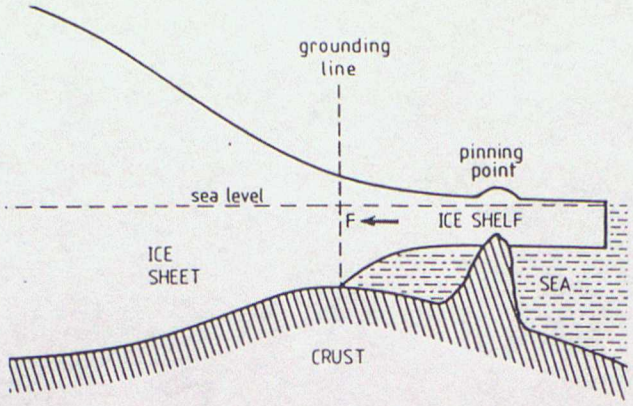

An ice sheet - ice shelf system typical for the West Antarctic Ice Sheet. Pinning points effect ice flow from the main sheet.

Figure 8.19

THE PHYSICS AND DYNAMICS OF THE CLIMATE SYSTEM

Simulation of Climate

John F B Mitchell
Dynamical Climatology Branch
Meteorological Office, Bracknell

9.1 INTRODUCTION

It is well known that the climate of the earth has been very different from present, as for example during the major Ice Ages. Awareness of the possibility that man can change the atmospheric environment has been heightened in the last few years by publicity concerning "Acid rain", "The ozone hole" and the "Greenhouse effect". The advent of electronic computers has made it possible to develop 3-dimensional models of the atmosphere and oceans which have been used to investigate these phenomena. In these two lectures, we will consider the simulation of global climate, past, present and future.

Climate may be regarded as the statistical distribution of temperature, rainfall and other such parameters over a period of time at a given location. Thus, for example, we are not only concerned with the long-term mean monthly temperatures, but also the variability from day to day, and from year to year. In assessing the impacts of changes in climate, the changes in the frequency of extreme events such as frosts, gales, droughts and heatwaves are as important as the changes in mean parameters. As the climate varies over all timescales (Figure 9.1), the length of the averaging period will vary from 30 years or so for contemporary climate (for example, Schutz and Gates, 1971), through millennia when variations in orbital parameters are being considered, to geological timescales.

In order to simulate climate it is evident from the definition just given that we must be able to model temporal and spatial variability. Thus we are compelled to use 3-dimensional general circulation models (GCMs) of the atmosphere and oceans. Such models are expensive to run and it is often difficult to analyse their behaviour. Hence models of lower dimension have

been used to investigate a wider range of parameter changes than is possible with a full model, or identify the dominant mechanisms in a GCM experiment.

Climate models, unlike numerical weather prediction models, cannot be validated against a large number of test cases. Although climate has varied in the past, the causes of these variations are not generally well known and our knowledge of past climates themselves is imprecise because of uncertainties in the interpretation of palaeoclimatic data. Thus, the usual scientific cycle of observation, making an hypothesis, validating the hypothesis against further independent observations and so on is difficult to achieve. It is therefore particularly important that climate models should be firmly based on physical principles and validated against whatever data there is available. These two topics are discussed further in the remainder of this paper.

9.2 ATMOSPHERIC MODELS AND THEIR PHYSICAL BASIS

In this section, the physical basis of climate models is discussed using atmospheric models as an example. A similar approach is taken in modelling the oceans, sea-ice and the land surface, but these components will not be discussed further. The purpose of this section is to outline the principles used in constructing a climate model as opposed to providing a comprehensive review of current climate models. Examples will be taken predominantly from the Meteorological Office climate model (Wilson and Mitchell, 1987a, henceforth referred to as WM; Slingo et al, 1988).

9.2.1 Dynamics and physical parametrizations

In a numerical model, the atmosphere is represented by values of wind, temperature and humidity which are held at various levels of grid points. For example, the model used by WM has 11 levels in the vertical and horizontal spacing of 5° latitude by 7.5° longitude (Figure 9.2) typical of current climate models. At any time t the state of the atmosphere is described by about 10^5 variables, and the values at some future time $t+\Delta t$

can be determined using the prognostic equations described below. Δt is of order 20 minutes. The Met. Office climate model (WM) requires 4.5 hours of elapsed time on Cyber 205 for each simulated year.

The prognostic equations are based on the laws of classical physics, and the local rates of change $\frac{\Delta \underline{Y}_i}{\Delta t}$ at each location and level $\underline{X}$ are given by

$$\frac{\Delta \underline{Y}_i}{\Delta t} = F_i(\underline{Y}, \underline{X}, t) \qquad Y_i = u, v, T, q \tag{9.1}$$

where u and v are the east-west and north-south components of wind, T is temperature, q is humidity, F_i is a function of all the variables $\underline{Y}$, and their spatial gradients at that location. Equation (9.2) may be expanded.

$$\frac{\Delta \underline{Y}_i}{\Delta t} = \underset{(a)}{-\underline{\nabla} \cdot \underline{V}\, Y_i} + \underset{(b)}{Z} + \underset{(c)}{D} + \underset{(d)}{N} \tag{9.2}$$

Where the term

(a) is the change in Y_i due to transport by the flow

(b) represents the effects of pressure gradients and the earth's rotation in the wind equation, and of adiabatic vertical motion in the temperature equation

(c) are smoothing (diffusive) terms

(d) are the sources and sinks of momentum (i=u,v), heat (i=T) and moisture (i=q).

The left-hand side and the terms (a) and (b) are often referred to as the large scale dynamics. The equations for u and v may be transformed into 2 equations for divergence and the vertical component of vorticity, and so may be solved using spectral techniques (see, for example, Schlesinger 1988): otherwise they are solved using finite difference techniques. In solving the equations, care must be taken that there are no spurious sinks of heat, moisture or momentum. This is particularly important for models used in climate change experiments, since the sizes of the perturbations typically considered are small (4 Wm^{-2} in the case of doubling carbon dioxide concentrations (Lal and Ramanathan, 1984)). The diffusive terms

(c) are required to prevent energy accumulating in the smallest scales resolved by the model grid and producing unmeteorological solutions. These terms can be regarded as representing small-scale motions not resolved by the grid.

The final term in 9.2 covers all the small-scale processes not incorporated in (c), including boundary and surface processes, radiation and convection. For some of these phenomena, notably radiation, there exists an accepted theoretical basis, and accuracy is limited by the availability of computer resources and the necessity of using grid-box values of parameters which in reality may vary substantially within a grid box. For other processes, there may be no accepted underlying theory, or the theory may be valid only for limited idealized conditions. The subgrid scale parametrizations may be derived on the basis of one or more of the following:

a. Simplified forms of the exact equation (if known)
b. Numerical experiments on a much finer mesh than feasible in the GCM.
c. Observations from the atmosphere
d. Laboratory experiments
e. Sensitivity studies made with general circulation models.

To illustrate the diversity of these approaches, the derivation of the radiative and convective parametrizations are considered in more detail.

In principle, the equations of radiative transfer are well known (see for example Paltridge and Platt, 1976) and detailed measurements of the absorption of radiation as a function of wavelength have been made for the principal atmospheric absorbers. Thus the accuracy of radiative fluxes under clear skies is limited only by computational effort. Since the explicit integration of the full equations for the vertical flux of long-wave radiation F(z)

$$F(z) = \int_0^\infty d\nu \int^\infty \frac{d\mu}{\mu^3} \int_z^\infty dz' \Pi\, B(\nu,z') \frac{d}{dz'} \exp\left\{-\mu \int \sum_i S_i(z'') f_i(\nu,z'')\, dz''\right\}$$

(from Rodgers, 1977) includes a double integration over the vertical co-ordinate z, integrations over all angles represented by μ and all frequencies ν and a summation over all spectral lines i, much effort has been devoted to simplifying the equations and devising efficient mathematical methods of solution. The Met. Office model currently uses an emissivity approximation which involves a single integration over the vertical co-ordinate and a summation over 7 broad bands (Slingo and Wilderspin, 1986). The radiative properties of water clouds can be derived theoretically provided the droplet-size distribution is known. Ice clouds are comprised of non-spherical particles which may vary in shape and orientation, making it difficult to estimate the radiative properties theoretically. The major uncertainties in radiative effects of ice and water cloud arise in determining cloud properties (height, thickness, extent, water content and droplet (particle) characteristics) from grid scale model variables.

Much of the vertical transport of heat, moisture and momentum is the result of vertical motions on scales much smaller than a model grid box such as cumulus convection. Unlike radiative transfer, there is no generally accepted underlying theoretical basis for parametrizing convective motions. However, some general principles can be applied. If the atmosphere becomes statically unstable, the vertical profile will adjust towards the dry adiabat (or moist adiabat if saturation occurs), conserving moist static energy, $C_pT + Lq + gz$. This is the basis of adjustment schemes, such as the moist convective adjustment scheme of Manabe and Strickler (1964) which instantaneously removes convective instability, and the Betts-Miller scheme (Betts and Miller, 1984) which relaxes the vertical profile towards reference profiles defined from observational data. Other schemes (Arakawa and Schubert, 1974; Lyne and Rowntree, 1976, used in current Met. Office models) distinguish explicitly between small-scale ascent in convective towers and large-scale subsidence and warming of environmental air. A third approach taken by Kuo (1974) links convection directly to the large-scale convergence of moisture in a vertical column, including that due to surface evaporation, repartitioning the moisture supply between

precipitation and moistening the column. In all but the moist convective adjustment scheme, there are explicit tunable parameters which may be chosen by testing the scheme against observed data such as those from the GARP Atlantic Tropical Experiment (GATE, Lyne et al, 1976) or by carrying out sensitivity experiments using the full model. A shortcoming of the former approach is that the large-scale convergence of heat and moisture is not well known, whereas in sensitivity experiments, errors in other parametrizations may degrade the performance of the convection scheme. Further guidance may be obtained from observations and numerical simulations of individual convective cells.

The factors guiding the development of various parametrizations used in a recent version of the Met. Office climate model (WM) are shown in Table 1. Note that apart from the snow free land reflectivities which are derived from observational data, adjustable parameters are prescribed with the same value over the whole globe, although separate values may be allocated to land and sea points. Hence there is a limit to the tuning possible in order to optimize the simulation of regional climate.

9.2.2 Using a climate model

Certain features, referred to here as boundary conditions, must be specified before a GCM can be integrated. For an atmosphere-only model, these include carbon dioxide and ozone concentrations, sea surface temperatures and sea-ice extents, orography and time of year. The normal procedure is then to integrate the model over the period of interest and look at the long-term statistics of the simulation. In the case of a climate change experiment, a second simulation is made changing only the relevant boundary conditions (for example carbon dioxide concentrations) and the long-term characteristics of the two simulations are compared. Note that even with fixed boundary conditions, the simulation will vary in time due to the inherent variability of climate. Hence it is necessary to perform statistical tests on the differences between the control and perturbed simulations in order to establish that the probability that such differences could have arisen by chance is small.

The length of simulation will depend on a variety of factors. First, the time taken for the model to adjust to the prescribed boundary conditions will vary from a week or so for prescribed sea surface temperature experiments to decades or even centuries in the case of coupled ocean-atmosphere models. Second, the length of time for which prescribed boundary conditions are valid will also vary, from a month or so for sea surface temperature anomalies to thousands of years in the case of orography. Third, the integrations must be sufficiently long (or numerous) to allow the statistics of the simulated climate to be defined. In practice, the length of a simulation is often limited by the computational resources available.

In the above approach, there are certain underlying assumptions whose validity may affect the relevance of the results to observed climate.

(a) A "mean" or quasi-equilibrium state exists in nature and in the model. As discussed in the introduction, the climate of the earth has varied considerably over a wide range of timescales. Thus in the real world at least, we do not know if statistically stationary climatic states exist. The problem of the stability of climatic states has been addressed using "simple" models (see for example Fraedrich 1978, Ghil and Childress, 1987) and will not be considered further here.

(b) The "mean" state is unique, and independent of the initial state. Lorenz (1975) suggested that the earth's climate may have more than one stable state, and that transitions between these states may be rare (climate is almost "intransitive"). It follows that the choice of initial conditions may determine which of the stable states evolve. For example, Wetherald and Manabe (1975) found that a simulation made with an idealized climate model which commenced with an ice covered surface remained ice-covered, whereas when the initial conditions were free of ice, only polar latitudes became ice-covered.

(c) The model converges, and converges to the correct solution. Although mathematical models of climate may be based on sound physical principles, this is not sufficient to guarantee that the model will produce the correct solution. We cannot check the convergence of such complex models using mathematical stability analyses, so the only way to check for convergence is to integrate the model and look at the results.

9.2.3 Verification

The validity of the model can be assessed on a variety of timescales against observational data. As climate models can be regarded as a development of numerical weather prediction models, one can specify initial conditions from meteorological analyses, perform short-range forecasts and compare the evolution of synoptic features in the model with those observed (for example, Carson and Cullen, 1976). A similar approach can be taken using long-range forecasts (Mansfield, 1986), though after a period of a week or so, the correspondence between individual simulated and observed features will be lost, and the forecasts of necessity become statistical rather than deterministic.

The traditional method of calculating atmospheric GCMs has been to compare the simulated means with climatological data (Manabe and Holloway, 1975; Mitchell, 1983). For example, by comparing a 4-year mean of simulated mean sea-level pressure from the version of the Met. Office GCM described by Slingo et al (1988) with observational data (Figure 9.3) one can see that the model reproduces all the main features of the observed circulation including the equatorial and mid-latitude pressure troughs, and the subtropical anticyclones which form over the ocean in summer and extend over land in winter. Note however that the simulated pressure ridge over the Rockies is weaker than observed, and the weak trough over Central Europe is much too strong in the model.

The variability in the model may also be assessed: Figure 9.4 shows the simulated and observed high pass filtered 500 mb heights which give an indication of the strength and position of the storm tracks. Again the agreement with observation is good, though the Atlantic storm track is weaker than observed, and penetrates too far south at the European end. One can assess variability on longer timescales including year to year in a similar manner.

The detailed evolution of the seasonal cycle can be assessed by comparing mean monthly grid point data with observations from suitable climatological stations (Reed, 1986). In Figure 9.5, the mean monthly midnight surface temperatures at a model grid point over eastern England are compared with observed 2 m minimum temperatures from Cambridge (Wilson and Mitchell, 1987b). Note the colder than observed spring temperatures. This is associated with more frequent than observed cold spells in the model (Figure 9.6) which are a result of too many or too strong outbreaks of easterly flow off the cold Eurasian continent (Reid, 1986).

The above approach may be used to establish that the mean climate and level of variability in the model are correct. In order to test that the structure of the model's response to specific perturbations is correct, one can examine the response of the model to observed changes in boundary conditions such as sea surface temperature anomalies, and compare the response with that observed. Palmer and Mansfield (1986) have examined the simulated and observed response to different sea surface anomalies in the tropical Pacific, and Folland et al (1986) have examined the relationship between sea surface temperatures and Sahel rainfall, using observations and numerical experiments. A weakness in this approach to model verifications is that in reality factors other than the changes in boundary conditions specified in the model may contribute to observed changes in the atmosphere, including inherent atmospheric variability.

The ability to simulate contemporary climate accurately is a necessary but not a sufficient condition for a model to produce reliable estimates of climate change. It is possible that in choosing values of disposable

parameters which give an accurate simulation of present-day climate, the response of the model to changes in climate may be distorted. Thus, attempts have been made to simulate climates in the past, including the last glacial maximum 18,000 years before present (18 K bp) (Manabe and Broccoli, 1985) and the last northern hemisphere summer insolation maximum (9 K bp), considered in the following chapter. Manabe and Broccoli compared the changes in surface temperature between 18 K bp and present from two different versions of the model with a palaeoclimatic estimate of the temperature change (Figure 9.7). However, the investigation was inconclusive because of both the small differences between the results from the two versions of the models and the uncertainties in the palaeoclimatic data.

9.3 OTHER COMPONENTS OF THE CLIMATE SYSTEM

The approaches used in developing atmospheric models may be applied to other components of the climate system including sea-ice, the oceans and continental ice-sheets. There is considerably less data from the ocean than from the atmosphere. In addition, synoptic eddies in the ocean have a typical length scale of 30 km as opposed to 1000 km typical of the atmosphere and so are not resolved by the current generation of global ocean GCMs. Thus ocean GCMs are even more difficult to validate than atmospheric models. Since the atmosphere, ocean and continental ice-sheets respond on timescales of days, centuries and thousands of years respectively, special care must be taken when representing the interaction between them. Schlesinger (1979) has listed several ways in which an atmospheric model may be coupled to an ocean model, and Bryan (1984) has tested methods for accelerating the convergence to equilibrium of ocean climate models. Alternatively, Hasselmann (1979) has suggested parametrizing the effect of quickly changing elements of a climate model (for example, the atmospheric component of a model which includes the deep ocean).

9.4 Summary

There is a growing interest in the simulation of climate, both in order to predict future changes in climate due to man's activities, and to understand past climatic change. Climate models are based on the laws of classical physics, though processes which occur on scales smaller than the model grid (or timestep) must be approximated (parametrized). This may be done on the basis of theory, observations and laboratory and numerical experiments. Validation of models includes detailed verification of individual components of the model, and the comparison of results from the full model over a variety of timescales with observational data. Certain assumptions concerning the stability of climate and its dependence on specified boundary conditions are implied in the current use of GCMs in climate simulations.

9.5 Acknowledgements

This paper is an enlarged and updated version of a paper "The physical basis of climate modelling" which appeared in "Palaeoclimatic Analysis and Modelling" (Ed Ghazi) published by D Reidel, 1983.

9.6 References

Arakawa, A. and Schubert, W. H. 1974 Interaction of a cumulus cloud ensemble with large-scale environment. Part I. J. Atmos. Sci., 31, 674-701.

Betts, A. K. and Miller, M. J. 1984 A new convective adjustment scheme. ECMWF Technical Report No 43, 65 pp.

Bryan, K. 1984 Accelerating the convergence to equilibrium of ocean-climate models. J. Phys. Oceanogr. 14 (4) 666-673.

Carson, D. J. and Cullen M. J. P. 1976 Intercomparison of short-range numerical forecsts using finite difference and finite element models from the UK Meteorological Office (Paper presented at the joint DMG/AMS International Conference on the Simulation of large-scale Atmospheric Processes, Hamburg, 30 August-4 September 1976). Met O 20 Tech. Note II/81, Meteorological Office, Bracknell.

Clarke, W. C. 1982 Carbon Dioxide Review: 1982 (Ed. W. C. Clarke) Clarendon Press, Oxford; Oxford University Press, New York. 469 pp.

Folland, C. K., Palmer, T. N. and Parker, D. E. 1986 Sahel Rainfall and Worldwide sea temperatures, 1901-85. Nature, 320, 602-607.

Fraedrich, K. 1978 Catastrophes and resilience of a zezro-dimensional climate system with ice-albedo and greenhouse feedback. Quart. J. R. Met. Soc. 105, 147-167.

Ghil, M. and Childress, S. 1987 Topics in Geophysical Fluid Dynamics; Atmospheric Dynamics, Dynamo Theory, and Climate Dynamics. Applied Mathematical Sciences 60, pp 485, Springer Verlag, New York.

Hasselmann, K. 1979 On the problem of multiple time-scales in climate modelling. In "Man's Impact on Climate" (Eds. Back, Pankrath and Kellogg). Developments in Atmospheric Science, 10, 43-55. Elsevier (Amsterdam, Oxford, New York).

Jones, P. D., Wigley, T. M. L., Folland, C. K., Parker, D. E., Angell, J. K., Lebedeff, S. and Hansen, J. E. 1988 Evidence for global warming in the past decade. Nature, 338, 790.

Kuo, H. L. 1974 Further studies of the parametrization of the influence of cumulus convection on large scale flow. J. Atmos. Sci., 31, 1232-1240.

Lal, M. and Ramanathan, V. 1984 Effects of moist convection and water vapour radiative processes on climate sensitivity. J. Atmos. Sci. 41, 2238-2249.

Lorenz, E. 1975 Climatic Predictability, WMO — GARP Publication Series No. 16, Geneva, 132-136.

Lyne, W. H. and Rowntree, P. R. 1976 Development of a convective parametrization using GATE data. Met O 20 Technical Note II/70, Meteorological Office, Bracknell.

Lyne, W. H., Rowntree, P. R., Temperton, C. and Walker, J. 1976 Numerical modelling using GATE data. Met. Mag. 105, 261-271.

Manabe, S. and Broccoli, A. O. 1985 A Comparison of Climate Model Sensitivity with data from the last glacial maximum. J. Atmos. Sci. 42, 2643-2651.

Manabe, S. and Holloway, J. L. Jnr. 1975 The Seasonal variation of the hydrologic cycle as simulated by a global model of the atmosphere. J. Geophys. Res., 80, 1617-1649.

Manabe, S. and Strickler, R. F. 1964 Thermal equilibrium of the atmosphere with a convective adjustment. J. Atmos. Sci. 21, 361-385.

Mansfield, D. A. 1986 The skill of dynamical long-range forecasts, including the effect of sea-surface temperature anomalies. Quart. J. R. Met. Soc., 112, 1145-1176.

Mitchell, J. F. B. 1983 The seasonal response of a general circulation model to changes in CO_2 and sea surface temperature. Q.J.R. Met. Soc., 109, 113-152.

Palmer, T. N. and Mansfield, D. A. 1986 Wintertime Circulation Anomalies During Past El Nino Events, using a High Resolution General Circulation Model II. Variability of the seasonal mean response. Quart J.R. Met. Soc., 112, 639-660.

Paltridge, G. W. and Platt, C. M. R. 1976 Radiative proceses in Meteorology and Climatology. Developments in Atmospheric Science, 5. Elsevier, New York, 318 pp.

Reed, D. N. 1986 "Simulation of temperature and precipitation over eastern England by an atmospheric general circulation model". Journal of Climatology 6, 233-253.

Roeckner, E., Schlese, U., Biercamp, J. and Loewe, P. 1987 Cloud optical depth feedbacks and climate modelling. Nature, 329, 138-139.

Rodgers, C. D. 1977 "Radiative Processes in the Atmosphere". In proceedings of ECMWF Seminars. "Parametrization of Physical Processes in the free atmosphere", 5-66.

Schlesinger, M. E. 1979 Comments on ocean-atmosphere coupling and discussion of the paper "A global ocean-atmosphere model with seasonal variation: Possible application to a study of climate sensitivity". Climate Research Institute, Report No. 39, Oregon State University.

Schlesinger, M. E. 1988 (Ed) Physically-based modelling and simulation of climate and climatic change. Vol. 1. NATO Advanced Study Institute Series. (Reidel, in Press).

Schutz, C. and Gates, W.L. 1971 Global Climatic data for surface, 800 mb, 400 mb (January), R-915-ARPA, RAND, Santa Monica.

Slingo, A. and Wilderspin, R. C. 1986 Development of a revised longwave radiation scheme for an atmospheric general circulation model. Q.J.R. Meteorol. Soc., 112, 371-386.

Slingo, A., Wilderspin, R. C. and Smith, R. N. B. 1988 The effect of improved physical parametrizations on simulations of cloudiness and the earth's radiation budget in the tropics. Submitted to Q.J.R. Meteorol. Soc. (Also Met O 20 DCTN 65).

Wetherald, R. T. and Manabe, S. 1975 The effects of changing the solar constant on the climate of a general circulation model. J. Atmos. Sci. 32, 2044-2059.

Wilson, C. A. and Mitchell, J. F. B. 1987a A Doubled CO_2 Climate Sensitivity experiment with a GCM including a simple ocean. J. Geophys. Res., 92, 13315-13343.

Wilson, C. A. and Mitchell, J. F. B. 1987b Simulated Climate and CO_2 — induced climate change over western Europe. Climate change, 10, 11-42.

9.7 Suggested Bibliography

Physically-based Modelling and Simulation of Climate and Climate Change Vol.1 (1988) Schlesinger, M. E. (Ed), NATO Advanced Study Institute Series, (Reidel, in Press). Excellent chapters by Bourke on spectral methods, and Arakawa on finite differences, as well as other components of climate models.

Numercial Weather Prediction and Dynamical Meteorology (1980) Haltiner, G. J. and Williams, R. T. (John Wiley). Generally good on numerical methods, but out-dated on physical parametrizations.

An Introduction to Three-Dimensional Climate Modelling (1986) Washington, W. M. and Parkinson, C. L. There are not many books on climate modelling, and this is the best to date.

The Global Climate (1984) Houghton, J. T. (Ed). (Cambridge University Press) Contains a series of articles by different authors on various aspects of the climate system.

Table 1 Choice of parameters in the atmospheric component of the model used by Wilson and Mitchell (1987)

	Parameter valid over globe	Tuning Experiments cf climatology	Theory	Detailed Models	Field Observations	Laboratory Experiments
Dynamics						
Diffusion Coefficient	X	X	(X)			
Time Smoothing	X	X				
Radiation						
Gaseous absorption	X		X	X	X	X
Cloud amounts	X	X			X	
Cloud properties	X	X			X	
Surface Reflectivity					X	
Convection						
Parcel size	X	X			X	
Entrainment and Detrainment	X	X	X		X	X
Evaporation	X	X	X		X	
Boundary Layer						
Drag coefficient	X		X		X	X
Surface roughness	X				X	
Other						
Soil moisture	X				X	
Heat flux through ice	X		X	X	X	X

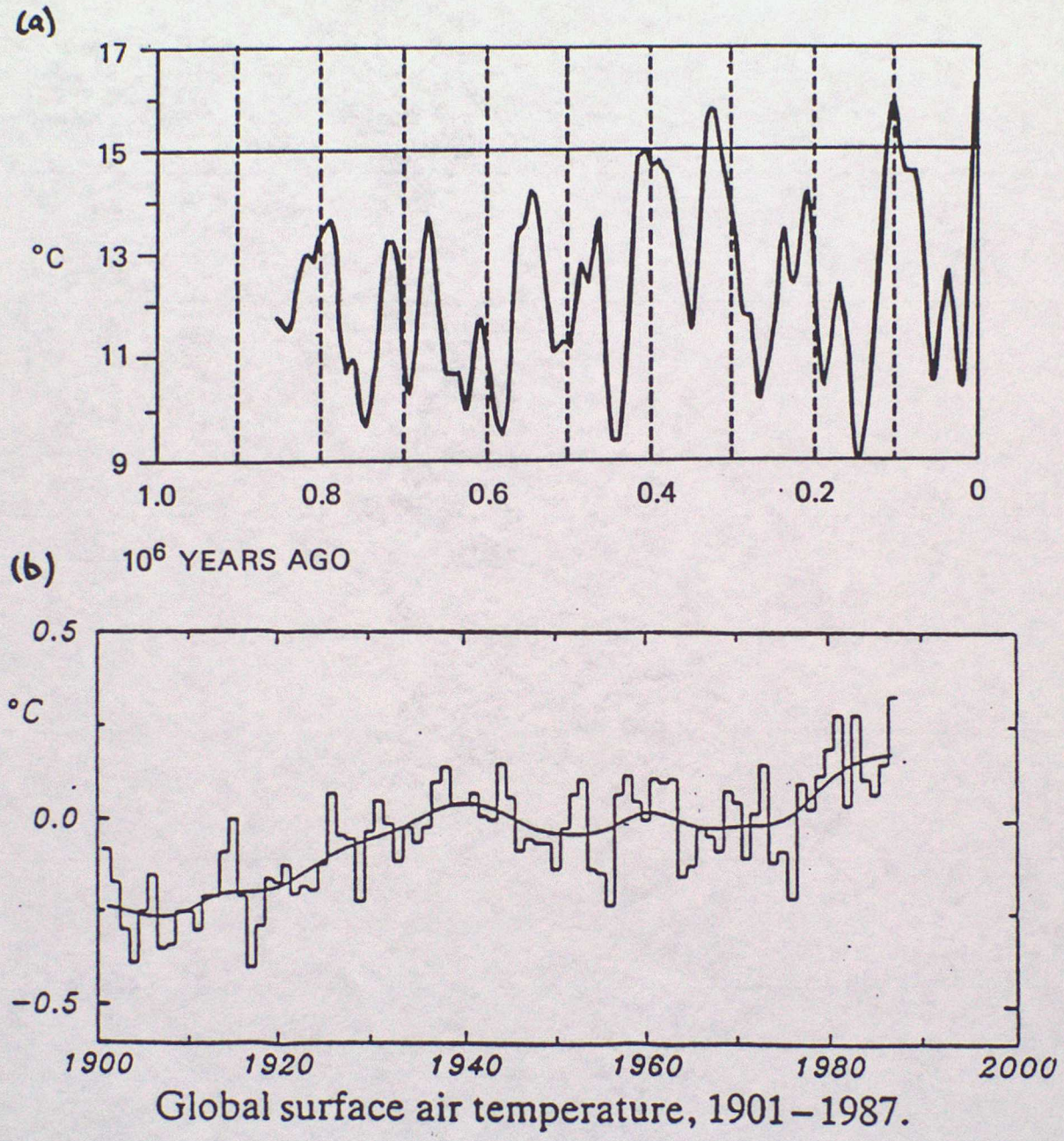

Figure 9.1 (a) Estimated global mean surface temperature over the last 850,000 years (from Clarke, 1982)

(b) Observed anomalies in global mean surface temperature 1901-1987 (from Jones et al, 1988).

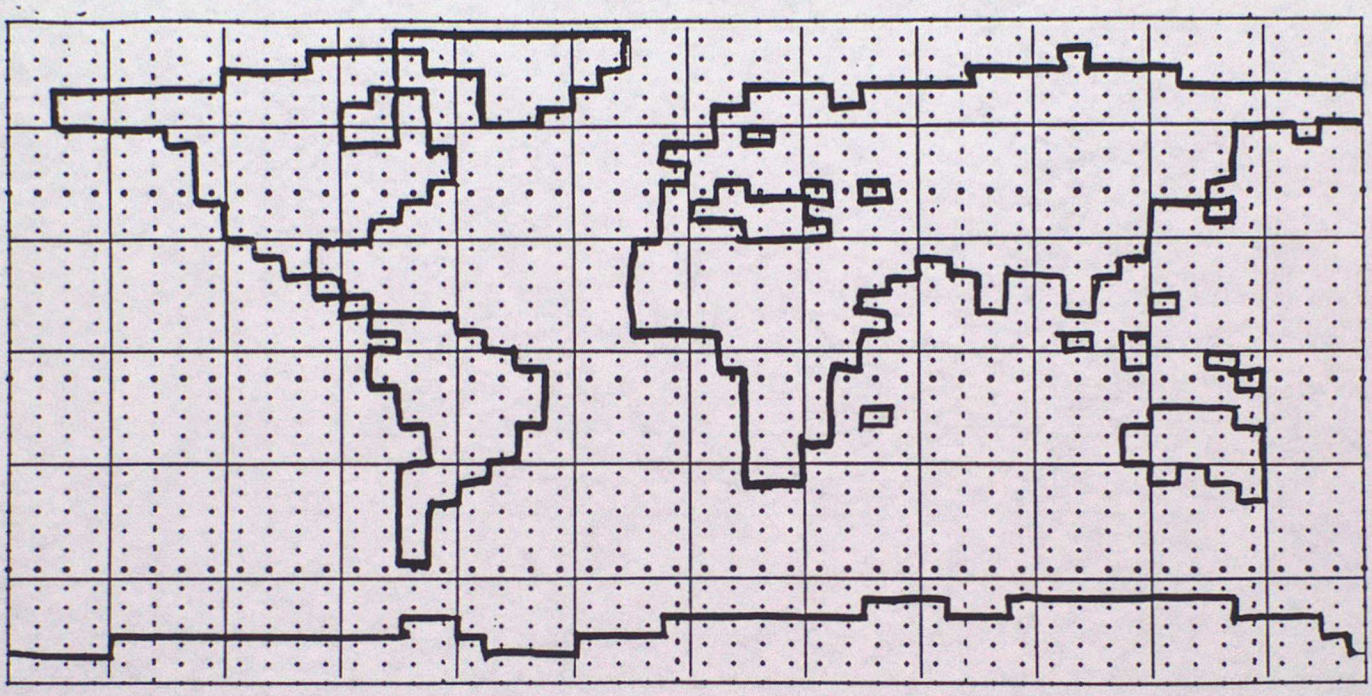

Figure 9.2 The horizontal grid used by WM. This is typical of current climate models. The horizontal spacing is 5° latitude by 7.5° longitude.

Mean-sea-level pressure (mb)

(a) Observed (January)

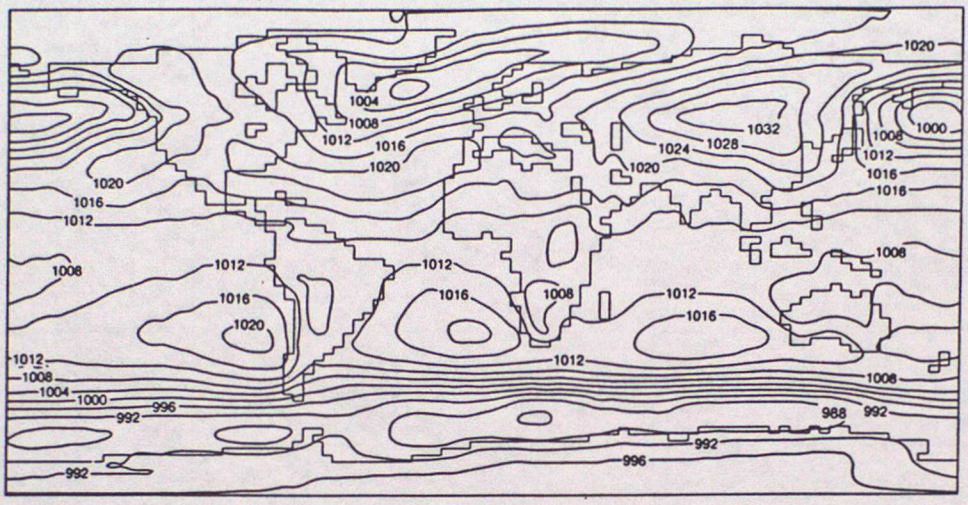

(b) Model (December to February)

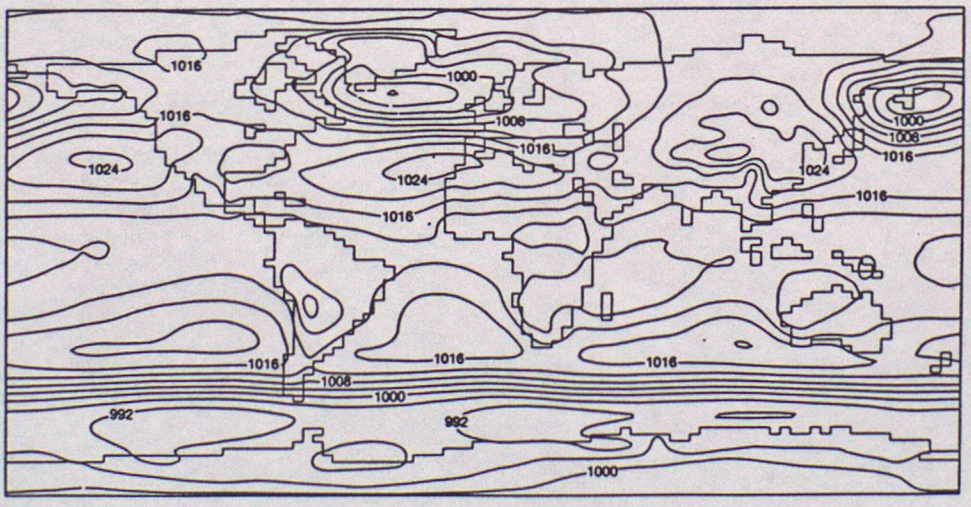

Figure 9.3 Mean sea level pressure (contours every 4 mbs)

(a) January, observed. (Schutz and Gates, 1971)

(b) December to February, simulated using a high resolution version of the Met. Office GCM (see Slingo et al, 1988)

High pass filtered variance of 500 mb heights
(December to February)

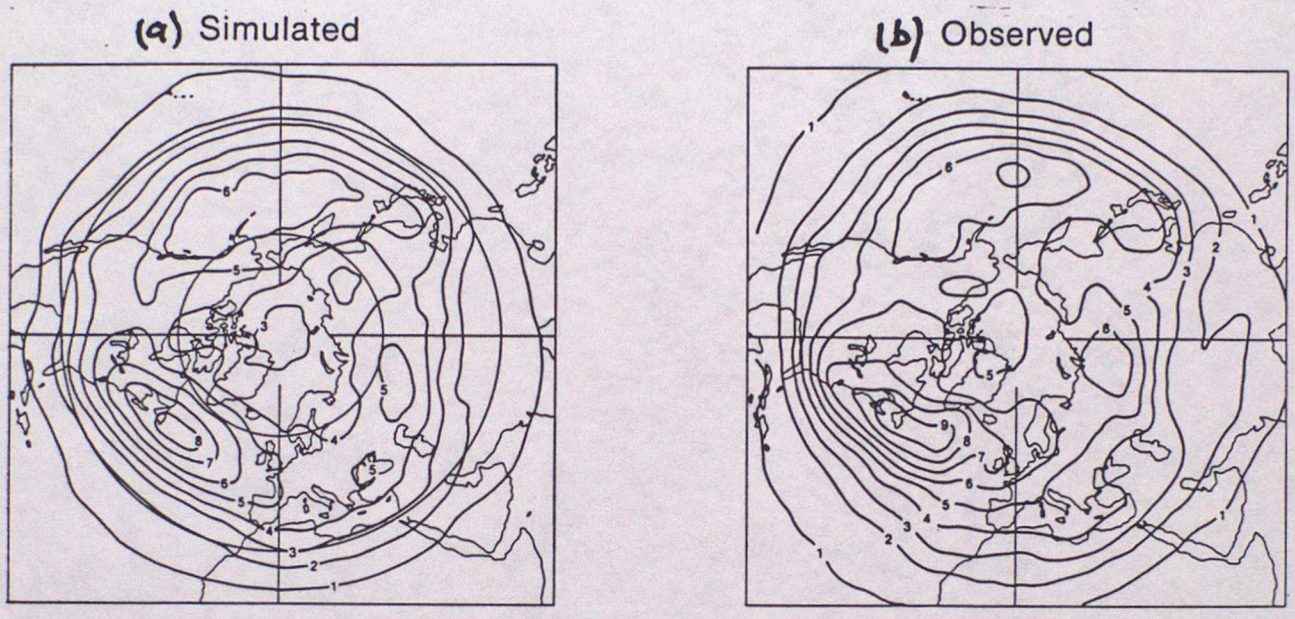

Figure 9.4 High pass filtered variance of 500 mb heights for the northern hemisphere for December to February. Contours every 1 mb.

(a) From a high resolution version of the Met. Office GCM.

(b) Observed, from Met. Office operational analyses, 1983-1986.

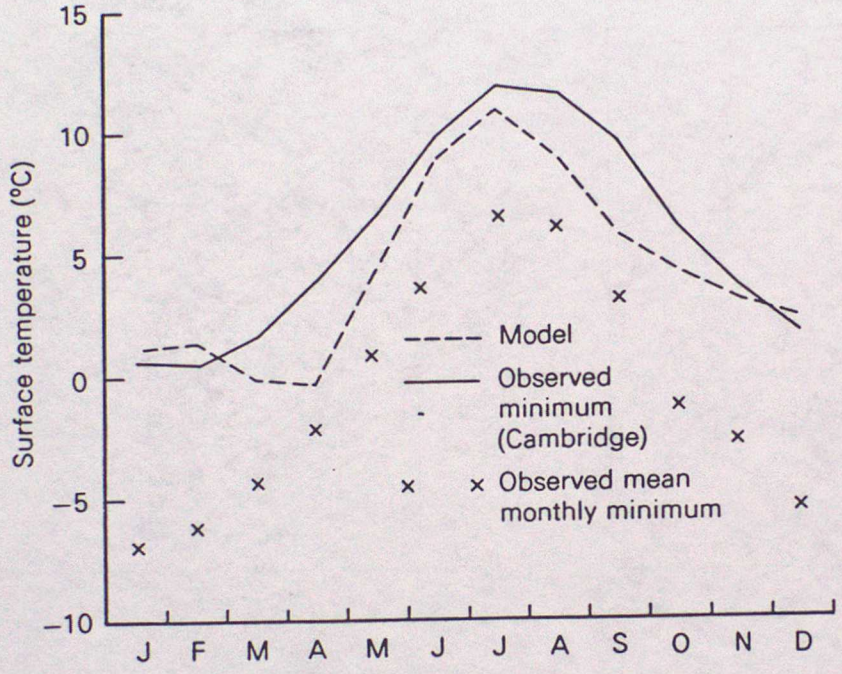

Figure 9.5 Monthly mean surface temperature over Eastern England. Solid line, climatological 2 m screen minimum temperatures at Cambridge; dashed line, simulated ground temperatures 00Z from a 5-layer atmospheric model. (Wilson and Mitchell, 1987b). The crosses are the observed mean monthly minimum.

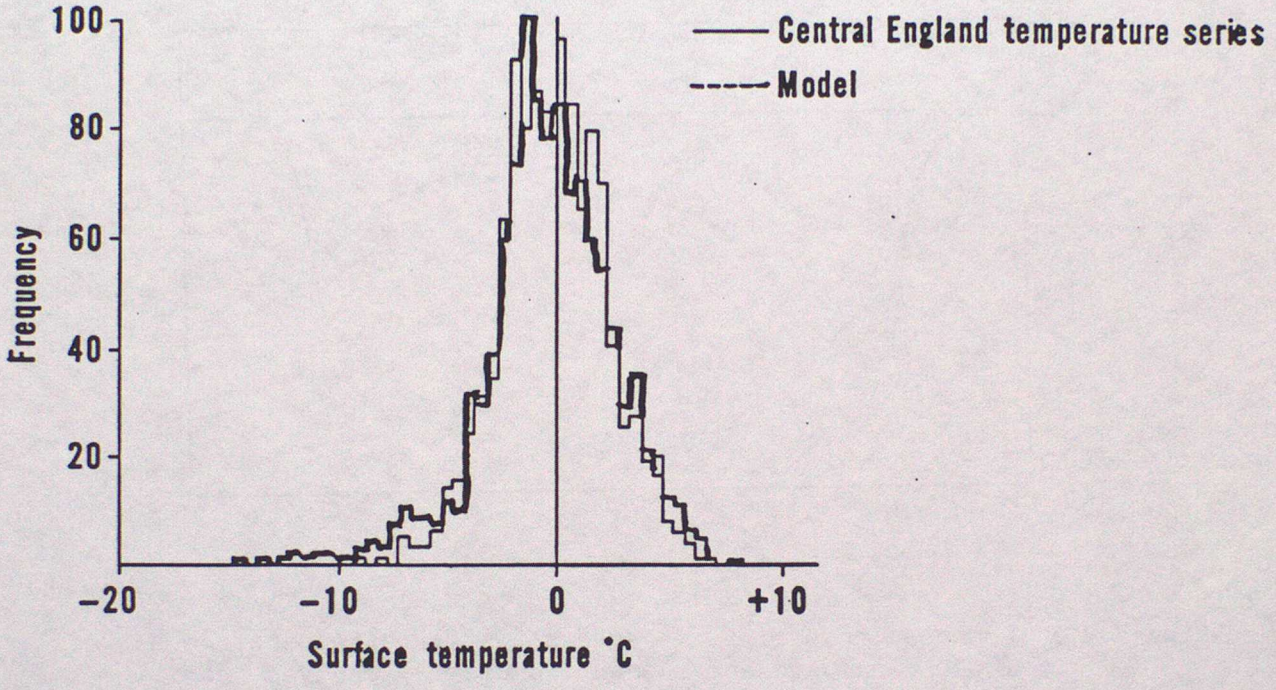

Figure 9.6 Frequency distribution of surface temperature over central/eastern England (mean, annual and semi-annual cycle removed) at 0.5 K intervals.

Light line — From 3 years of Central England Temperature Series

Heavy line — From a 3-year simulation with a 5-layer atmospheric model (Reed, 1986).

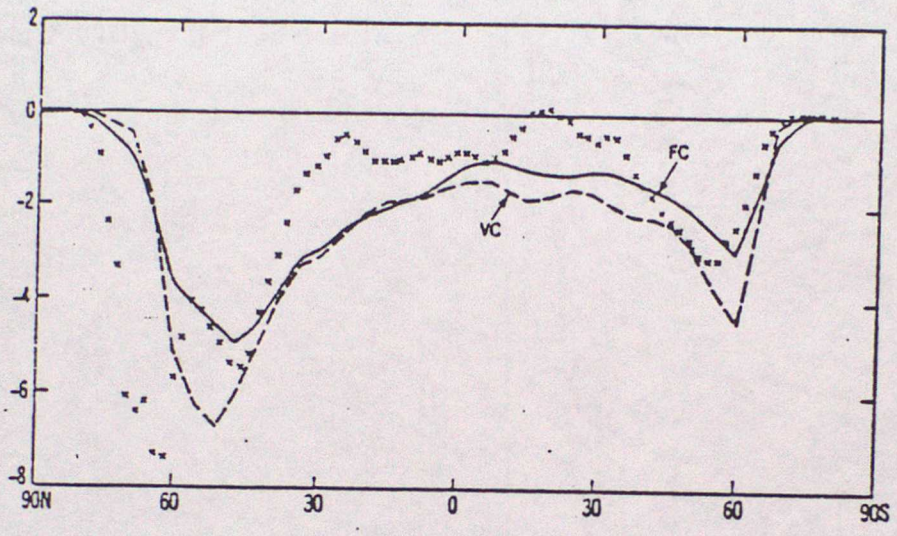

Figure 9.7 Changes in zonally averaged sea surface temperature between 18000 years ago and present. Crosses - derived from palaeological data; Solid line - simulated using prescribed cloud; Dashed line - simulated using model generated cloud. (From Manabe and Broccoli, 1985)

THE PHYSICS AND DYNAMICS OF THE CLIMATE SYSTEM

Simulation of Climate Change

J F B Mitchell

Meteorological Office, Bracknell RG12 2SZ

10.1 INTRODUCTION, WHY MODEL CLIMATE?

The increases in atmospheric "Greenhouse" gases since 1860 have a radiative effect equivalent to a 40% increase in carbon dioxide concentrations, and by the middle of the next century, are expected to be equivalent to a doubling of carbon dioxide concentration. Simulations with detailed climate models indicate that this would produce a warming of 2 to 5 K in global mean surface temperature at equilibrium, with accompanying changes in precipitation, sea level and other parameters. The observed increase of 0.5 K since 1900 is consistent with the lower range of the estimated potential increase, allowing for a possible slowing of the global mean warming due to the ocean's large thermal inertia. Thus, man-made climate change is not just a possibility, it may already be occurring. Consequently, there is an ever pressing need to predict the likely changes in climate due to increases in trace gases in order to guide future energy policies and to minimize the possible climatic impacts. As discussed in Chapter 9, detailed 3-dimensional models of climate are the most promising method of providing the detailed information required for climatic impact assessment.

There is also considerable interest as to why the earth's climate has changed in the past (see Figure 9.1a). Climate models provide a means of testing theories of climate change. Conversely, periods from which reliable and wide-spread palaeoclimatic data are available may be used as a test of the fidelity of climate models, especially if the factors producing the climatic change are well known.

The rest of this paper is arranged as follows:

10.2 The "Greenhouse" effect.

10.3 The principal gases, past, present and future.

10.4 Climate feedbacks in CO_2 experiments.

10.5 Equilibrium climate change due to increased CO_2.

10.6 Modelling the transient response to increases in trace gases.

10.7 Uncertainties in the simulation and detection of the climatic effect of increased trace gases.

10.8 Appeals to the past; simulations for 9000 years before present (9 K bp).

10.9 Concluding remarks.

10.10 Acknowledgements.

10.2 THE "GREENHOUSE" EFFECT

The globally averaged radiative heat balance of the earth-atmosphere system may be approximated by

$$(S_0/4)\ (1-\alpha) = \sigma T_e^4 \qquad (10.1)$$

where S_0 is the solar "constant", α is the fraction of solar radiation reflected by the earth and atmosphere, σ is Stefan's constant and T_e is the mean or effective radiative temperature of the system. T_e is the radiative equilibrium temperature that the earth's surface would reach if the atmosphere was transparent to longwave (thermal or infra-red) radiation. With the current value of α (0.3), T_e = 255 K, some 33 K below the current observed global mean surface temperature.

Now consider a single layer atmosphere, longwave emissivity ε and shortwave albedo α in radiative equilibrium with the surface (Figure 10.1). For convenience, it will be assumed that the atmosphere does not absorb solar radiation. The surface temperature T_* is given by

$$T_*^4 = T_e^4/(1-\varepsilon/2) \qquad (10.2)$$

and the atmospheric temperature T is given by

$$T^4 = \frac{T_*^4}{2} \qquad (10.3)$$

Thus, gases which absorb and emit longwave radiation (greenhouse gases) warm the surface and cool the atmosphere. As an exercise, the reader can show that in a two-level atmosphere in radiative equilibrium, temperature decreases with height.

In practice, the troposphere is not generally in radiative equilibrium, but is heated convectively from the surface. The global mean lapse rate, about 6 K/km, is slightly less than the dry adiabatic lapse rate due to latent heat released in regions of saturated ascent. The radiative equilibrium temperature of 255 K corresponds to a height of 5.5 km (point a on the solid profile in Figure 10.2). An increase in the concentration of greenhouse gases raises the effective emitting level, (point b in Figure 10.2) and reduces the effective emitting temperature T_e and outgoing radiance σT_e^4. The system warms until the temperature at the new emitting level rises to the original value T_e (point c).

The stratosphere will cool if the concentration of greenhouse gases there is increased. The stratosphere is not convectively coupled to the surface but is in radiative equilibrium; an increase in longwave absorbers will produce enhanced emission to space which at equilibrium is compensated by a fall in emitting temperature.

10.3 THE PRINCIPAL ABSORBERS, PAST, PRESENT AND FUTURE

The concentration and radiative characteristics of the climatically most important longwave absorbers in the contemporary atmosphere are listed in Table 10.1, based on Dickinson and Cicerone (1986) and Ramanathan et al (1985). The greenhouse heating is defined as the change in net downward

flux at the tropopause due to the presence of each gas. Since increasing the concentration of greenhouse gases produces a slight increase in the downward flux from the stratosphere, the change in net flux at the tropopause rather than at the top of the atmosphere is considered (Schneider, 1975). Note that the troposphere and surface are strongly coupled and hence can be regarded as a single system. Water vapour is by far the most important "Greenhouse" gas, followed by carbon dioxide. Although the concentrations of chlorofluorocarbons (CFCs) CFC11 and CFC12 are 10^{-6} that of carbon dioxide, their contribution to radiative heating is only a factor 10^{3} less. These gases have absorption bands which are both very strong and lie in the atmospheric "window" from about 833 cm^{-1} to 1250 cm^{-1}, where there is little absorption by other gases.

Estimates of the pre-industrial (1860) concentrations of the main trace gases (other than water vapour) are shown in Table 10.2. The concentrations of carbon dioxide, methane and nitrous oxide are deduced from ice-core sampling. CFCs are produced solely by industrial activity and so their pre-industrial concentration is zero. Gases other than CO_2 produce 30% of the radiative perturbation to date, and the total effect is already equivalent to half that due to doubling carbon dioxide concentrations. There is considerable uncertainty in the estimated concentrations for 2035; the first three gases in Table 10.2 undergo natural cycles which are not completely understood, and for all the gases the industrial contribution is dependent on the world economy and the effectiveness of recent agreements to limit production such as those for carbon dioxide and CFCs. (The assumptions made to derive the concentrations in 2035 are listed in Mitchell (1989) and references therein.) If the estimates in Table 10.2 are not greatly in error, the radiative effect of the increase in all the gases since 1860 will be equivalent to a doubling of CO_2 before 2035, and this would occur even if CFCs do not increase any further.

The effect of alternative scenarios can be estimated from Table 10.2 by noting that the radiative effect of carbon dioxide varies approximately logarithmically with concentration, (Augustsson and Ramanathan, 1977), and that of methane and nitrous oxide as the square root of their

concentration. The effect of CFC11 and CFC12 vary linearly with concentration because of their low concentrations and the fact that they absorb at wavelengths where there is little absorption by other gases.

10.4 CLIMATE FEEDBACKS IN CARBON DIOXIDE EXPERIMENTS

The radiative perturbation due to enhancing trace gases can (in principle) be calculated to any desired accuracy. Doubling carbon dioxide amounts increases the heating of the tropopause and surface by 4 Wm^{-2} (Lal and Ramanathan, 1984), which, assuming the current climate system behaves as a black body at mean temperatures near 255 K, would produce a warming of 1.1 K. However, the atmospheric response to changes in radiative heating is complex involving many processes which are not well understood. These may amplify the perturbation (positive feedbacks) or damp it (negative feedbacks).

Most equilibrium experiments to determine the climatic effects of increases in trace gases have assumed a doubling or quadrupling of carbon dioxide concentrations. The vertical profile of the radiative perturbation due to the other gases in Table 10.2 is qualitatively similar to that due to increasing carbon dioxide, (except near the tropopause where the minor gases produce a slight warming as opposed to a cooling (Ramanathan et al (1985)), so experiments with increased carbon dioxide only are probably adequate to represent the effect of all the gases. Here and in the next section, we will consider the equilibrium response to doubling carbon dioxide concentrations. First, we consider the main climate feedbacks which have been identified in numerical experiments.

A warmer atmosphere will hold more water vapour, and hence enhance the radiative perturbation due to carbon dioxide. Higher temperatures reduce the extent of highly reflective snow and ice, and so increase the absorption of solar radiation. In most simulations with increased carbon dioxide, cloud amount decreases, reducing the amount of insolation reflected back to space, and the mean cloud height increases, further enhancing the "Greenhouse" effect. It is also likely that cloud radiative properties may change. An increase in atmospheric moisture would tend to

increase cloud water content and hence the reflectivity of cloud, producing a negative feedback. Thick clouds behave as black bodies at infra-red wavelengths, but thin high clouds may have an emissivity considerably less than unity. An increase in cloud water would tend to increase the longwave emissivity of high cloud and enhance the "greenhouse" effect, adding a further positive feedback.

The strength of individual feedbacks simulated in GCM experiments has been quantified using a simple zero-dimensional energy balance model

$$C_* \frac{d\Delta T}{dt} + \lambda \Delta T = \Delta Q \qquad (10.4)$$

where ΔQ is the radiative perturbation, ΔT is the change in surface temperature, C_* is the effective heat capacity of the system, and λ is defined as the feedback parameter. At equilibrium, $\Delta T_{eq} = \Delta Q/\lambda$. Thus the smaller λ, the greater ΔT_{eq}, implying a larger positive feedback. Assuming the feedbacks are linear and independent,

$$\lambda = \sum \lambda_i \; ; \; \lambda_i = \Delta Q_i / \Delta T_{eq} \qquad (10.5)$$

where i denotes the individual feedbacks, and ΔQ_i is the radiative perturbation due to the process i alone. For example, if i denotes changes in water vapour, then ΔQ_i is the radiative perturbation due to the increase in water vapour between the perturbed and control simulations, in the absence of changes in other parameters. Typical values for λ_i from GCM experiments are shown in Table 10.3. The water vapour feedback is easily the strongest, and there is good agreement between different models. The ice-snow albedo feedback is small, though it should be noted that the representation of sea-ice in current climate models is simplistic. The strength of the cloud feedback varies from model to model. Estimates of the effect of changes in cloud radiative properties range from a strong negative feedback (Somerville and Remer, 1984) to a weak positive feedback (Roeckner et al, 1987). The representation of clouds and their radiative properties are a source of major uncertainty in climate change experiments.

Other feedbacks have been analysed using one-dimensional radiative-convective models (for example, Schlesinger 1985). However, the reader is warned that the different modelling groups estimate the feedbacks in their experiments in different ways. The main value of feedback analysis is in identifying the processes which most affect climate sensitivity, and in helping to identify the reasons for discrepancies between models.

10.5 SIMULATED EQUILIBRIUM CLIMATE CHANGE DUE TO INCREASED CARBON DIOXIDE

The increases in carbon dioxide and other trace gases have been occurring on timescales of decades to centuries. It is generally assumed that one can ignore changes in the continental ice sheets on this timescale, but not changes in the ocean or sea-ice. Coupled ocean-atmosphere models are at present prohibitively expensive to run to equilibrium, so over the last decade atmospheric models coupled to a simple oceanic mixed layer of prescribed depth have been used to model the effects of increased CO_2. In order to allow for the advection of heat by the oceans, some models have included a prescribed oceanic heat flux C such that the mixed layer temperature T is given by

$$\rho h C_p \frac{dT}{dt} = S + C \qquad (10.6)$$

where ρ, h and C_p are respectively the density, depth and specific heat of the well mixed layer and S is the net downward heat flux from the atmosphere. C may be derived by prescribing the sea (surface) temperature T from climatology in the atmospheric model and integrating through several annual cycles to determine S as a function of time of year and location. Knowing S, h and $^{dT}/_{dt}$, one can derive C as a function of time and space, and prescribe it in equation 10.6 to determine the evolution of T in the coupled atmosphere mixed layer model.

In the remainder of this section, the effect on simulated climate of doubling carbon dioxide will be outlined using examples primarily from Wilson and Mitchell (1987a), henceforth referred to as WM. Schlesinger and

Mitchell (1987) have reviewed three other comparable modelling studies; a fifth study is described by Schlesinger and Zhao (1987). Where appropriate, discrepancies between models are discussed.

Increasing carbon dioxide concentrations leads to a warming of the troposphere and a cooling of the stratosphere (Figure 10.3). In the tropics, the tropospheric warming increases with height, since in low latitudes the lapse rate adjusts towards the moist adiabatic which decreases with increasing temperature. The increase in warming with height is more pronounced in models with penetrative convection schemes as opposed to those with moist convective adjustment. Penetrative schemes are more efficient in transporting moisture upwards, and hence in warming upper levels.

In high latitudes in winter, the low-level inversion confines the warming near the surface. The reduction of snow and sea-ice leads to considerable enhancement of the warming in high latitudes in the winter hemisphere. Note that the removal of sea-ice in summer leads to increased absorption of solar radiation and storage of heat in the mixed layer, delaying the onset of freezing in autumn and early winter (Manabe and Stouffer (1980)). This leads to a pronounced warming, or more precisely, a reduced cooling relative to the control. In contrast, over sea-ice in summer, temperatures generally rise to the melting point of ice and are maintained there in both the control and anomaly simulation. Even where sea-ice is temporally removed in summer, the thermal inertia of the oceanic mixed layer substantially reduces the magnitude of the warming.

The influence of sea-ice is seen more clearly in the geographical distributions of seasonal mean changes in surface temperature (Figure 10.4). During December to February the maximum warming occurs in the Arctic, Hudson Bay and near Kamchatka where sea-ice is thinner or removed altogether in the $2xCO_2$ simulation, and the minimum occurs over Antarctic sea-ice in the Ross and Weddell Seas. In models in which sea-ice extents are excessive in the simulation of present day climate, the high latitude warming is exaggerated and the latitude of the maximum warming may be displaced equatorwards. The warming is generally less over the ocean than over land. Over land,

evaporation may be limited by the dryness of the surface so that a greater proportion of the increase in radiative heating is used to raise surface temperature as opposed to increasing evaporation. In middle latitudes in winter, removal of snow in the $2xCO_2$ simulation also enhances the surface warming.

The warming is a minimum over the tropical oceans. The saturation vapour pressure for water increases exponentially with temperature, so assuming the relative humidity is approximately constant, potential evaporation also increases non-linearly with temperature. As a result more of the increase in radiative heating of the surface is converted to latent heat and less to raising surface temperatures and sensible heat as one goes from cold to warm regions. Increased evaporative cooling at the surface is linked to increased warming due to latent heat aloft, consistent with the reduction in lapse rate in the tropics noted above.

The changes in cloud are qualitatively similar from model to model (Figure 10.5). In general, there is an increase in high cloud and a reduction in upper and middle tropospheric cloud which in some models is most pronounced in the tropics and mid-latitudes. The changes in low cloud vary considerably from model to model, though increases in low cloud are generally restricted to middle and high latitudes. Thus in low latitudes, where insolation is greatest, there is a reduction in planetary albedo (high cloud is generally assigned a low albedo) leading to enhanced absorption of solar radiation, and in the extratropics, there are substantial increases in high cloud tending to reduce longwave cooling to space.

The warming of the atmosphere leads to an increase in specific humidity (41% in WM) and evaporation and precipitation (15% in WM). Precipitation does not increase everywhere, (Figure 10.6) and the spatial scale of the change is smaller than for temperature (compare Figure 10.4). Whereas there is substantial agreement between the temperature changes simulated by different models, there is little agreement between the regional details of the changes in precipitation, especially in the tropics. All models produce increased precipitation in high latitudes, particularly in winter.

The increase in water vapour produces an increase in the transport of moisture into high latitudes, giving enhanced moisture convergence and precipitation. Most models simulate areas of decreased precipitation outside the intertropical convergence zone (ITCZ) and the subtropics, but there is little spatial correlation from model to model. In general, precipitation in the ITCZ is enhanced.

Changes in the variability as well as the mean climate are important in the assessment of the impacts of climatic change. Wilson and Mitchell (1987b) investigated changes in the variability over Western Europe in a $4xCO_2$ sensitivity experiment. They found, for example, statistically significant reductions in the frequency and intensity of summer precipitation over Southern Italy (Figure 10.7).

There is a growing concern that increases in trace gases will lead to drier conditions in the northern and mid-latitude continents in summer. Even if mean summer precipitation increases (Figure 10.5) the soil may still become drier, as found by WM. Three out of five recent studies found a drying in mid-latitudes (Fig 10.8), whereas one model (Washington and Meehl, 1984) produced a wetter land surface on enhancing CO_2.

Mitchell and Warrilow (1987) have investigated the importance of land surface parametrizations on determining the simulated hydrological response to increased CO_2. In the standard formulation, snowmelt is used to augment soil moisture, or is run off if the ground is saturated. In the control simulation, snowmelt saturates the ground in late spring and the surface then dries rapidly through the summer (Figure 10.9a). On enhancing CO_2, precipitation increases in winter, raising soil moisture levels, but snowmelt and the associated summer drying occur earlier but from the same (saturated) level as in the control. The experiment was repeated, changing only the treatment of snowmelt such that all snowmelt is lost as run-off over frozen ground. The loss of snowmelt leads to a much drier control run (Figure 10.9b) and much less pronounced drying during summer. On enhancing CO_2, the enhanced precipitation in winter now enters in the soil, and though the summer drying starts earlier, it starts from a much higher level, and so the soil remains wetter for most of the summer. The model

used by Washington and Meehl (1984) produces an excessively dry surface in the control simulation, apparently as a result of using too low a land surface albedo, and so behaves in a similar manner to the second version of the model described above.

Equilibrium simulations to date using models with a full dynamical representation of the ocean have used idealized geography and annual mean insolation (for example, Spelman and Manabe (1984); Manabe and Bryan (1985)). These studies suggest that the inclusion of the deep ocean does not substantially alter the equilibrium response. A faithful representation of the ocean is however essential if one is to model the time dependent response of climate to increases in greenhouse gases. This is considered in the following section.

10.6 MODELLING THE TRANSIENT RESPONSE TO INCREASES IN TRACE GASES

Although the concentration of "greenhouse" gases has and will continue to increase gradually, the temperature response of the atmosphere is likely to be slowed down by the large thermal inertia of the ocean. If the oceans are assumed to have a constant heat capacity C_* (equation 10.4), then the evolution of the temperature change ΔT due to an instantaneous increase in heating ΔQ at t=0 is given by

$$\Delta T = \frac{\Delta Q}{\lambda} (1 - \exp (- \lambda t/C_*)) \qquad 10.7$$

The time τ taken to reach (1-1/e) of the equilibrium response is C_*/λ. Assuming λ = 1 Wm^{-2} K^{-1} and that the warming is mixed uniformly through the deep ocean, τ is about 500 years. On the other hand, if the warming is confined to the observed seasonal ocean mixed layer which has a depth of order 100 m, then τ is of order 10 years. These two estimates are probably upper and lower limits respectively, and the actual timescale for the oceans depends on the efficiency with which heat is mixed into the deep ocean and so varies between different parts of the ocean.

Rough estimates of the effect of oceanic inertia have been made using one-dimensional diffusive models of the ocean. The evolution of global mean temperatures assuming a doubling of effective carbon dioxide concentrations between 1850 and 2050 and vertical diffusion coefficients of 2.25 m^2 sec^{-1} are shown in Figure 10.10. (See Advanced Lecture 1 (Rowntree)). Two cases are shown corresponding to an equilibrium increase of 4 K and 1.1 K due to doubling CO_2. For each case, the solid curve denotes the equilibrium response, and the dashed curves, the response of the diffusive ocean.

The diffusive model gives a very crude representation of vertical mixing in the ocean, and at equilibrium produces a temperature anomaly which is uniform with depth. Transient experiments have been carried out using coupled ocean atmosphere models in which carbon dioxide concentrations have been instantaneously doubled. The degree to which the warming penetrates the ocean varies with latitude, as can be seen in Figure 10.10 which shows the warming of an annually averaged ocean-atmosphere model with idealized geography 25 years after quadrupling carbon dioxide concentrations. Also shown in Figure 10.10 is the fraction of the equilibrium response achieved after 25 years, and the equilibrium response itself. Estimates of the response time τ derived from simple models at GCMs range from 10 to 100 years (Schlesinger, 1986) and possible reasons for the wide range of estimates have been investigated using simple diffusion models (Wigley and Schlesinger, 1985).

A numerical study carried out by Bryan et al (1988) indicates that the response in high latitudes of the southern hemisphere may be substantially slower than elsewhere because of the larger fractional ocean coverage and the existence of a meridional cell upwelling unmodified water from great depth. Hansen et al (1988) have estimated the time dependent response from 1958 to 2020, using a high, medium and low scenario for future increases in trace gases. In their model, the ocean is represented by a seasonally varying mixed layer. The mixed layer depth and advection of heat are assumed to remain unchanged as the concentration of trace gases is increased, and heat transfer into the deep ocean is represented by simple

diffusion, the coefficient of diffusion being specified geographically on the basis of observations. As a result of their study, Hansen et al (1988) claim that the climatic effects should be clearly discernible in the 1990s. In contrast to Bryan et al (1988), they find that high southern latitudes is one of the regions where the warming should be detected earliest.

10.7 Uncertainties in the simulation and detection of the climatic effect of increases in trace gases.

(a) There are uncertainties in the pre-industrial concentration of carbon dioxide, and hence in the change in radiative forcing since then.

(b) The size of the equilibrium response to a given increase in gases is known only within a factor of 2 or so (Table 10.3), due mainly to uncertainties in the modelling of cloud and cloud radiative properties. These problems are currently an area of intensive research. The nature of the regional response, particularly in the hydrological cycle, varies from model to model. These discrepancies may be reduced by using higher horizontal resolution and improved physical paramatrizations.

(c) There is much to learn concerning the vertical mixing of heat in the oceans and its representation in numerical models. It is not known whether or not one has to resolve oceanic eddies in order to produce a reliable simulation of the changes in oceanic heat transport. Current global ocean GCMs have a horizontal resolution of 300-500 km. These require large horizontal diffusion coefficients which maintain numerical stability but also smooth out the more intense ocean currents.

(d) The climatic effects of enhanced trace gas concentrations have to be detected against the background of the natural variability of the atmosphere and ocean. The instrumental temperature record (Figure 9.1) exhibits variability on timescales up to several decades. Some indication of the inherent variability of climate on the decadal timescales may be obtained from long (of order 100 years) simulations

of coupled ocean atmosphere models (see also Lecture 9 on Climate of the World) . Hence there remains some uncertainty in the observed warming.

(e) There remains the possibility that other factors are masking (or enhancing) the effects of increases in "greenhouse" gases. There has been much speculation concerning the possibility of changes in the solar "constant". Accurate measurements of the solar constant have only been available for the last decade or so, and these indicate a decrease of 0.1% between 1980 and 1985 (Willson et al, 1986). (The climatic effect of a 2% increase in solar constant is thought to be approximately equivalent to that due to a doubling of carbon dioxide concentrations, Wetherald and Manabe, 1975.) Variations in the concentration and composition of stratospheric aerosol resulting from volcanic eruptions have also been cited as a cause of climatic change, but the indices used to categorize volcanic dust do not allow a quantitative estimate of the associated radiative effects.

10.8 APPEALS TO THE PAST; A SIMULATION FOR 9000 BEFORE PRESENT (9 Kbp)

In order to try and limit some of the uncertainties discussed in the previous section, attempts have been made to model past climates and compare the simulated changes with the changes from the present deduced from palaeoclimatic data. Models have also been used to help understand past climates (for example Kutzbach and Guetter, 1986). The two periods chosen most frequently are the last glacial maximum (18 Kbp) and part of the Holocene around 9 Kbp. During the latter period, perihelion almost coincided with the summer as opposed to the winter solstice, enhancing insolation during the northern summer, especially in high northern latitudes. Here, a brief summary of some recent simulations for 9 Kbp (Mitchell et al, 1988) will be given. This period is of interest because

(a) The changes in boundary conditions are simple; the changes in orbital parameters are well known, CO_2 concentrations are believed to have been similar to present, and the ice sheet over North America was relatively small in extent.

(b) There is a large amount of palaeoclimatic data available from that period.

In the initial experiment, only the orbital parameters were altered. The enhanced insolation during the boreal summer produces an increase in surface temperature over the northern mid-latitude continents (Figure 10.12a). This enhances the land-sea contrast, lowering surface pressures over the continents (Figure 10.12b) and enhancing the monsoon precipitation over Venezuela, East Africa and Southern Asia (Figure 10.12c). The land surface becomes drier in mid-latitudes (Figure 10.13a) and wetter over most of the tropics. This is consistent with estimates of lake levels for the period (Figure 10.13b) which are lower than average in mid-latitudes and above average in the tropics. Although the broad pattern of simulated changes is in agreement with palaeoclimatic data, there are discrepancies, as over West Africa, where the model produces a drier surface at 9 Kbp, whereas the lake level data suggest that it was wetter then. This shortcoming has been the subject of further investigation.

10.9 CONCLUDING REMARKS

General circulation models have been used to investigate the climatic effects of a wide variety of other phenomena including sea surface temperature and sea-ice anomalies, changes in land surface characteristics due to desertification or deforestation, "nuclear winter" and waste heat from energy parks. Experiments have also been carried out to determine the influence of topography, land-sea contrasts and so forth on the general circulation of the atmosphere.

Although the use of climate models has become more frequent, each experiment should still be analysed carefully before one attempts to interpret the results. In doing so, one must bear in mind the limitations of the model and how such limitations will distort the simulated response. One can attempt to do this by isolating the mechanisms producing the changes in climate in the model, and assessing the physical realism of each step. Where there is some uncertainty concerning a parametrization on which the model's response is dependent, the experiment can be repeated

using alternative forms of that parametrization to determine whether or not the uncertainties affect the results. One also has to consider whether or not all the physical processes relevant to the experiment have been included in the model. In short, one should always treat results from numerical models with a certain amount of cynicism until they are supported by a critical assessment of the model used and the simulated response.

10.10 ACKNOWLEDGEMENTS

The development, running and assessment of climate models is not a task that can be carried out by an individual. I am indebted to members of the Dynamical Climatology Branch of the Meteorological Office over the last 10 years for their help and support. I am also grateful to colleagues at other modelling centres who have provided additional information on their experiments. Peter Rowntree and Alayne Street-Perrott kindly provided Figures 10.10 and 10.13(b) respectively.

10.11 REFERENCES

Augustsson, T. and Ramanathan, V. 1977 A radiative — convective model study of the CO_2 climate problem. J. Atmos. Sci., 34, 448-51.

Bryan, K., Manabe, S. and Spelman, M.J. 1988 Interhemispheric Asymmetry in the transient response of a coupled ocean-atmosphere model to a CO_2 forcing. J. Phys. Oceanogr. 18, 851-867.

Dickinson, R.E. and Cicerone, R.J. 1986 Future global warming from atmospheric trace gases. Nature, 319, 109-115.

Hansen, J., Fung, I., Lacis, A., Rind, D., Lebedeff, S., Reudy, R. and Russell, G. 1988 Global climatic changes as forecast by Goddard Institute for Space Studies Three Dimensional Model. J. Geophys Res. (To appear).

Hansen, J. Lacis, A., Rind, D., Russell, L, Stone, P., Fung, I., Ruedy, R. and Lerner, J. 1984 Climate Sensitivity, Analysis of Feedback Mechanisms. In Climate Processes and Climate Sensitivity (ed J. Hansen and T Takahashi) Geophysical Monograph 29, 130-163. American Geophysical Union, Washington DC.

Kutzbach, J. E. and Guetter, P. J. 1986 The influence of changing orbital parameters and surface boundary conditions on climate simulations for the past 18,000 years. J. Atmos Sci. 43, 1726-1759.

Lal, M. and Ramanathan, V. 1984 The effects of moist convection and water vapour radiative processes on climate sensitivity. J. Atmos. Sci. 41, 2238-2249.

Manabe, S. and Bryan, K.Jnr. 1985 CO_2-Induced Change in a Coupled Ocean-Atmosphere Model and the Paleoclimatic Implications. J. Geophys. Res. 90, C11, 11,689-11,707.

Manabe, S. and Stouffer, R.J. 1980 Sensitivity of a global climate model to an increase in the CO_2 concentration in the atmosphere. J. Geophys. Res. 85, 5529-5554.

Mitchell, J.F.B. and Warrilow, D.A. 1987 Summer dryness in northern mid-latitudes due to increased CO_2. Nature 330, 238-240.

Mitchell, J.F.B., Grahame, N.S. and Needham, K.J. 1988 Climate simulations for 9000 years before present: Seasonal variations and the effect of the Laurentide ice sheet. J. Geophys Res. 93, 8283-8303.

Mitchell, J.F.B. 1989 The "greenhouse" effect and climate change. Submitted to Revs. of Geophysics.

Ramanathan, V., Cicerone, R.J., Singh, H.B. and Kiehl, J.T. 1985 Trace Gas and Trends and their potential role in climate change. J. Geophys. Res. 90, 5547-5566. J. Geophys. Res.

Roeckner, E., Schleses, U., Biercamp. J. and Loewe, P. 1987 Cloud optical depth feedbacks and climate modelling. Nature, 329, 138-139.

Schlesinger, M.E. 1985 Feedback analysis of results from energy balance and radiative-convective models. In "Projecting the climatic effects of increasing atmospheric carbon dioxide", edited by M.C. MacCracken and F.M. Luther, pp 280-319, US Department of Energy, Washington DC, 1985. (Available as NTIS, DOE (ER-2037 from Natl. Tech Inf.Serv., Springfield Va.)

Schlesinger, M.E. 1986 Equilibrium and transient climatic warming induced by increased atmospheric CO_2. Climate Dynamics 1, 35-51.

Schlesinger, M.E. and Mitchell, J.F.B. 1987 Climate model simulations of the equilibrium climatic response to increased carbon dioxide. Reviews of Geophysics 25, 760-798.

Schlesinger, M.E. and Zhao, Z. 1987 Seasonal climate changes induced by doubled CO_2 as simulated by the OSU atmospheric GCM/mixed layer model. Oregon State University Climatic Institute Report 70, 73pp.

Schneider, S.H. 1975 On the Carbon Dioxide Climate Confusion. J.Atmos.Sci. 32, 2060-2066.

Somerville, R.C.J. and Remer, L.A. 1984 Cloud Optical Thickness Feedbacks in the CO_2 Climate problem. J. Geophys. Res. 89, 9668-9672.

Spelman, M.J. and Manabe, S. 1984 Influence of Oceanic Heat Transport upon the sensitivity of a model climate. J. Geophys. Res. 89, 571-586.

Washington, W.M. and Meehl, G.A. 1984 Seasonal Cycle Experiment on the Climate Sensitivity Due to a Doubling of CO_2 with an Atmospheric General Circulation Model Coupled to a Simple Mixed Layer Ocean Model. J. Geophys. Res. 89, 9475-9503.

Wetherald, R.T. and Manabe, S. 1975 The effects of changing of the solar constant on the climate of a general circulation model. J. Atmos. Sci. 32, 2044-2059.

Wetherald, R.T. and Manabe, S. 1986 An investigation of cloud cover change in response to thermal forcing" Climate Change. 8, 5-24.

Wigley, T.M.L. and Schlesinger, M.E. 1985 Analytical solution for the effect of increasing CO_2 on global mean temperature. Nature 315, 649-652.

Willson, R.L., Hudson, H.S., Frohlich, C. and Brusa, R.W. 1986 Long term downward trend in solar radiance. Science, 234, 1114-1117.

Wilson, C.A. and Mitchell, J.F.B. 1987a A Doubled CO_2 Climate Sensitivity experiment with a GCM including a simple ocean. J. Geophys. Res, 92, 13315-13343.

Wilson, C.A. and Mitchell, J.F.B. 1987b Simulated climate and CO_2 induced climate change over Western Europe. Climatic Change, 10, 11-42.

10.12 BIBLIOGRAPHY

Physically-based modelling and simulation of climate and climate change

Vol 2 (1988) Schlesinger, M.E. (Ed) NATO Advanced Study Institute Series (Reidel, in Press). This volume covers applications of climate models as opposed to their development.

The "Greenhouse" Effect, Climatic Change and Ecosystems: 1987

Bolin, B., Doos, B.R., Jager, J. and Warrick, R.A. (Eds). SCOPE 29, Wiley, New York. Probably the best book to date covering the "greenhouse" effect and related topics.

Climate Model Simulations of the Equilibrium Response to Increased Carbon Dioxide: 1987

Schlesinger, M.E. and Mitchell, J.F.B., Rev. of Geophysics, 25, 760-798. A detailed review of CO_2 simulations up to 1986.

Issues in Atmospheric and Oceanic Modelling, Part A. Climate Dynamics: 1985

Manabe, S. (Ed). Advances in Geophysics Vol. 28, Academic Press (London). Chapters by Dickinson on Climatic sensitivity, Manabe and Wetherald on CO_2 and hydrology and Kutzbach on modeling of palaeoclimatics are of particular interest.

Palaeoclimatic Analysis and Modeling: 1985 Hecht, A.D. (Ed) John Wiley and Sons (New York). An excellent book describing both methods on analysis of palaeoclimatic data and some numerical experiments.

Table 10.1 Current concentrations and "greenhouse heating" due to trace gases. The main absorption bands and band strengths (a measure of the probability of a molecule absorbing a photon at the band wavelength) are shown for the less abundant gases.

Gas	Concentration (ppm)	Principal absorption bands Position (cm^{-1})	Strength $cm^{-1}(atm\ cm)^{-1}STP$	Greenhouse heating Wm^{-2}
Water Vapour	~3000			~100
Carbon Dioxide	345	667	(many bands)	~50
Methane	1.7	1306	185	1.7
Nitrous Oxide	0.30	1285	235	1.3
Ozone	$10-100\times10^{-3}$	1041	376	1.3
CFC11	0.22×10^{-3}	846	1965	0.06
		1085	736	
CFC12	0.38×10^{-3}	915	1568	0.12
		1095	1239	
		1152	836	

Table 10.2. Past and projected greenhouse gas concentrations and associated changes in "greenhouse" heating ΔQ

Gas	Assumed 1860 Concentration	ΔQ 1860 to 1985	Estimated 2035 Concentration (ppm)	Estimated ΔQ 1985 to 2035 (Wm^{-2}) Range
Carbon Dioxide	275.	1.3	475	1.8
Methane	1.1	0.4	2.8	0.5
Nitrous Oxide	0.28	0.05	0.38	0.15
CFC11	0	0.06	1.6×10^{-3}	0.35
CFC12	0	0.12	2.8×10^{-3}	0.69
TOTAL		1.9		3.5

Table 10.3 ANALYSIS OF FEEDBACKS AND TEMPERATURE CHANGES DUE TO DOUBLING CO_2, BASED ON TYPICAL VALUES FROM GCM EXPERIMENTS

FEEDBACK	STRENGTH ($WM^{-2}\ K^{-1}$)	TEMP. CHANGE (Cumulative)
NONE	+3.7	1.1
WATER VAPOUR	-1.4	1.7
ICE/SNOW	-0.3	2.1
CLOUD AMOUNT	-0.9	4.0
CLOUD RADIATIVE PROPERTIES	-0.1 to 0.5	2.7 - 4.5

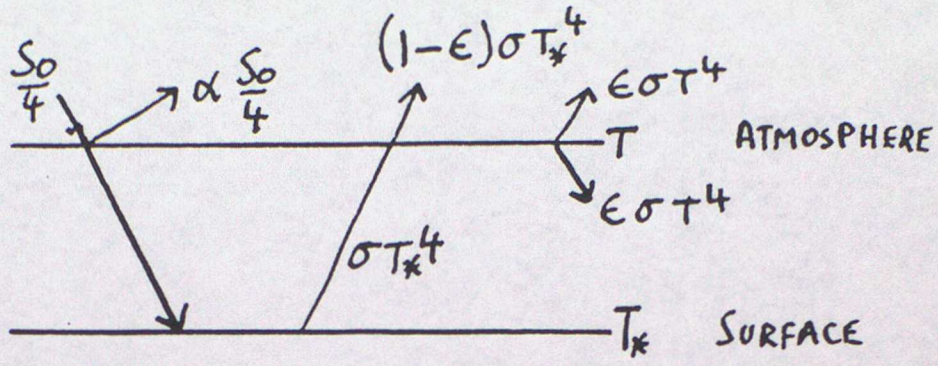

Figure 10.1 In idealized single layer atmosphere, reflectivity α, longwave emissivity ε and temperature T in radiative equilibrium with the surface at temperature T_*.

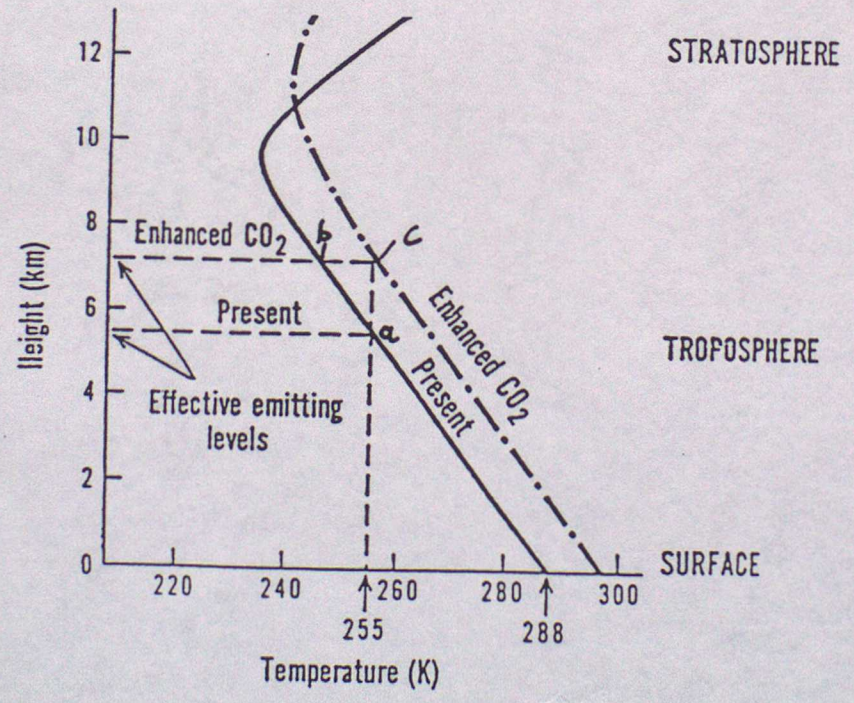

Figure 10.2 The effect on vertical temperature profile of increasing atmospheric CO_2 concentrations (schematic). Increasing CO_2 raises the emitting level from a to b, and the profile then warms from b to c to restore the effective emitting temperature to its original value.

(a)

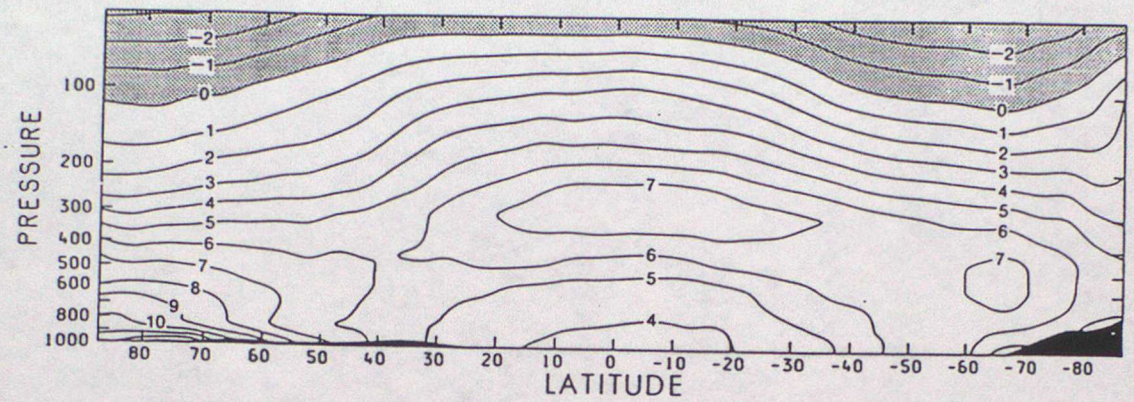

(b)

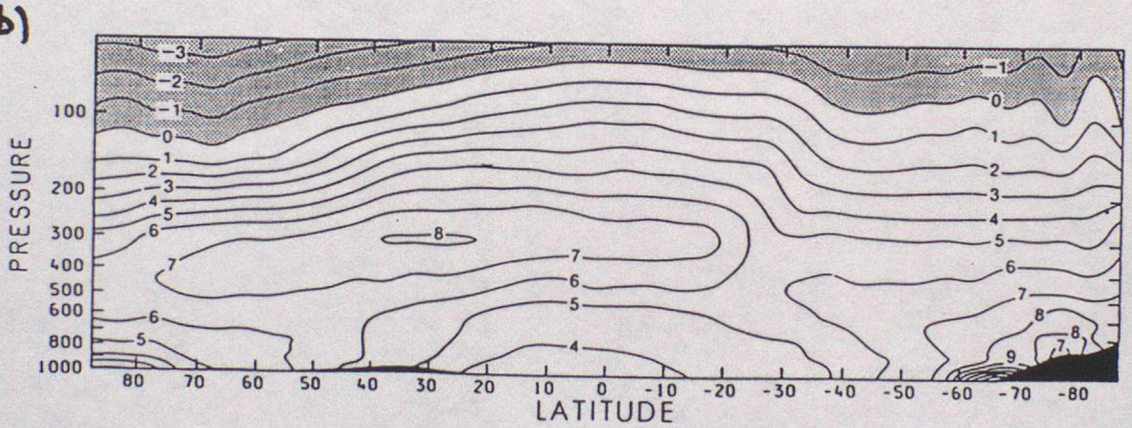

Figure 10.3 The height/latitude distribution of simulated temperature changes due to doubling CO_2 concentrations. Areas of decrease are stippled (a) Northern winter (December to February) (b) Northern Summer (June to August). From Wilson and Mitchell (1987a).

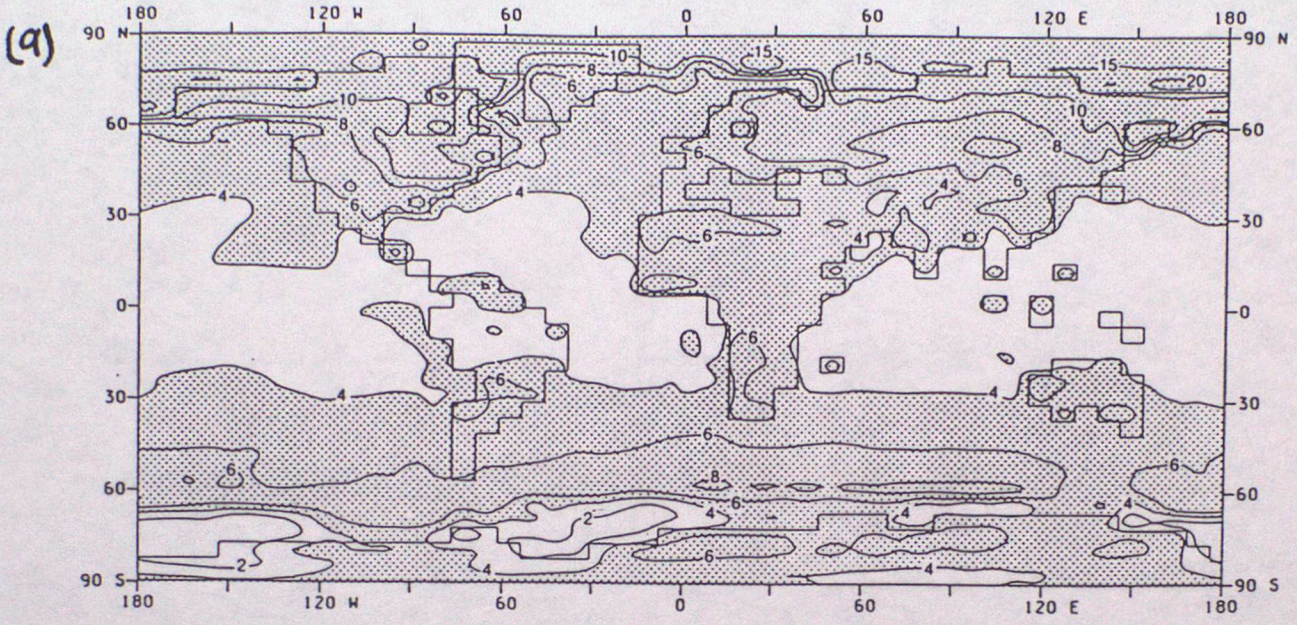

Fig. *ia*

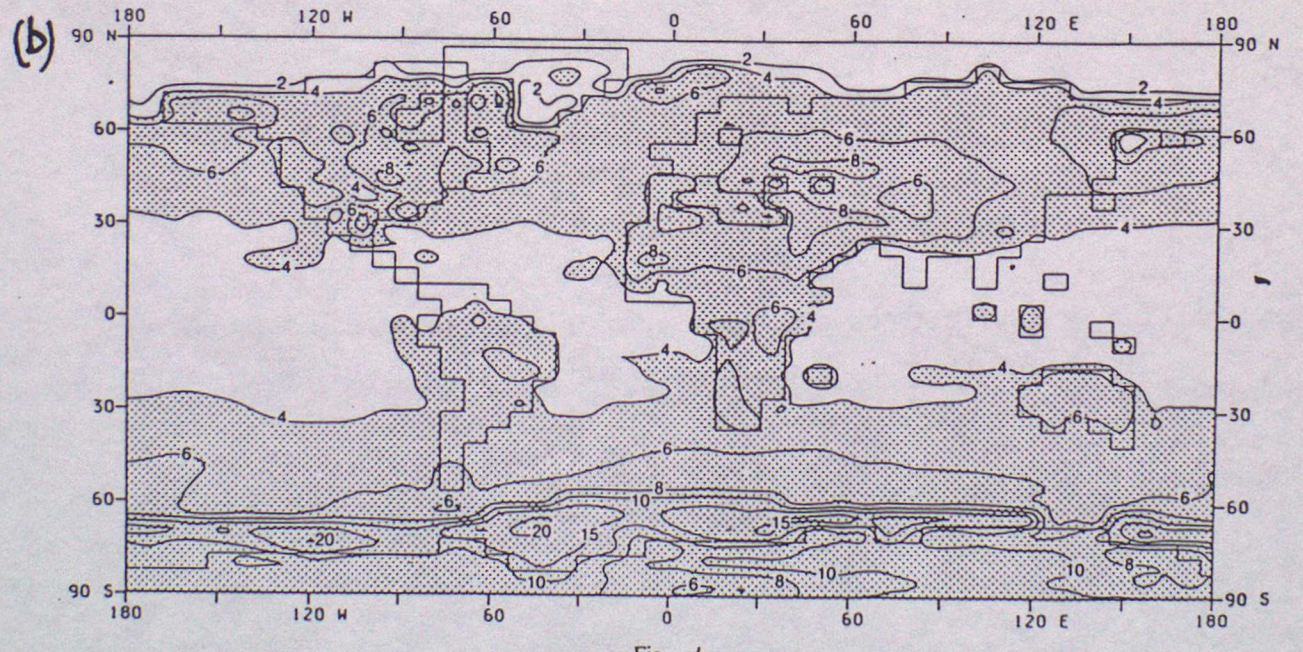

Fig. *b*

Figure 10.4 Simulated changes in surface temperature due to doubling CO_2 concentrations. (a) Northern winter (b) Northern Summer.

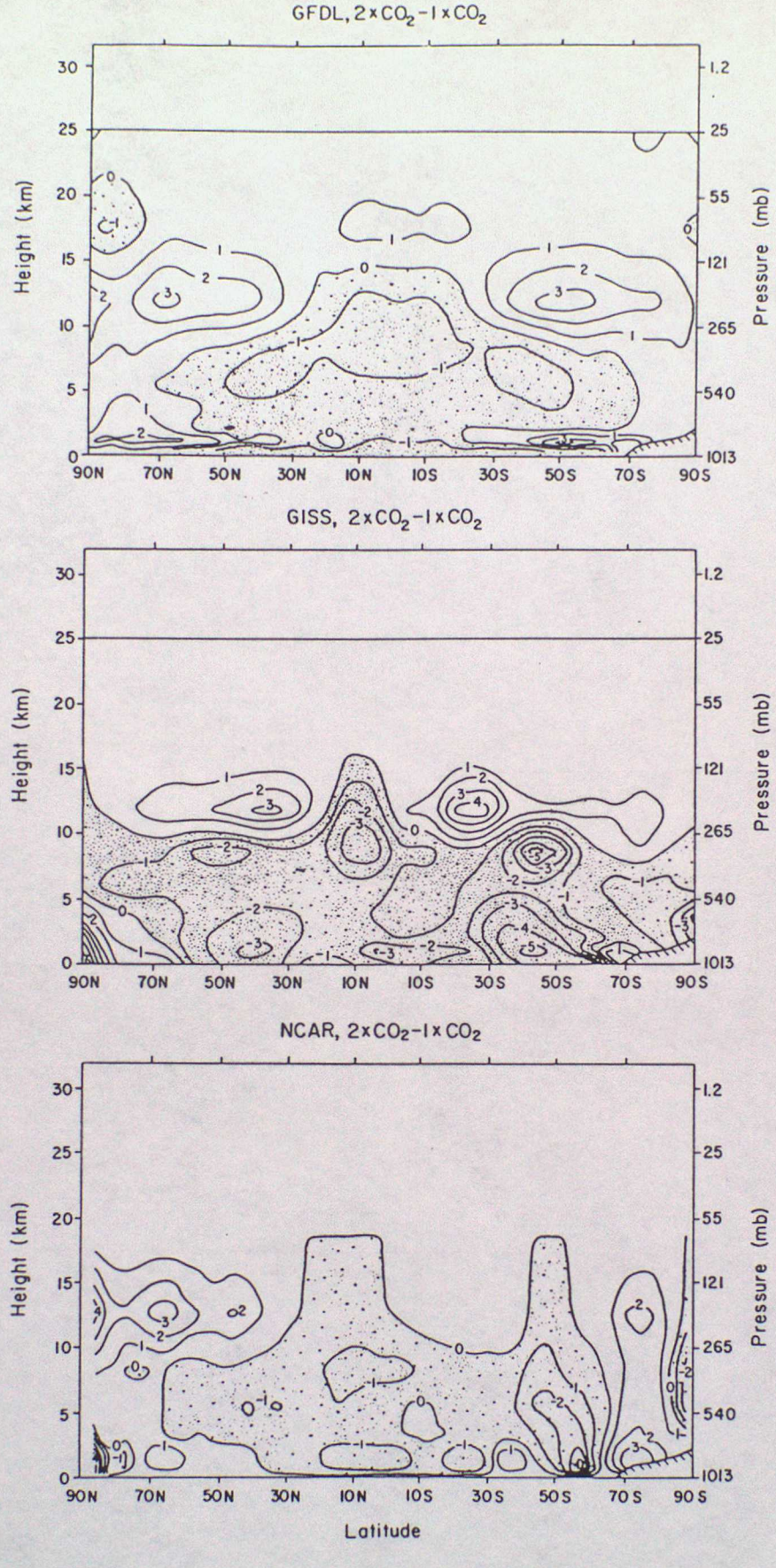

Figure 10.5 The height/latitude distribution of simulated annual mean changes in cloud from three different models. Areas of decrease are stippled, and the units are percent of total cover. Top, from Wetherald and Manabe (1986); Centre, from Hansen et al (1984); bottom, from Washington and Meehl (1984).

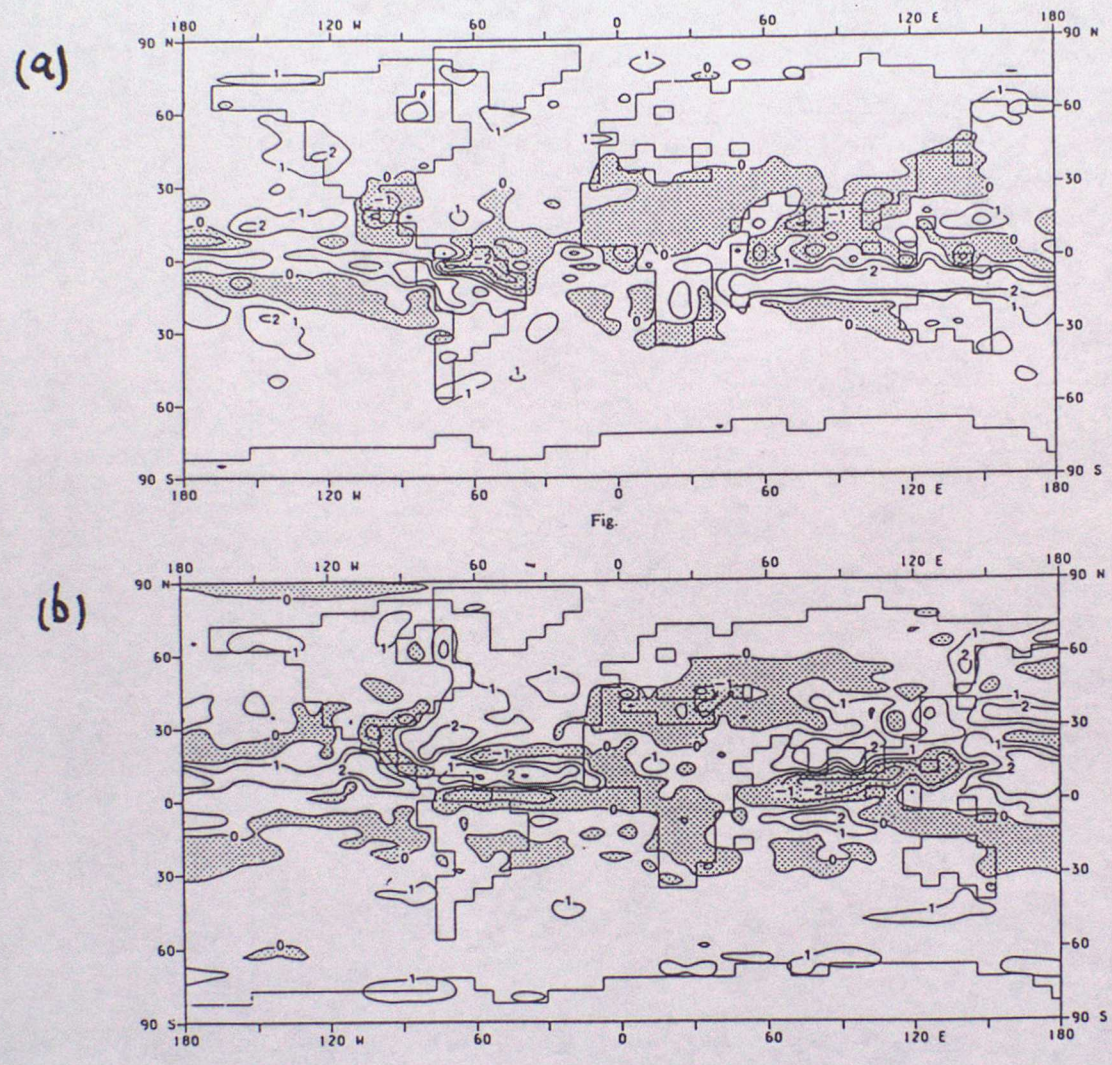

Fig.

Figure 10.6 Simulated changes in precipitation rate (mm/day) due to doubling CO_2 concentrations. Areas of decrease are stippled (a) Northern winter (b) Northern Summer. From Wilson and Mitchell (1987a).

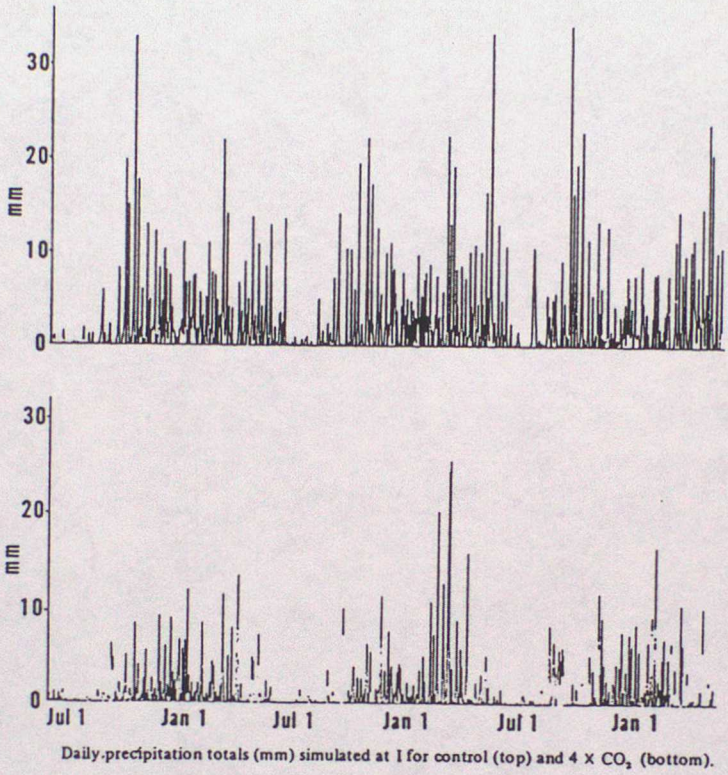

Daily precipitation totals (mm) simulated at I for control (top) and 4 × CO_2 (bottom).

Figure 10.7 Simulated daily precipitation totals (mm) at a grid point over Southern Italy. Top panel, with quadripled CO_2 amounts and enhanced sea surface temperatures: bottom panel, with present CO_2 amounts and sea surface temperatures. From Wilson and Mitchell (1987b).

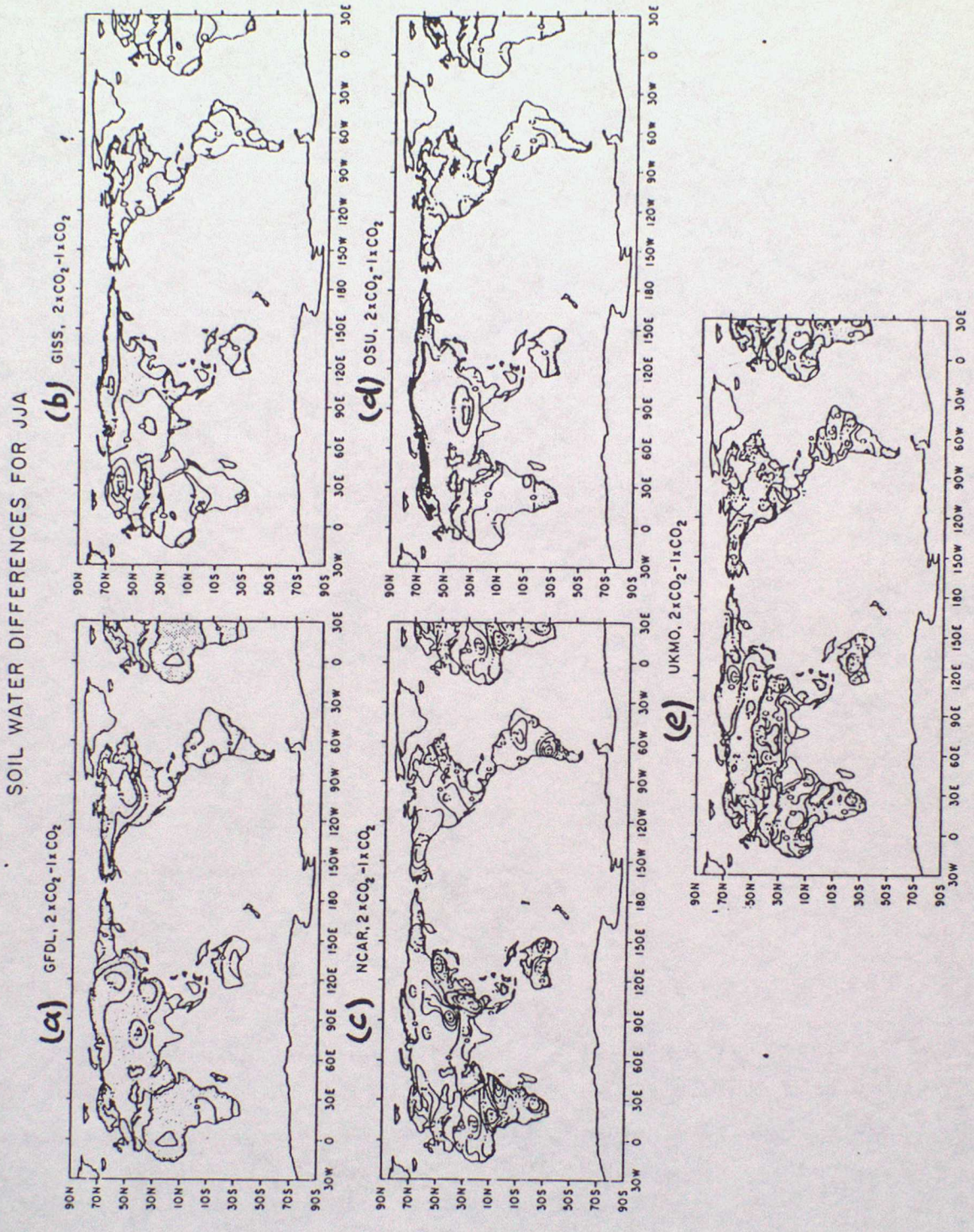

Figure 10.8 Simulated changes in soil moisture (cm) due to doubling CO_2 amounts. (a) From Manabe and Wetherald (1987) (b) Hansen et al (1984) (c) Washington and Meehl (1984) (d) Schlesinger and Zhao (1987) (e) Wilson and Mitchell (1987a).

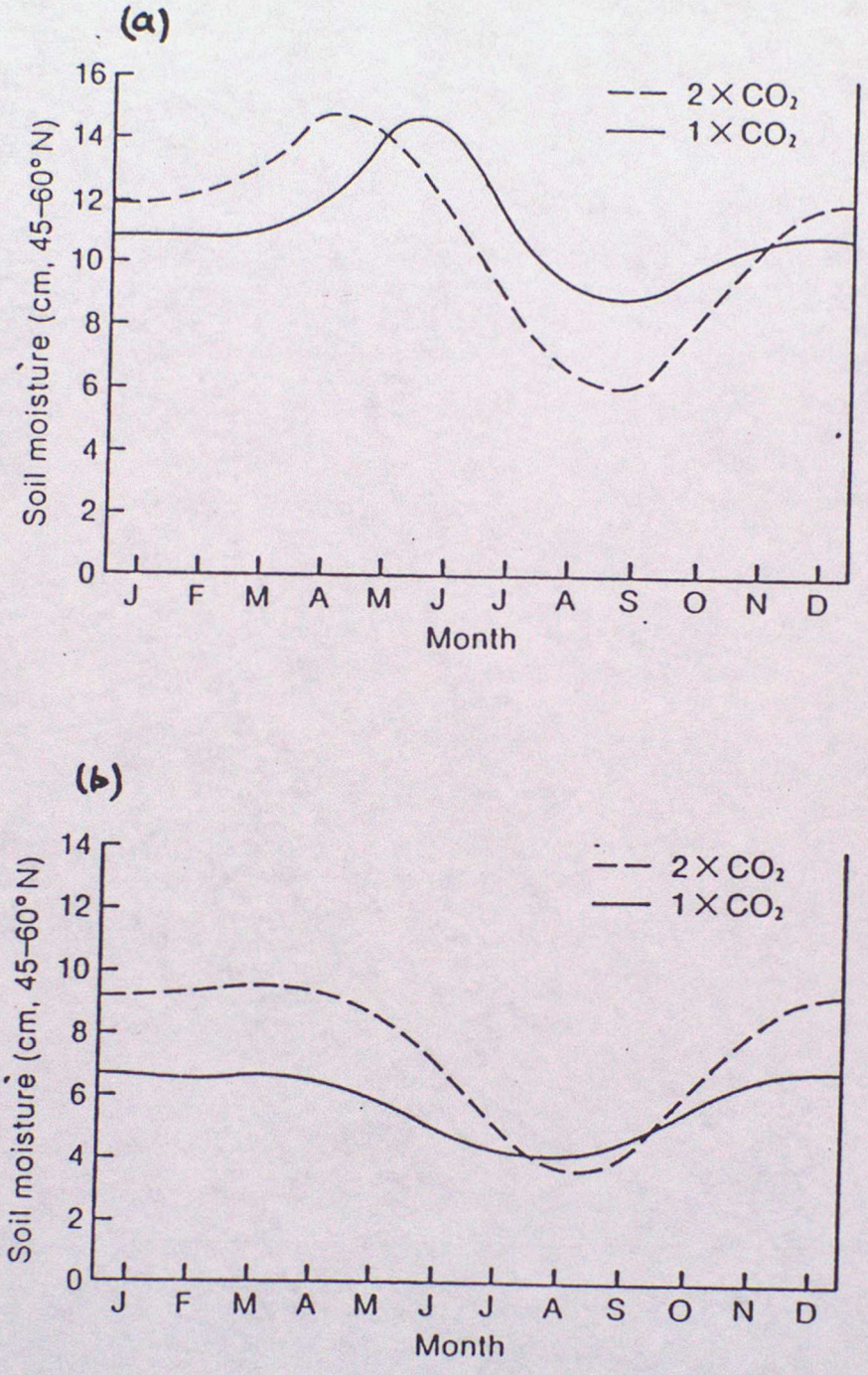

Figure 10.9 Simulated monthly mean soil moisture averaged over land between 45° and 60°N for $1xCO_2$ (solid line) and $2xCO_2$ (dashed) line. (a) Allowing snowmelt to augment soil moisture (b) Running off snowmelt if the ground is frozen. From Mitchell and Warrilow (1987).

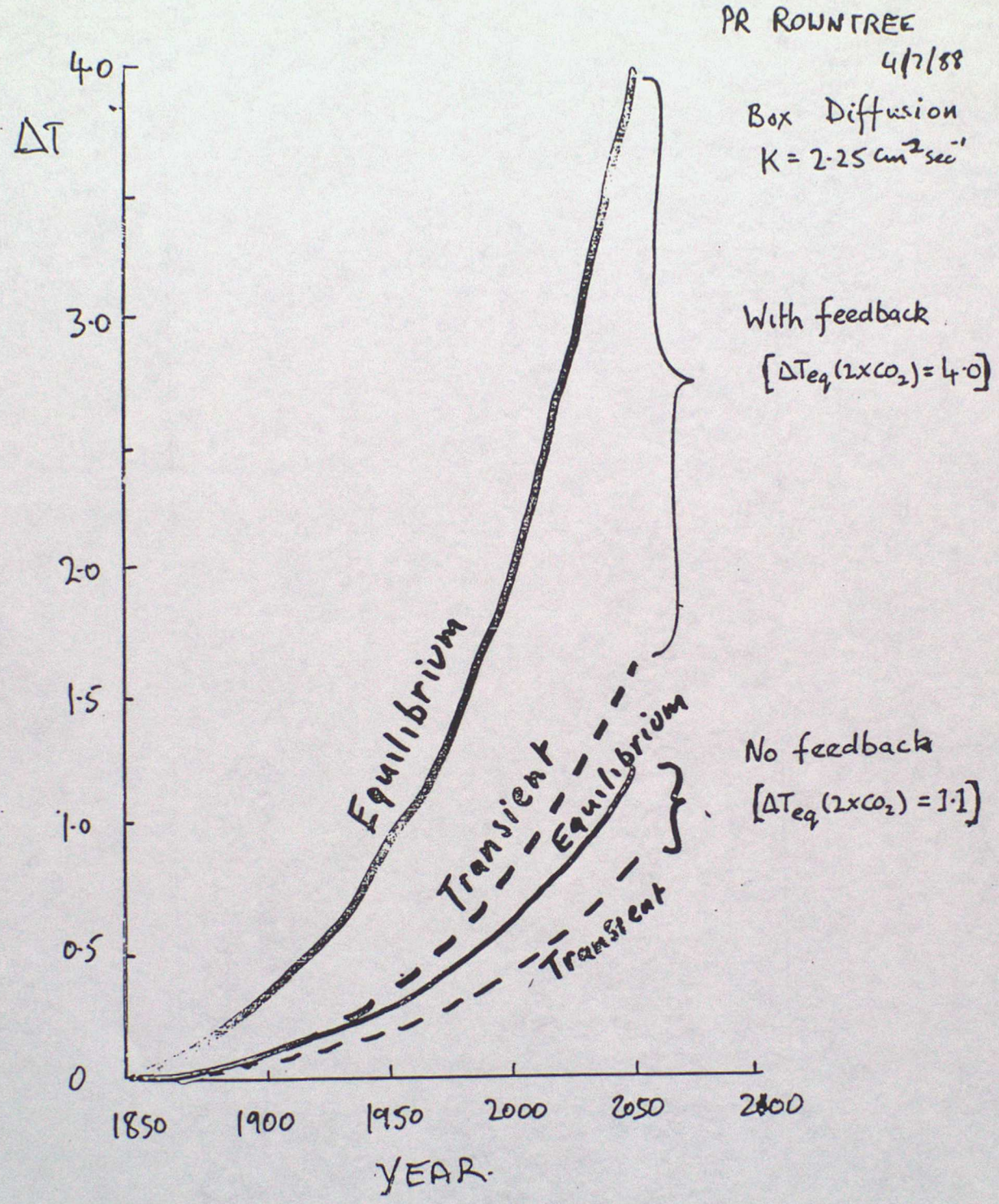

Figure 10.10 Estimates of the time dependent response to doubling effective CO_2 concentrations between 1850 and 2050, made using a one-dimensional diffusive ocean model with a vertical diffusion of 2.25 cm^2 sec^{-1}. The solid curves represent the instantaneous equilibrium values, the dashed curves the actual response allowing for oceanic thermal inertia. The upper curves allow for climate feedbacks, the lower curve neglect feedbacks. (Rowntree 1988, personal communication).

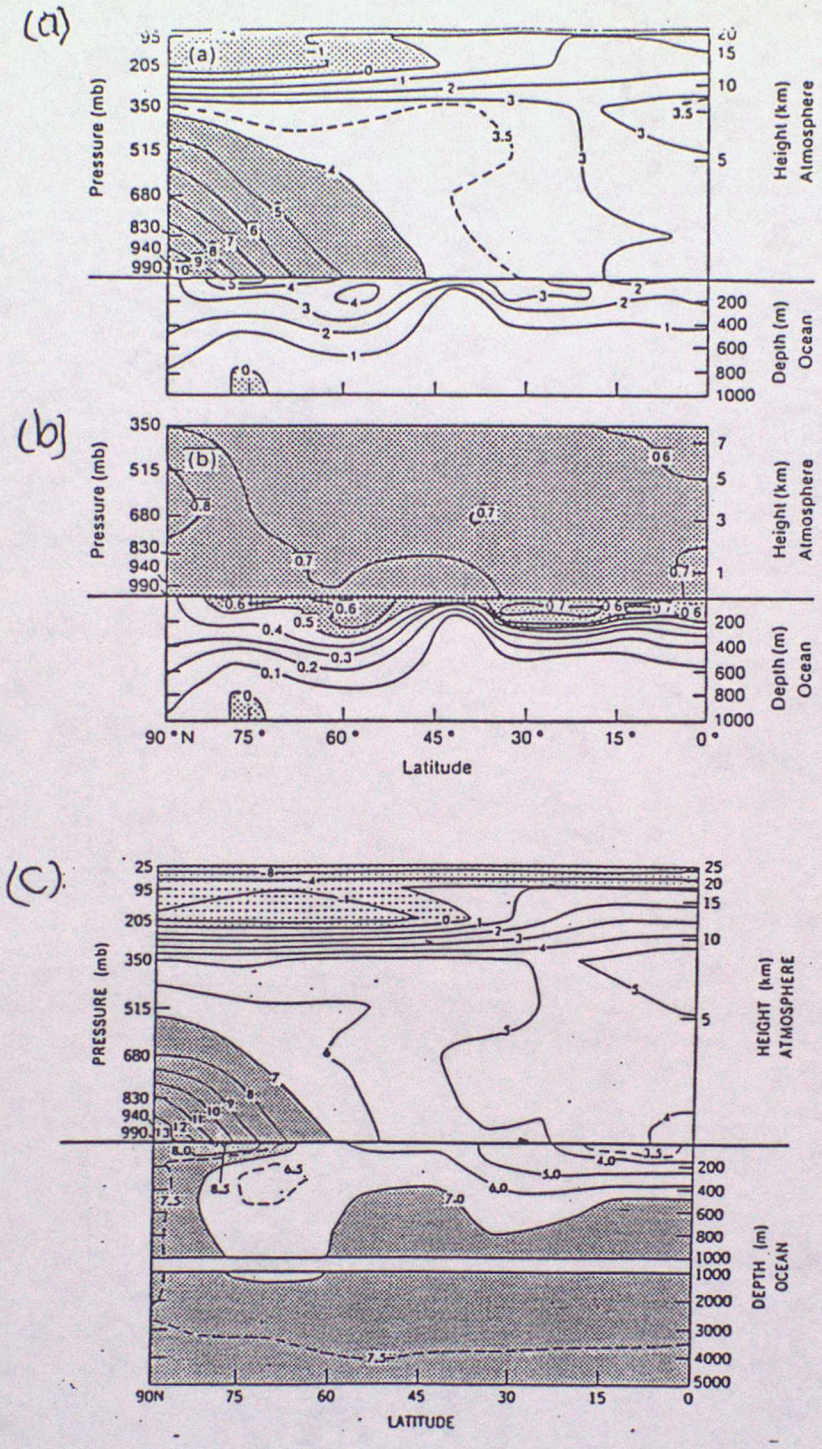

Figure 10.11 Height (depth)/latitude diagrams of the simulated changes in atmospheric (oceanic) temperatures due to quadrupling CO_2 amounts in an annually averaged coupled ocean-atmosphere model using idealized topography. Upper panel, the changes 25 years after instantaneously quadrupling CO_2 amounts. Middle panel, the percentage of the equilibrium response achieved after 25 years. Lower panel, the equilibrium response. From Spelman and Manabe (1984).

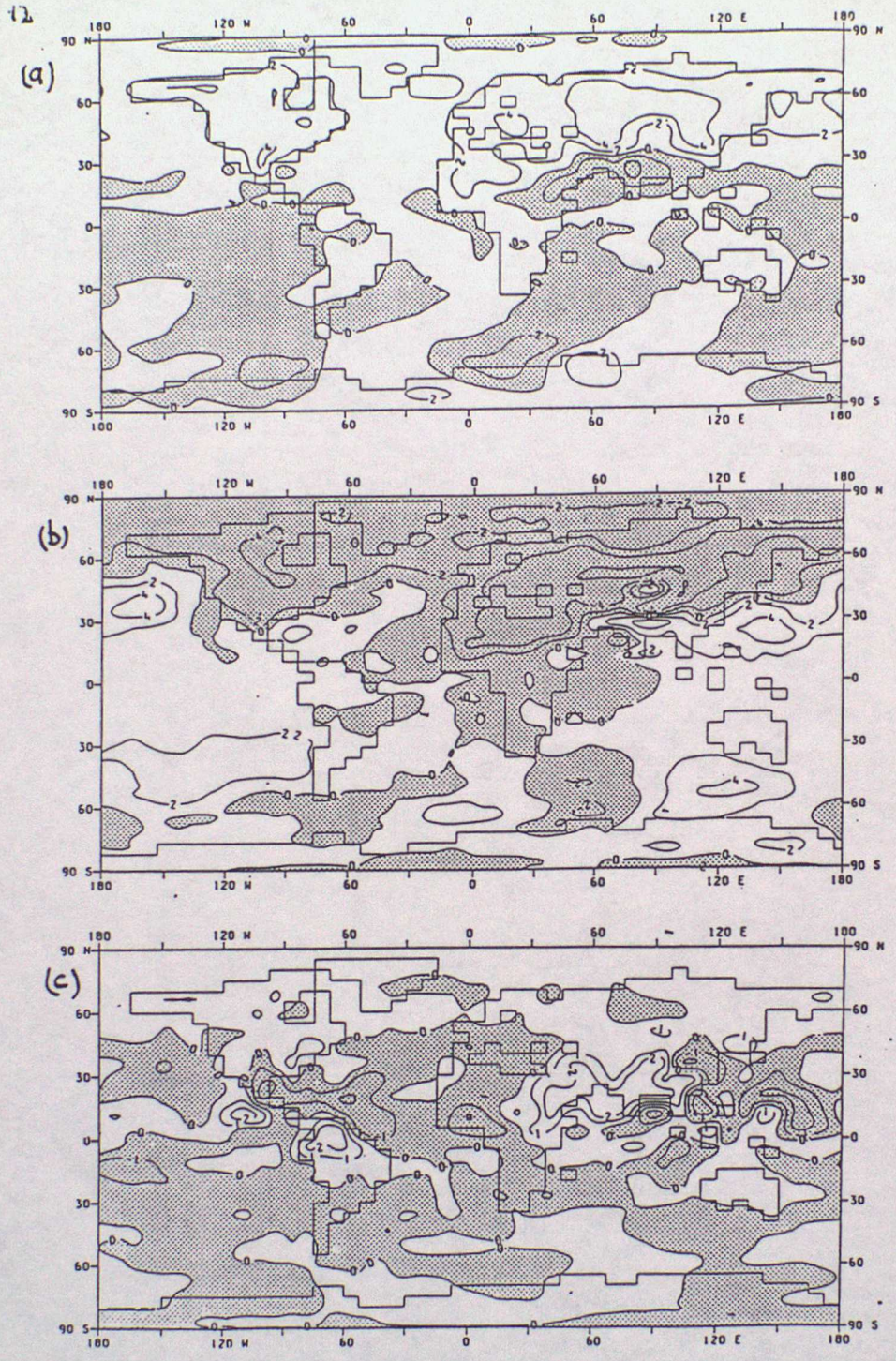

Figure 10.12 Simulated changes during northern summer due to change in the earth's orbital parameters to those appropriate to 9 Kbp. (a) Surface temperature (K), (b) Sea-level pressure (mb), (c) Precipitation rate (mm/day). Areas of decrease are stippled. From Mitchell et al (1988).

(a)

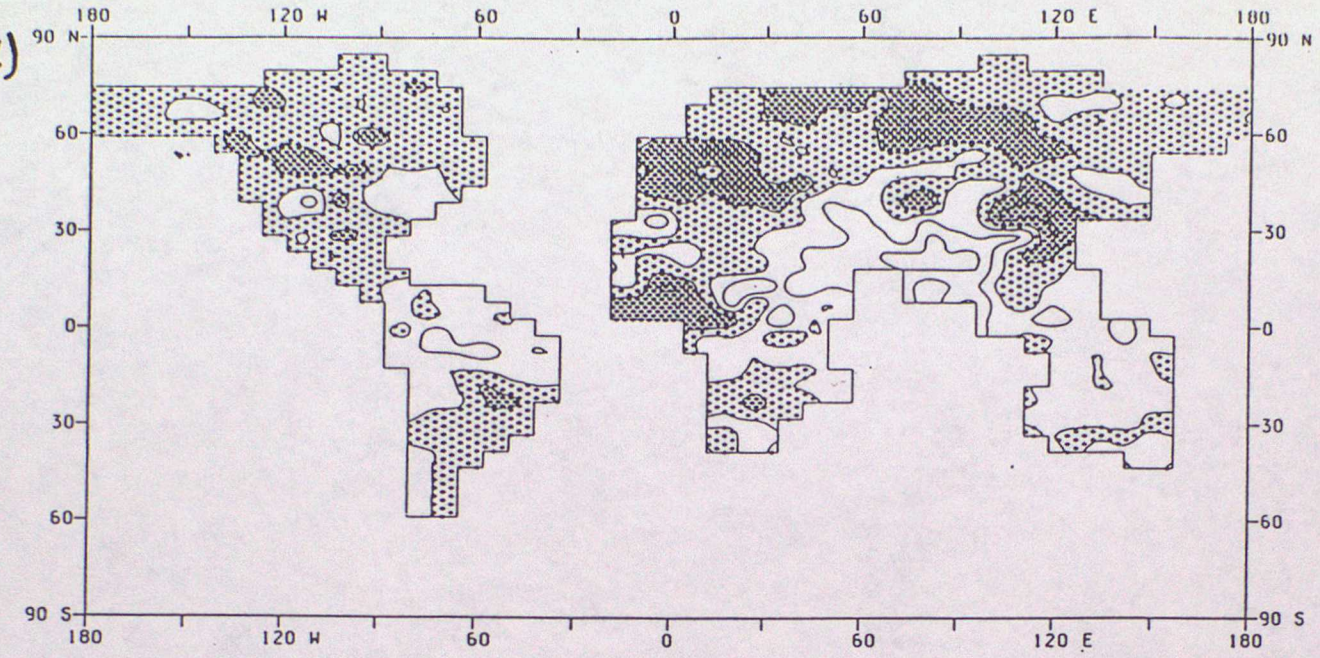

(b)

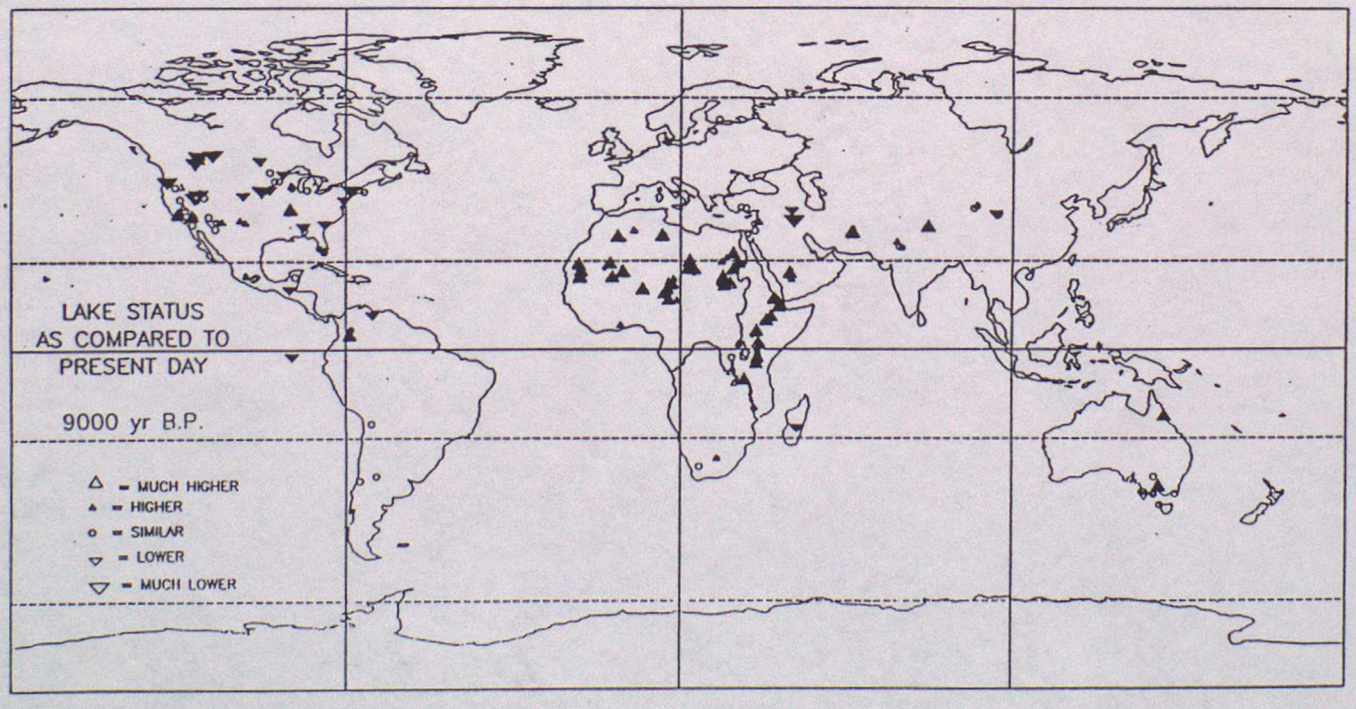

Figure 10.13 (a) Simulated changes in soil moisture (9 Kbp-present). Contours at 0, ±2, ±5 cm. Areas of decrease are stippled, and reductions greater than 2 cm are stippled heavily. From Mitchell et al (1988). (b) Changes in lake level status between 9 Kbp and present. (Street-Perrott, 1988, personal communication.)